IMPERIAL COLLEGE LONDON

MODELLING OF ELECTROMAGNETIC ACOUSTIC TRANSDUCERS

by

Remo Ribichini

A thesis submitted to Imperial College London for the degree of

Doctor of Philosophy

Department of Mechanical Engineering

Imperial College London

London SW7 2AZ

February 2011

Ai Miei Genitori

Declaration of originality

The material presented in the thesis "Modelling of Electromagnetic Acoustic Transducers" is entirely the result of my own independent research under the supervision of Professor Peter Cawley. All published or unpublished material used in this thesis has been given full acknowledgement.

Name: Remo Ribichini 03/03/2011

Signed:

"È bellissimo."

Manuela Arcuri commenting on the "sms-epistolary novel"
"Il labirinto femminile" by Alfonso Luigi Marra.

Abstract

At present, the dominant technology for transducers in the field of Ultrasonic Non-Destructive Testing is piezoelectric. However, some industrially important applications, like the inspection of components operating at high temperature or while in motion, are difficult tasks for standard piezoelectric probes since mechanical contact is required. In these cases, contactless NDT techniques can be an attractive alternative. Among the available options, Electromagnetic Acoustic Transducers (EMATs) can generate and detect ultrasonic waves without the need for a physical contact between the probe and the test object, as their operation relies on electromagnetic, rather than mechanical coupling. Since EMATs do not require any coupling liquid, the experimental procedures for inspection set-up are simplified and a source of uncertainty is eliminated, yielding highly reproducible tests that make EMATs suitable to be used as calibration probes for other ultrasonic tests. A further advantage of EMATs is the possibility of exciting several wave-modes by appropriate design of the transducer. Unfortunately, EMATs are also characterized by a relatively low signal-to-noise ratio and by a complex operation relying on different transduction mechanisms that make their performance dependent on the material properties of the testpiece.

The present work aims to develop a numerical model including the main transduction mechanisms, the Lorentz force and magnetostriction, that can be employed as a prediction tool to improve the understanding of EMAT operation. Following an overview on the historical development of EMATs and their models, the theory describing EMAT operation is presented. The governing equations are implemented into a commercial Finite Element package. The multi physics model includes the simulation of the static and dynamic magnetic fields coupled to the elastic field through custom constitutive equations to include magnetostriction effects. The model is used to quantitatively predict the performance of a magnetostrictive EMAT configuration for guided waves without employing arbitrary parameters. The results are compared to experimental data providing a validation of the model and insight

on the transduction process. The validated model, together with experimental tests, is exploited to investigate the performance of different EMAT designs for Shear Horizontal waves in plates. The sensitivities of each configuration are compared and the effect of key design parameters is analyzed. Finally, the model is used in the evaluation of the performance of bulk wave EMATs on a wide range of steel grades. Experimental data interpreted via numerical simulations are employed to investigate the relative weight of the transduction mechanisms, with implications on the applicability of EMATs on the range of steels usually encountered in inspections.

Acknowledgements

I would like to express my deepest gratitude to Prof. Peter Cawley for his impeccable supervision and constant support. His scientific rigour and devotion to research are invaluable teachings that I will carry throughout my future professional and personal life. I am grateful to Dr Fredric Cegla for his valuable advice that was so needed to get started with my research. Credit goes to them and Prof. Mike Lowe and Dr Francesco Simonetti for creating a stimulating and fruitful research environment in the Non-Destructive Testing Group.

I am extremely grateful to Prof. Peter B. Nagy of University of Cincinnati for his essential help in the experimental part of this work and for easing my ignorance in the field of electromagnetism. Not only have our discussions been enlightening for me, but also very enjoyable.

I also would like to thank all the members of the NDT group in general for their help and cooperation. I must mention in particular Marco for (rightly) convincing me that joining this group was a great idea, Giuseppe for his patience and help, Prabhu, Ken, Jake and Tom for their encouragement and support that meant so much to me, especially during the early stages of my Ph.D.

All my gratitude goes to those who made this beautiful scientific experience also a wonderful time with their friendship: Tino "il boss" for the time at our mansion in Ingelow road, Rosalba for the countless "short coffee breaks", Bieppe for making me explore London culinary, Michela for teaching me not only English, but also Italian, Sara for managing all the events with a rock mood, Andrea for introducing me to the proper English traditions, Tim for letting me know about his "awesome" ideas.

Nothing of this would have ever happened without the support and love of my family: a huge thank you to Mamma, Neno, Piggi, Teta e Nonna.

Finally, my heartily *grazie* to Elvira, whose enthusiasm and smile fill my life with joy.

Contents

List of Figures

List of Tables

Chapter 1

Introduction

1.1 Motivation

Ultrasonic Non-Destructive Testing and Evaluation (NDT&E) is a widespread practice in modern engineering and industry. The need for early detection of flaws and defects in critical components employed in oil and gas, power generation and aerospace industries is paramount. It is easy to understand that a failure in one of them not only causes severe economic damage but can also provoke fatal harm to human beings. The ability to detect, locate and size a flaw in components guarantees their safety and allows the estimation of the remanent life, reducing the maintenance cost and unnecessary replacement of safe parts.

NDT&E is a wide subject, involving several fundamental branches ranging from the processing and interpretation of signals to the assessment of the probability of the detection of a given kind of defect. The very source of information, however, comes form the transducers employed in the tests; the understanding of the operation of the sensors is thus fundamental, in order to exploit their features as much as possible and optimize their design. The dominant technology in ultrasonic sensors is piezoelectric. These devices offer a series of positive characteristics: high signal to noise ratio, linear behaviour, simplicity of hardware, ease of use and relatively low cost [1–3]. However, piezoelectric transducers suffer from a major drawback,

that is, physical contact is required between the sensor and the test object, often by means of a coupling fluid. This implies that piezoelectric transducers can be difficult to apply in a number of situations: e.g. measurements at high temperature or on moving samples [2–4]. Moreover, the coupling fluid represents a source of errors and uncertainty even in conventional applications and can make the experimental procedure more complex. In this niche of applications, contact-less NDT methods can be more attractive. The main non-contact NDT ultrasonic methods exploit laser-based technologies or Electromagnetic Acoustic Transducers (EMATs) [1,5–7]; the latter will be the subject of the present study. Even if a considerable amount of research has already been done in the study of EMATs, a better understanding of the transduction process is desiderable, not only for the sake of pure scientific knowledge, but also to choose the best configuration of this kind of sensor in practical applications.

The main novelty of this work is the inclusion of magnetostriction in a Finite Element code. This transduction mechanism, occurs when EMATs are employed on ferromagnetic media. Previous research had laid the theoretical basis of this phenomenon and numerical models had been presented, however, an experimentally validated model was still lacking. The model presented in this thesis allows the operation of EMATs to be simulated quantitatively even on ferromagnetic materials when the physical properties and geometry of the system are given. Once the accuracy of the numerical model is assessed via experimental validation, the model can be employed to compare the performance of different EMAT configurations and to investigate the experimental behaviour of EMATs on different kinds of steel materials. The analysis of EMAT performance on steel materials with the aid of the numerical model gives an estimate of the relative importance of different transduction mechanisms so shedding new light on an existent inconsistency in the literature.

1.2 Thesis outline

This thesis follows the structure outlined below. The first three chapters summarize previous research and serve as an introduction to the new contributions of this thesis, which are presented in Chapters 4 to 8.

Chapter 2 gives a general overview on Electromagnetic Acoustic Transducers. A basic physical explanation of how EMATs can excite and detect ultrasonic waves is given; then the major advantages and drawbacks of EMATs are highlighted. A classification of the most common and important EMAT configurations follows. Finally, a literature review is presented, giving an overview on the historical development of EMATs and the models describing their performance.

In Chapter 3 the physics underlying EMAT operation is described. The equations governing both the generation and the reception mechanisms are presented. Each transduction phenomenon involved in EMAT operation is covered, though special emphasis is given to magnetostriction, being intrinsically the more complex, and, at the same time, the less understood phenomenon. A new analysis of magnetostriction, in terms of static and dynamic components of the relevant fields is presented.

The numerical implementation of the governing equations into a commercial Finite Element software is the subject of Chapter 4. A full 3D model, including the main transduction mechanisms is presented. The full model is compared to simplified models exploiting analytical expressions available for special cases. A description of the absorbing regions, symmetries and meshes used in the simulations is given.

The presented model is validated in Chapter 5. At first the main elements of the model, i.e. electrodynamic, magnetostatic and elastic models are benchmarked against analytical solutions for simple configurations. Then a full EMAT model, including the coupled electromagnetic and mechanical modules is validated against experimental results. Following the description of the experimental set-up used, qualitative and quantitative validations of the model are presented. The material of this Chapter, and parts of the previous Chapters, are the basis of an article pub-

lished in IEEE Transactions on Ultrasonics, Ferroelectrics and Frequency Control ([P2] in the List of Publications).

In Chapter 6 the performance of different EMAT configurations used in the inspection of plates with Shear Horizontal waves is investigated. Simulations supported by experimental evidence allow a comparison of the different designs available in terms of signal amplitude achievable, also taking into account practical issues, such as the ease of use and robustness of each configuration. This Chapter is the basis of an article submitted to IEEE Transactions of Ultrasonics, Ferroelectrics and Frequency Control [P5].

The performance of bulk shear wave EMATs when used on a wide range of steel grades is the subject of Chapter 7. The dependence of EMAT performance on a typical range of physical properties encountered in practice is assessed by means of experiments, interpreted with the help of the numerical model. Conclusions on the relative importance of the transduction mechanisms involved are drawn, leading to useful design suggestions. The results give indications on an existent inconsistency in the literature and are supported by the possible identification of a flaw in published work, presented in Appendix A. The findings described in this Chapter have been submitted to the journal NDT&E International [P4].

Finally, the main results of this work are summarized in Chapter 8 and suggestions for future work are given.

Chapter 2

EMAT background and literature review

2.1 Introduction

This chapter introduces the basic principles of operation of Electromagnetic Acoustic Transducers, highlighting the main advantages and limitations of EMATs. The principal features and applications of the most popular and important EMAT configurations are discussed. Finally, a literature review on the historical development of EMATs and their modelling is given.

2.2 Basic EMAT operation

EMATs are essentially made of a coil fed by a large dynamic current (a pulse or a toneburst are commonly used) and a magnet or electromagnet providing a static magnetic field. When the sensor is close to a metallic sample, an eddy current density $\mathbf{J}_e$ is induced in it; the interaction of this current density with the bias magnetic flux density $\mathbf{B}$ results in a net body force on the sample (Figure 2.1 (a)),

according to the Lorentz equation:

$$\mathbf{f} = \mathbf{J}_e \times \mathbf{B}. \tag{2.1}$$

This force causes the generation of ultrasonic waves in the solid, that can be exploited for NDT purposes [5, 8–10]. From a microscopic point of view, the electric field $\mathbf{E}$ induced by the driving current exerts a Coulomb force $-e\mathbf{E}$ on the electrons of the sample and accelerates them to mean velocity $-eE\tau/m$; when a bias magnetic flux density $\mathbf{B}$ is present, the electrons are also subject to the Lorentz force $e\mathbf{v_e} \times \mathbf{B}$. Here e indicates the charge of the electron and $\mathbf{v_e}$ its mean velocity [7]. For harmonic oscillations much slower than the mean frequency of electron-ion collision $1/\tau$, the inertial forces of the electrons can be neglected and the equation of motion reduces to:

$$n_e(m\mathbf{v_e})/\tau = -n_e e(\mathbf{E} + \mathbf{v_e} \times \mathbf{B}), \tag{2.2}$$

where n_e is the number density of electrons and m is the mass of the electron. The electrons exchange their momentum with the ions of the metal through collisions, and the body force acting on the ions can be written as:

$$\mathbf{f} = NZ_e(\mathbf{E} + \mathbf{v_i} \times \mathbf{B}) + n_e(m\mathbf{v_e})/\tau, \tag{2.3}$$

where N, Z_e and $\mathbf{v_i}$ are respectively the number density, charge and velocity of ions. By using Equation (2.2) in (2.3) it can be shown that [7]:

$$\mathbf{f} = -n_e e\mathbf{v_e} \times \mathbf{B}, \tag{2.4}$$

noting that, $NZ_e = n_e e$ and that the velocity of the ions is negligible compared to that of the electrons. This reduces to Equation (2.1), as the term $-n_e e\mathbf{v_e}$ is the eddy current density.

The Lorentz force effect takes places in any conducting metal; if the sample is ferromagnetic a further principle contributes to the generation of elastic waves: the so-called magnetostriction [11, 12]

There are two different types of magnetostriction [12]: spontaneous magnetostriction and field induced magnetostriction . The former takes place when a ferromagnet is cooled through its Curie temperature. Above the Curie temperature the magnetic dipoles are randomly aligned, due to the thermal excitation. However, below the critical temperature a large number of close-by magnetic dipoles aligns to a given directions, forming the magnetic domains. The alignment of the magnetic dipoles within a domain results in a spontaneous magnetization of the domain along a certain direction and is associated with a spontaneous strain. The average deformation of the whole ferromagnetic material is the average of the deformations of the single domains, and is referred to as spontaneous magnetostriction. For an isotropic material, this causes a change in the volume of the solid but not in the shape of the specimen. On the other hand, the second type of magnetostriction, the field induced magnetostriction, causes pure shear strains, with no changes in volume. When a magnetic field is applied to a ferromagnetic material (below the Curie temperature) a preferred direction arises towards which the magnetic domains tend to align. This results in a net strain in the direction of the applied field and in a transverse magnetostriction which is half the magnitude and opposite in sign to the strain along the magnetization direction, such that volume is conserved [12]. EMATs can exploit field induced magnetostriction: a dynamic field superposed on a bias field results in dynamic total magnetic field that causes dynamic stresses in the material, that propagate in the form of elastic waves. Throughout this thesis, by "magnetostriction" field induced magnetostriction will be implied. Thanks to reciprocity [13], these physical principles also work in the inverse sense, allowing the detection of ultrasonic waves. A mechanical wave travelling in a conductive medium causes dynamic currents that combined with a static magnetic field induce an electric field in a coil, proportional to the speed of the metal particles in the material (inverse Lorentz mechanism). An inverse magnetostriction phenomenon also takes place when the deformation of a ferromagnetic body produces a magnetic flux density variation that can be detected by the coil.

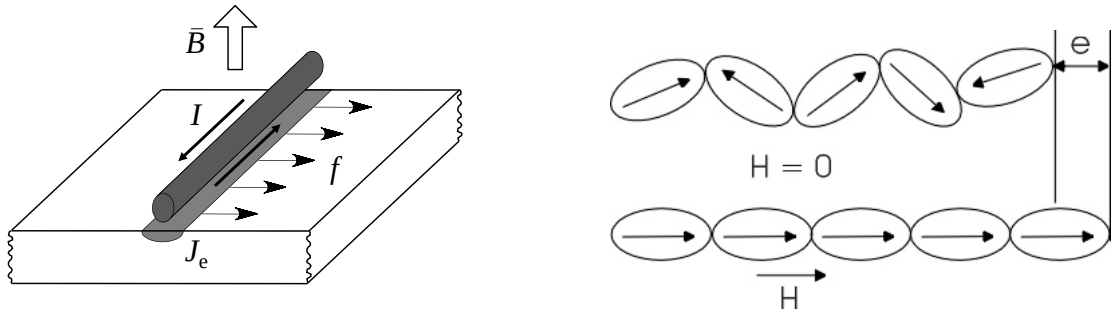

(a) (b)

Figure 2.1: *Fundamental physical principles exploited by an EMAT: (a) Lorentz force. A driving current I induces eddy current density J_e; the interaction with a static magnetic flux density $\bar{B}$ generates volume force density f. Picture adapted from [14]. (b) Magnetostriction. At room temperature, the applied magnetic field H aligns the ferromagnetic domains (here represented for simplicity with an elliptic shape and their magnetization direction with an arrow), and causes a net deformation e. From [12].*

2.3 Advantages and limitations of EMATs

The principles outlined in Section 2.2 exploit electromagnetic induction, hence, operation without any contact is possible. Actually, the efficiency of the transduction decays exponentially with the distance between the sensor and the sample, limiting the practical separation to a few millimetres. However, this tiny gap is enough to give a big advantage over piezoelectric transducers in some applications; high temperature testing is made possible as well as operation on moving samples. Since no contact is needed, couplant fluids do not have to be used which simplifies the operation and minimizes the need for surface preparation; moreover, highly reproducible measurements can be achieved because variability due to the couplant is eliminated. EMATs have been successfully employed in different industrial applications for several decades. For instance, high temperature ($> 1000\,^{\circ}\mathrm{C}$) thickness gaging of seamless steel pipes have been achieved during manufacturing processes using water-cooled permanent magnets (or electromagnets) [7]. Another example of EMAT application is in steel sheet production, where the rolling process causes preferred orientations in the microstructure of the samples, resulting in anisotropy

in the elastic and electromagnetic properties. A pair of EMATs separated by a known distance can be used to measure the speed of sound at different angles from the rolling direction, yielding important information on the formability of the metal sheets [15, 16]. Here the lack of couplant between the transducer and the sample is the key factor to obtain a fast scan of the plate in several directions. Another main advantage of EMATs is the large variety of ultrasonic modes that can be generated. A careful design of the geometry of the coil and the magnet and their relative position allows the excitation and detection of complex wave patterns. EMATs have been used to generate and detect bulk longitudinal and shear waves, Lamb and Shear Horizontal waves in plate-like structures as well as torsional, flextural and longitudinal modes in pipes and wires [5–7, 17]. A classification of the most common configurations of EMATs will be given in the next section (2.4).

The contact-less nature of EMATs comes at a price of some disadvantages: first of all, these transducers are extremely inefficient when compared to traditional sensors. The signal-to-noise ratio is rather poor if the transducer is not carefully designed and special electronics are not employed [18]. Another major problem of EMATs is that their performance can vary with the electromagnetic properties of the sample: a sensor working perfectly on one metal can give low-quality signals when operated on another material. Further, the principles on which EMATs rely to generate and detect ultrasonic waves imply that only good elctrical conductors can be tested. Important non-conductive engineering materials, such as composites, plastics or ceramics, cannot be inspected with EMATs. Table 2.1 summarizes the main advantages and the disadvantages of electromagnetic acoustic transducers.

2.4 EMAT classification

Many EMAT configurations have been proposed to excite different kinds of ultrasonic waves. This section will cover only the most popular and useful types; in-depth classifications of EMATs can be found in the literature; more than ten different configurations with related variants have been reported [5–7].

Table 2.1: *Summary of the advantages and disadvantages of EMATs.*

Advantages	Disadvantages
No contact	Low signal-to-noise ratio
No couplant needed	Special electronics required
Multiple mode excitation	Material-dependent
High temperature inspection	Working only on good conductors
High speed inspection	or highly magnetostrictive metals
Reproducibility	

One of the most common and simplest configurations is the so-called spiral coil EMAT, also known as pancake coil EMAT (Figure 2.2 (a)). As the name implies, the coil is a wire wound in order to make a flat spiral shape. The applied magnetic field is normal to the surface of the sample. As a result, radially polarized shear waves are produced. In practice, the situation is more complex: the static magnetic field often has some non-zero component in the direction parallel to the sample, and the dynamic magnetic field induced by the coil is mainly parallel to the surface of the material as well. This leads to the generation of longitudinal waves travelling in the direction normal to the surface of the sample. However, when the transducer is employed on ferromagnetic material, the situation changes: the magnetization force arising in this case tends to cancel out the normal component of the Lorentz force [19–21], making the generation of longitudinal waves extremely inefficient (Section 3.2.3). This sensor finds wide application in thickness gaging of samples as well as in flaw detection.

Another common configuration is depicted in Figure 2.2 (b). It is referred to by different names: racetrack coil EMAT, elongated spiral coil EMAT or split magnet EMAT [5,22]. The magnetic field and current distributions both reverse on opposite long sides of the racetrack coil so the net effect is a force in the same direction. The overall effect is the generation of linearly polarized shear waves, propagating normal to the surface. Thanks to this feature, this sensor can be employed to study anisotropic samples, where waves have different velocities along different polarization

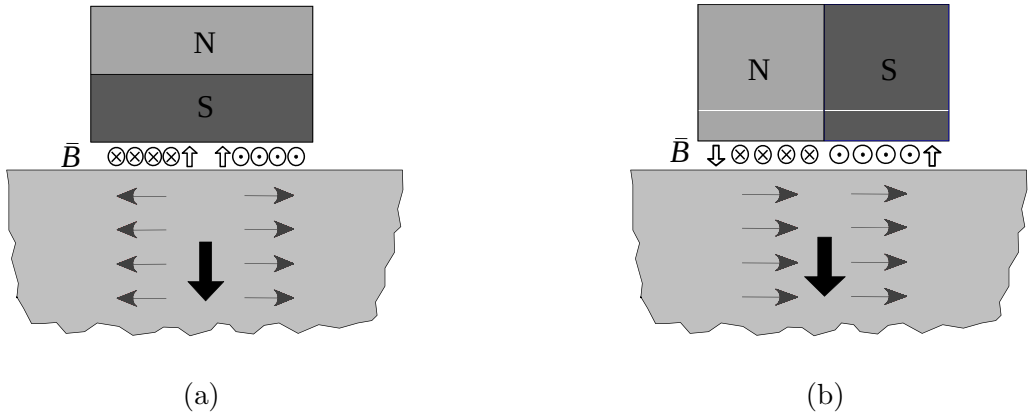

(a) (b)

Figure 2.2: *EMAT classification. Transducers generating ultrasonic beams normal to the surface of the sample. (a) Spiral (pancake) coil EMAT (b) Elongated spiral coil or split magnet EMAT. Arrow convention: thick black for the propagation direction; grey for the polarization direction; hollow arrows indicate the static magnetic flux density. Pictures adapted from [14].*

directions (acoustic birefringence [7, 23, 24]). An equivalent EMAT for longitudinal waves can be obtained when the applied magnetic field is tangential [5, 6]. If the sensitive area of the coil runs normal to the field, and parallel to the sample, linearly polarized longitudinal waves are excited (Figure 2.3 (a)).

The configurations introduced so far are suited for bulk wave generation and detection. When surface waves or guided modes of plates and pipes have to be excited, other EMATs can be employed. A meander coil in conjunction with a normal field causes a series of alternating tractions parallel to the surface of the sample. As a result, surface waves, with a wavelength equal to double the spacing between the wires, are excited [6, 7]. In bulk samples this EMAT configuration generates shear and longitudinal waves propagating obliquely (Figure 2.3 (b)).

Periodic permanent magnet (PPM) EMATs [5, 25] are made of an array of magnets having alternating magnetization directions, all normal to the sample surface. Between the array and the sample, straight wires carry the driving current (Figure 2.4 (a)). Tractions parallel to the surface, alternating with a periodicity equal

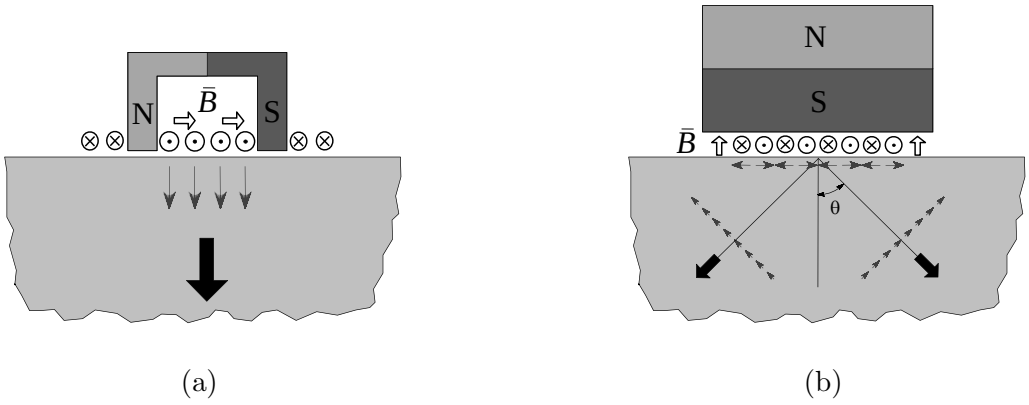

(a) (b)

Figure 2.3: *EMAT classification. (a) Longitudinal wave EMAT (b) Meander coil EMAT. Arrow convention: thick black for the propagation direction; grey for the polarization direction; hollow arrows indicate the static magnetic flux density. Pictures adapted from [14].*

to twice the width (x_1 direction) of the magnets are induced. The resulting waves are Shear Horizontal (SH) waves. SH waves are attractive for NDT purposes and are generally not easily excited with traditional transducers, thus, this configuration can be extremely valuable in applications. The wavelength of the SH waves is dictated by the width of the magnets of the array; hence, small wavelengths require thin magnets. Unfortunately, magnets whose width is less than 1 mm usually give small magnetic fields, so, in the case of SH guided waves, the sensor works efficiently only below a certain frequency limit, roughly 1 MHz.

Another EMAT design for SH wave generation on ferromagnetic metals relies on magnetostriction only [26, 27]. A meander coil is placed within a tangential magnetic field (Figure 2.4 (b)). Since the Lorentz effect is not the transduction principle exploited, the sensor works even when the field and the wires of the coil are parallel. The static magnetic field and the dynamic field due to the driving current are perpendicular to each other, causing only a change in the direction of the total magnetic field, not in its magnitude. This produces shear strains below the wires that generate SH waves. A similar concept has been applied successfully to generate a range of modes on ferromagnetic plates and pipes [17, 28].

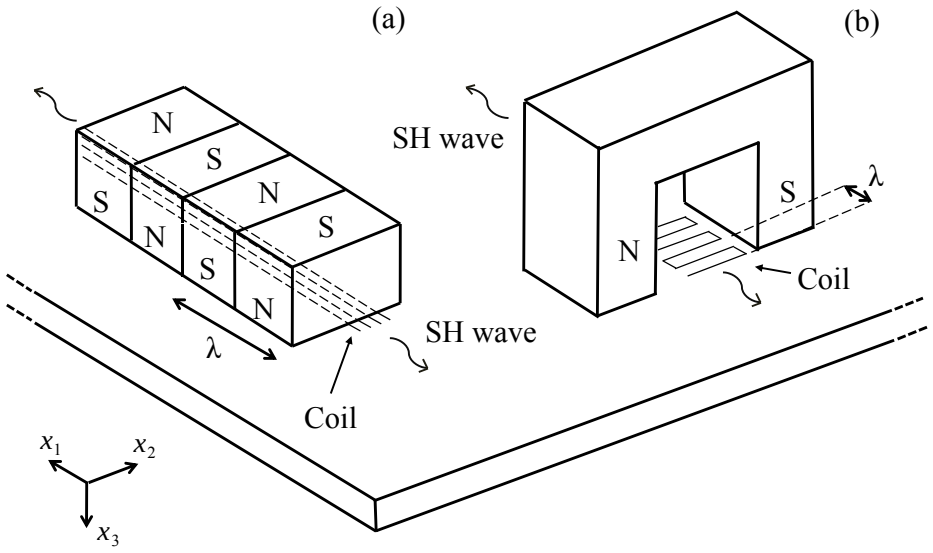

Figure 2.4: *EMAT classification. Schematic diagram of (a) periodic permanent magnet (PPM) and (b) magnetostrictive EMATs on a plate. The polarization of the magnets, the coils and the propagation direction are shown.*

2.5 History of EMAT development and modelling

The following literature review outlines some of the major steps in the development of EMATs. Over the years, many authors have proposed theoretical and numerical models to describe the transduction mechanisms, in order to improve the low signal-to-noise ratio of the sensors and to increase the understanding of EMATs physics. This historical overview presents the evolution EMAT modeling up to the current state-of-the-art models. While pointing out the main modeling advances, some significant experimental developments will also be highlighted.

It is hard to determine who was the "inventor" of electromagnetic acoustic transducers [7]. The physical principles underlying their operation were known since the early studies on fundamental electromagnetism: Maxwell had included what was later known as the Lorentz force in the equations of electromagnetism in 1861 [29], while Joule had already reported on the magnetostrictive effect in 1847 [30]. How-

ever, only over a century later, with the advances in all scientific and technological fields, the first EMATs were proposed for Non Destructive Evaluation purposes. Apparently [7], the kick-start was given by studies on helicons (low-frequency electromagnetic waves) by Grimes and Buchsbaum [31] in the early sixties of the last century. Following this work, Gaerttner *et al.* observed ultrasound generation caused by magnetic body forces [32]. In 1973, Dobbs [8] started an investigation on ultrasonic waves generated by electromagnetic mechanism. He concluded that the forces were due to the Lorentz effect and pointed out that the phenomenon could be useful for Non-Destructive Testing.

In the same year, Thompson [9] described the generation of Rayleigh and Lamb waves in metal plates, using a meander coil EMAT. He formulated an analytical model including the Lorentz force mechanism and studied the lift-off dependence of the generated signal. The classical electrodynamics equation describing the eddy current induced on a metal surface by an infinite current-carrying wire was used to model the effect of a single wire of the coil. Then a spatial Fourier analysis was adopted to model a full two-dimensional meander coil. Later, Thompson concentrated on the study of magnetostriction: in 1977 he addressed the efficiency of the transduction mechanism on different ferromagnetic materials [33]. In particular, he studied the dependence of the signal amplitude on the applied magnetic field, finding that magnetostriction is usually dominant for low magnetic fields when the static field is parallel to the surface of the sample. In this case the relationship between the signal amplitude and the bias magnetic field is highly non-linear and severely material-dependent. On the other hand, when the magnetic field increases, magnetostriction saturates and no longer contributes to the force generation, whereas the Lorentz force increases linearly with the magnetic field. Thus, the overall relationship between the magnetic field and force generated for high fields is linear, whatever the material. In 1978, Thompson [19] gave an overview of the equations governing EMAT operation, including a third generation effect, the magnetization force, which was demonstrated to be minor compared to the other mechanisms. Another remarkable achievement of Thompson (together with Vasile) in those years is

the proposal of a new kind of EMAT: the periodic permanent magnet EMAT [25]. Such a transducer is capable of exciting shear horizontal (SH) waves in plates, a non-trivial task for traditional piezoelectric transducers. A further advance was due to Höeller and Mohr, who produced the first guided-wave EMATs for pipe inspection [34]. Using longitudinal and torsional modes, they investigated the reflections due to flaws in ferritic and austenitic pipes. It has to be pointed out that their approach was purely empirical.

A major improvement in the modeling of spiral coil EMATs, operating on non-ferromagnetic metals, was made by Kawashima in 1976 [10]. He modelled the coil as the superposition of several circular loops, lying on planes parallel to the surface of the sample, at a certain distance. This assumption allowed him to use the well-known Dodd and Deeds model [35], originally proposed in 1968 to model eddy-current probes. The model solves the electrodynamics equations in steady-state conditions, using a magnetic vector potential formulation, together with an axisymmetric geometry. The analytical solution obtained is in the form of an integral of Bessel functions and can easily be computed numerically. Kawashima used this relationship together with the experimentally measured magnetic flux density to predict the Lorentz forces produced by a pancake coil EMAT. The further assumption employed was that the forces could be regarded as superficial forces rather than body ones, as they are concentrated within the electromagnetic skin depth, which is usually much smaller than the wavelength of elastic waves. In this way, he could use a modified piston source model [36] to predict the acoustic field. Kawashima's model, in contrast with previous models, was the first one to give useful equations for the actual design of the transducer: practical parameters, such as the dimensions of the coil and the number of turns, appear in the equations, and are directly linked to the generation and reception efficiencies of the sensor. In 1984, Kawashima [37] extended his analysis to transient excitation, using Fourier analysis. The comparison between his predictions and the experimental results showed good qualitative agreement, but quantitatively, the discrepancy was between 30% and 50%, probably because of the number of approximations he had to make in the theoretical analysis.

The works of Il'in and Kharitonov [20], and Wilbrand [38,39] in the eighties have defined analytical models for magnetostriction, in terms of elastic and electromagnetic constitutive equations linked by coupling terms accounting for the magneto-mechanical transduction, in analogy with piezoelectric equations. These studies have been successfully validated, but only in a qualitative way, i.e. with an arbitrary scaling parameter; moreover the solutions are available only for very simple geometric configurations and a number of simplifying assumptions is required.

The widespread development of numerical methods, such as the finite difference method and the finite element method, was crucial in the formulation of realistic EMAT models. In the early nineties, Ludwig and co-workers proposed a two-dimensional FE code, modelling all the generation mechanisms, with an arbitrary transient excitation [40–45]. The inhomogeneous magnetic field due to an electromagnet was also included. This allowed the study of more complex systems, for example a variable lift-off coil, driven by a tone-burst excitation current. Though Ludwig's theoretical analysis was comprehensive and consistent with analytical solutions available, the results were never validated against experiments. In particular, magnetostrictive effects were modeled with a matrix of coefficients, but there was no further insight on this phenomenon, either theoretical or empirical.

Some new light was shed on this issue by Ogi in 1997 [21]. In this article a full analytical description of a two dimensional meander coil EMAT was presented. A detailed treatment of magnetostrictive effects is given, both in generation and reception of ultrasonic waves, and the equations are used in conjunction with an experimentally determined magnetostriction curve. Ogi's main finding is the derivation of equations to compute the magnetostrictive parameters from experimental data. In disagreement with Thompson and Wilbrand, who had regarded magnetostriction as the main transduction mechanism only when the bias field is parallel to the surface of the sample, Ogi claimed that even for normal bias field configurations magnetostriction is the dominant mechanism, being one or two order of magnitudes larger than the Lorentz effect. This model was only qualitatively validated by ex-

periments, leaving the issue of the relative weight of transduction mechanisms not fully clarified.

An indirect verification of the importance of magnetostriction in the transduction process was given by Kwun and co-workers [17, 46, 47] and by Murayama and collaborators [28, 48, 49]. Both groups generated and detected longitudinal, torsional and flexural waves in ferromagnetic rods or tubes, relying on magnetostriction only. Kwun's sensor is essentially a coil wound circumferentially around the pipe and subjected to a bias magnetic field, orientated according to the kind of wave to be generated or detected. These studies have clearly confirmed the importance of magnetostrictive effects, at least in configurations where the bias field is parallel to the surface of the sample. The analysis is purely empirical and qualitative, and no theoretical description has been provided yet: the whole design process of these transducers is based on some physical insight together with a trial-and-error approach.

In recent years, enhancements in the design of EMATs were due to Dixon and collaborators from Warwick University. They mainly concentrated their analysis on the Lorentz force mechanism, focusing on the dynamic magnetic field produced by the driving current in the coil. In a study on Rayleigh wave generation [50], FE simulations of the Lorentz force mechanism were used to show that the orientation of the bias field can be chosen such that the Lorentz forces due to the static and dynamic magnetic fields constructively interfere, enhancing signal amplitude [51, 52]. Also, exploiting the self-generated magnetic field interacting with induced eddy currents, it is possible to generate acoustic waves without the need for a permanent magnet or an electromagnet. Dixon and co-workers employed a plate of magnetite iron oxide above the coil to increase the induced magnetic flux density [53, 54]. In other modelling research [55], the presence of two conductive layers was analyzed: the sample and an electrically conductive screen between the coil and the magnet, to reduce ultrasonic generation in the magnet. The extra conductive layer affects the impedance of the coil because eddy currents are induced in both the conductive

media. This leads to the conclusion that the original Dodd and Deeds model has to be modified in order to compute the correct impedance of the coil.

Another recent advance is realistic modelling of the EMAT coil. Shapoorabadi and co-workers at University of Toronto were the first to model the skin effect in a conductive coil, including this effect in a FE model [56–58]. Previous work assumed a uniform distribution of current density on the coil cross-section; this neglected the tendency of current to concentrate on the boundary of the conductor. The authors claim that this phenomenon is not negligible and may be one reason for the large discrepancies observed in the past between some models and experimental data. In [59], the group experimentally validated in a quantitative way a Finite Element model accounting for the Lorentz force mechanism only.

The analysis of previous research shows that even if extensive modelling on EMAT transduction mechanisms has been carried out, there is a lack of an experimentally quantitatively validated numerical model of magnetostriction. The implementation of such a model into a commercial Finite Element software is one of the main contributions of this thesis and is described in chapters 4 and 5.

2.6 Conclusions

A general introduction to Electromagnetic Acoustic Transducers has been presented. EMAT operating principles and their classification were given. This will be the basis for a detailed mathematical analysis of the physics involved in the transducer's behavior which will be covered in the following chapter. A review of past research on EMATs and their modelling was also given, highlighting the main novelty of this work.

Chapter 3

Theory

3.1 Introduction

This chapter describes the physics underlying the operation of EMATs. The purpose is to provide a solid mathematical basis that can be used in the modelling of the device. An in-depth analysis of each of the transduction mechanisms is given. The electrodynamic equations governing the Lorentz and magnetization mechanisms are introduced and used in conjunction with standard elasticity theory to describe wave generation and reception. Magnetostriction is included in the model via appropriate constitutive equations that, in an analogy with piezoelectricity, link the elastic field with the electromagnetic field. The magneto-mechanical coupling is expressed by a magnetostriction matrix whose coefficients can be deduced from experimental data.

EMATs are able to generate and detect elastic waves in a solid exploiting three different electromagnetic phenomena [6, 7, 38]. The Lorentz force acts on any conducting material, both ferromagnetic and non-ferromagnetic. It arises because of the interaction of the magnetic flux density with the eddy currents generated in the solid by the dynamic current passing through the coil of the sensor. On the other hand, the two remaining mechanisms, magnetization force and magnetostriction, operate only on ferromagnetic materials. The former appears when the dynamic

electromagnetic field caused by the driving current interacts with the magnetization induced in the material, generating a body force. The latter, magnetostriction, consists in the deformation taking place in a ferromagnetic media when subject to a magnetic field. Since the magnetic field generated by the driving current is dynamic, the deformation induced in the sample is time-dependent too, leading to the generation of mechanical waves.

3.2 Lorentz and magnetization mechanisms

3.2.1 Governing equations

EMAT generation of elastic waves relies on electromagnetic phenomena that can be described by Maxwell's equations (Faraday's law and Ampére's law) [7, 12, 21]:

$$\nabla \times \mathbf{E} = -\frac{\partial \mathbf{B}}{\partial t}, \tag{3.1}$$

$$\nabla \times \mathbf{H} = \mathbf{J} + \frac{\partial \mathbf{D}}{\partial t}, \tag{3.2}$$

and

$$\nabla \cdot \mathbf{B} = 0, \tag{3.3}$$

$$\nabla \cdot \mathbf{D} = \rho_q, \tag{3.4}$$

and with the constitutive relations:

$$\mathbf{J} = \sigma \mathbf{E}, \tag{3.5}$$

$$\mathbf{B} = \mu_0 \left(\mathbf{H} + \mathbf{M} \right), \tag{3.6}$$

where $\mathbf{E}$ and $\mathbf{D}$ are the electric field and displacement, respectively; $\mathbf{J}$ is the current density, $\mathbf{B}$ and $\mathbf{H}$ are the magnetic flux density and the magnetic field, $\mathbf{M}$ is the magnetization, μ_0 and σ are the magnetic permeability of free space and the electric conductivity, and ρ_q is the charge density. The term $\partial\mathbf{D}/\partial t$ is usually dropped in all the regions of the system, as its contribution is negligible for frequencies lower than 100 MHz (quasi-static approximation) [60]. The solution to this set of equations can be used to compute the dynamic forces $\mathbf{f}$ acting on the elastic body:

$$\mathbf{f} = \mathbf{f}_L + \mathbf{f}_M, \tag{3.7}$$

where $\mathbf{f}_L$ and $\mathbf{f}_M$ are respectively the Lorentz and magnetization body forces, defined as:

$$\mathbf{f}_L = \mathbf{J}_e \times \mathbf{B}, \tag{3.8}$$

$$\mathbf{f}_M = \nabla\mathbf{H} \cdot \mu_0\mathbf{M}, \tag{3.9}$$

where $\mathbf{J}_e$ is the eddy current density induced in the sample. Here $\nabla\mathbf{H}$, the gradient of the magnetic field, is a 3×3 second-order tensor whose (i, j) element in cartesian coordinate is $\partial H_j/\partial x_i$. Each component of the magnetization force can be expressed as $f_k = \mu_0 M_i(\partial H_i/\partial x_k)$, where the summation convention is implied. This set of interactions can then be used as the external force operating on a continuous elastic isotropic medium, in order to compute the acoustic field [10, 58]:

$$\breve{\mu}\nabla \times \nabla \times \mathbf{u} - \left(\breve{\lambda} + 2\breve{\mu}\right)\nabla\nabla \cdot \mathbf{u} + \rho\frac{\partial^2\mathbf{u}}{\partial t^2} = \mathbf{f}, \tag{3.10}$$

where $\breve{\mu}$ and $\breve{\lambda}$ are Lamé's constants (the accents are used to avoid confusion with the magnetic permeability, μ and the elastic wavelength, λ), $\mathbf{u}$ is the displacement vector, and ρ is the mass density. The approach outlined is hierarchically coupled: the solution of equations from (3.1) to (3.6) allows the computation of the external force in Equation (3.10) by using equations from (3.7) to (3.9); this is described in Section 3.2.4 with further details. Analytical solutions exist only for a small number of simple cases, using simplifying assumptions [6, 7, 21, 37].

3.2.2 Lorentz force

The dynamic current density, $\mathbf{J}$, flowing in the coil, induces a mirror eddy current density, $\mathbf{J}_e$, in the conducting solid, opposing the original current, according to Faraday's law (Equation (3.1)). The induced current is mainly confined in a superficial portion of the sample, which can be quantified by the so-called "skin depth" parameter, δ. For a sinusoidal plane electromagnetic wave of frequency f, impinging on a material with conductivity σ and permeability $\mu_0\mu_r$, δ is defined as [12]:

$$\delta = \frac{1}{\sqrt{\pi f \sigma \mu_0 \mu_r}}. \tag{3.11}$$

The eddy current interacts with the magnetic flux density yielding a body force, according to Equation (3.8). The magnetic flux density is actually made up of two different contributions: the static field due to the magnet, $\bar{\mathbf{B}}$, plus the dynamic field generated by the driving current, $\widetilde{\mathbf{B}}$:

$$\mathbf{B} = \bar{\mathbf{B}} + \widetilde{\mathbf{B}}. \tag{3.12}$$

Throughout this thesis we will denote static quantities with a bar, as opposed to dynamic ones, designated with a tilde. The overall Lorentz force is thus:

$$\mathbf{f}_L = \mathbf{f}'_L + \mathbf{f}''_L = \mathbf{J}_e \times \left(\bar{\mathbf{B}} + \widetilde{\mathbf{B}}\right). \tag{3.13}$$

If the generating current is sinusoidal, with frequency f (or angular frequency $\omega = 2\pi f$), both the induced eddy current and the dynamic magnetic flux density will be harmonic, oscillating at the same frequency, while the static magnetic field produced by the magnet remains constant:

$$\begin{cases} \mathbf{J}_e, \widetilde{\mathbf{B}} & \propto & \sin(\omega t) \\ \bar{\mathbf{B}} & = & \text{const.} \end{cases}. \tag{3.14}$$

Equation (3.13) implies that the contribution to the Lorentz force due to the permanent magnet oscillates with the same frequency as the driving current f, while

the component due to the self-induced field has a double frequency, $2f$:

$$\begin{cases} \mathbf{f}'_L & \propto \sin(\omega t) \\ \mathbf{f}''_L & \propto \sin(\omega t) \cdot \sin(\omega t) \propto \cos(2\omega t) \end{cases}. \tag{3.15}$$

In most practical cases, the static magnetic flux density is much bigger than the dynamic one. However, if the driving current is extremely large (more than 100 A), the sensor can work without the help of a permanent magnet or an electromagnet, but at double frequency [7, 53, 54].

3.2.3 Magnetization force

The gradient of the magnetic energy density $\mathcal{U}_M$ of a magnetized sample within a magnetic field gives the expression of the magnetization force, that is [61]:

$$\mathbf{f}_M = -\nabla \mathcal{U}_M = \nabla \mathbf{H} \cdot \mu_0 \mathbf{M}. \tag{3.16}$$

It has been shown both experimentally [19,62,63] and theoretically [7] that, in EMAT configurations with bias field tangential to the sample, the components of the Lorentz force and the magnetization force in the direction normal to the sample have similar amplitudes but are out of phase, tending to cancel each other. For this reason, these mechanisms are not able to generate compressional waves in ferromagnetic materials. Also, the contribution of the magnetization force to shear wave generation in this configuration is relatively small and will be neglected in following chapters of this thesis.

3.2.4 Ultrasonic field

Once the electromagnetic equations have been solved for a certain geometry and set of physical parameters, and the dynamic body force has been computed, it is possible to predict the ultrasonic field generated by the transducer. The governing equation, in the case of an elastic, isotropic medium is Navier's Equation (3.10). Generally,

the solution of this equation requires the use of numerical methods. However, some assumptions allow approximate solutions in special cases. An approach used by several authors takes advantage of the fact that all the dynamic forces generated by EMATs act in a small portion of the solid, that is, within a depth comparable to the skin depth [6, 10, 37]. Since the skin depth is usually much smaller than the wavelength (for example, in aluminum for shear waves, with $f = 2\text{MHz}$, $\delta \cong 0.08\text{mm}$ while $\lambda \cong 1.50\text{mm}$), the body forces are modelled as surface ones, whose values are obtained by integrating the original forces along the depth. This method allows the application of classical solutions of the ultrasonic field, such as the "piston source" model [36]. It has to be pointed out that the outlined approach neglects any mutual coupling, that is, the magnetic field generated by the induced acoustic wave is not taken into account during the wave generation process. This effect is often regarded as a second order effect as its magnitude is considered very weak. The fact that uncoupled FE models such as that presented in [59] have been experimentally validated supports the soundness of this approximation.

3.2.5 Reception process

The same physical principles that allow EMATs to generate elastic waves can be exploited to obtain an electrical signal from a mechanical wave travelling in the vicinity of the sensor. The dynamic displacement field causes a reciprocal Lorentz effect in any metal. A time-varying displacement in a conductive medium, in the presence of a static magnetic flux density $\bar{\mathbf{B}}$, results in an induced electric field:

$$\mathbf{E} = \frac{\partial \mathbf{u}}{\partial t} \times \bar{\mathbf{B}}. \tag{3.17}$$

This field produces a current loop in the conducting material and the resulting varying magnetic field is picked-up by the coil of the transducer, and a voltage signal proportional to the velocity of the wave can be output.

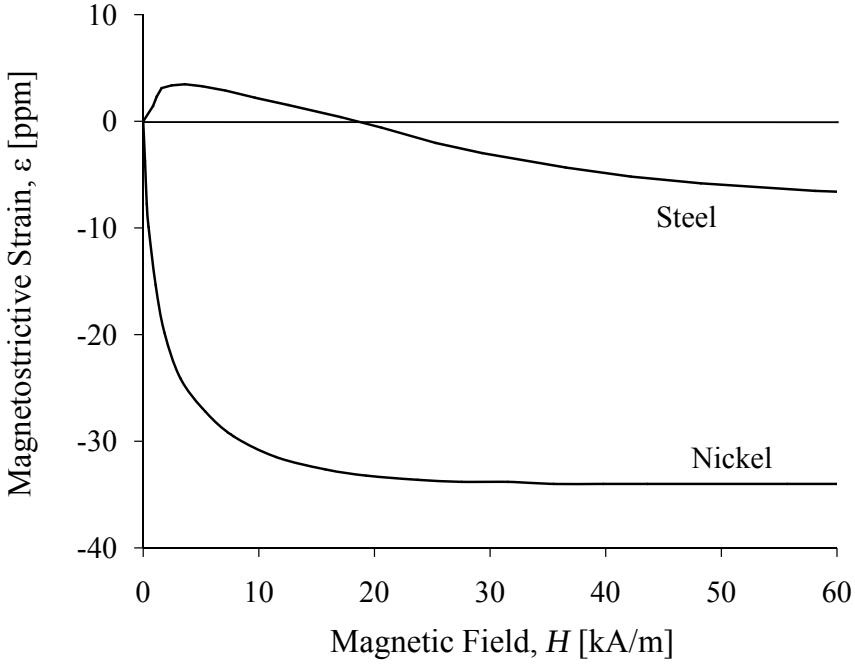

Figure 3.1: *Static magnetostriction curves of nickel and mild steel. From [11, 12].*

3.3 Magnetostriction

Ferromagnetic metals undergo dimensional changes when exposed to a magnetic field. This phenomenon is referred to as Joule magnetostriction (Figure 3.1). The magnetostriction data shown throughout this thesis refer to static conditions where a dc magnetic field is applied and the resulting static strain is measured. The reciprocal phenomenon, the so-called Villari effect, consists of a variation of the magnetic field due to a deformation occurring in a magnetic metal [64,65]. While the Lorentz and magnetization force can be modelled as body tractions or compressions applied to an elastic solid, magnetostriction takes the form of elastic strains that can be modelled by appropriate constitutive equations. In general, magnetostrictive constitutive relations are non-linear and can be expressed as [66]:

$$\begin{cases} \epsilon = f(\sigma, \mathbf{H}) \\ \mathbf{B} = g(\sigma, \mathbf{H}) \end{cases}, \tag{3.18}$$

where ϵ and σ are the strain and stress tensors and $\mathbf{B}$ and $\mathbf{H}$ are the magnetic flux density and the magnetic field strength respectively. The first equation includes the

direct magnetostrictive effect (Joule magnetostriction), while the second equation includes the inverse magnetostriction (Villari effect) [11]. These equations are not single-valued, as magnetostriction usually shows a certain degree of hysteresis.

It is possible to approximate the coupled magnetostrictive equations by analogy with piezoelectricity, with the difference that the electric field is replaced by the magnetic field:

$$\begin{cases} \epsilon &= S^H \, \sigma + \mathcal{D} \, \mathbf{H} \\ \mathbf{B} &= \mathcal{D}^T \, \sigma + \mu^\sigma \, \mathbf{H} \end{cases} . \tag{3.19}$$

The mechanical quantities are related by the elastic compliance matrix S^H (6×6), measured when $\mathbf{H}$ is constant, and the magnetic quantities are related by the magnetic permeability matrix μ^σ (3×3), at constant stress. The magneto-mechanical coupling is expressed by the magnetostriction matrix $\mathcal{D}$ (6×3).

These equations assume a linear magnetostriction curve, i.e. the strain is a linear function of the magnetic field. It is known experimentally that materials actually exhibit a highly nonlinear behaviour [11, 12] (Figure 3.1). However, in the case of EMATs, a small dynamic magnetic field $\widetilde{\mathbf{H}}$ is superimposed on a much larger static bias field $\bar{\mathbf{H}}$, such that $\bar{H} \gg \widetilde{H}$. In this case, there is only a small oscillation of the magnetic field around the operation point $\bar{H}$, such that the linear assumption is locally valid. Hysteresis is also neglected as this effect greatly complicates the analysis without significantly affecting the analysis, at least within the strong bias field hypothesis.

When the small dynamic magnetic field $\widetilde{\mathbf{H}}$ is superimposed on a large static bias field $\bar{\mathbf{H}}$, the resulting strain can be decomposed into a static $\bar{\epsilon}$ and a dynamic component $\widetilde{\epsilon}$ (the same considerations apply to σ and $\mathbf{B}$):

$$\begin{cases} \mathbf{H} &= \bar{\mathbf{H}} + \widetilde{\mathbf{H}} \\ \epsilon &= \bar{\epsilon} + \widetilde{\epsilon} \end{cases} . \tag{3.20}$$

As a result, the constitutive equations (3.19) can also be rewritten in terms of their dc and dynamic components. The static magnetic field causes constant volume

deformations when applied on a ferromagnetic material:

$$\begin{cases} \bar{\epsilon} &= S^H \, \bar{\sigma} + D \, \bar{\mathbf{H}} \\ \bar{\mathbf{B}} &= D^T \, \bar{\sigma} + \mu^\sigma \, \bar{\mathbf{H}} \end{cases} . \tag{3.21}$$

In an elastically isotropic material and within the linear approximation, the magnetostrictive strain along the magnetization direction is directly proportional to the applied field through a constant, D_{11}, which is a material property. The magnetostrictive strain in any direction orthogonal to the magnetization axis is half the magnitude and opposite in direction to the strain along the magnetization direction. In this way, the continuity relationship ($\epsilon_1 + \epsilon_2 + \epsilon_3 = 0$) is satisfied, and volume is conserved. This also implies that there is no shear magnetostrictive strain in the directions parallel and orthogonal to the magnetization axis. As a result the static magnetostriction matrix D can be written as:

$$D = \begin{bmatrix} D_{11} & -\frac{1}{2}D_{11} & -\frac{1}{2}D_{11} \\ -\frac{1}{2}D_{11} & D_{11} & -\frac{1}{2}D_{11} \\ -\frac{1}{2}D_{11} & -\frac{1}{2}D_{11} & D_{11} \\ 0 & 0 & 0 \\ 0 & 0 & 0 \\ 0 & 0 & 0 \end{bmatrix} . \tag{3.22}$$

It has to be pointed out that the static constitutive equations (3.21) are less valid than their analogous counterparts of piezoelectricity, because of the high non-linearity of magnetostriction. Equations (3.21) are reported for completeness only and will not be used in the subsequent analysis. The dynamic component of the constitutive equations can be approximated by its leading linear term that connects the fundamental harmonics of the strain and magnetic field:

$$\begin{cases} \widetilde{\epsilon} &= S^H \, \widetilde{\sigma} + d \, \widetilde{\mathbf{H}} \\ \widetilde{\mathbf{B}} &= d^T \, \widetilde{\sigma} + \mu^\sigma \, \widetilde{\mathbf{H}} \end{cases} , \tag{3.23}$$

where d is the dynamic magnetostriction matrix. It has to be stressed that the linearized approximation of Equation (3.23) is valid in the strong bias field approx-

imation, even when the linearization of the static constitutive equations (Equation (3.21)) is not applicable. The configuration d depends on the direction of the magnetization, if the static field lies along the x_2 direction in a reference system $\{x_1, x_2, x_3\}$, it can be written as [7, 27]:

$$d = \begin{bmatrix} 0 & -\frac{d_{22}}{2} & 0 \\ 0 & d_{22} & 0 \\ 0 & -\frac{d_{22}}{2} & 0 \\ 0 & 0 & d_{61} \\ 0 & 0 & 0 \\ d_{61} & 0 & 0 \end{bmatrix}^{T}. \tag{3.24}$$

The presence of a strong bias field causes the material to appear anisotropic for a superimposed dynamic magnetic field, even if the material is statically isotropic. This phenomenon is analogous to acoustoelasticity, where a large static bias stress causes a weakly nonlinear but isotropic material to appear linear but slightly anisotropic for a small superimposed dynamic stress [67]. Equation (3.24) shows that the material appears to be transversely isotropic, with the plane of isotropy normal to the magnetization axis. The matrix is characterized by two independent terms that account for different physical phenomena. The coefficient d_{22} accounts for the normal dynamic strain $\widetilde{\epsilon}_2$ along the magnetization direction $\bar{H}_2$, caused by a dynamic magnetic field acting in the same direction $\widetilde{H}_2$:

$$d_{22} = \left(\frac{\partial \epsilon_2}{\partial H_2}\right)_{\bar{H}_2.} \tag{3.25}$$

This is the first derivative of the magnetostriction curve with respect to the magnetic field, at the operation point $\bar{H}_2$. Since $\widetilde{H}_2$ and $\bar{H}_2$ are parallel, the total magnetic field changes over time, while its direction is constant; as a consequence, d_{22} represents the modulation of the magnitude of the bias magnetic field. On the other hand, when the dynamic field component $\widetilde{H}_1$ (or $\widetilde{H}_3$) is orthogonal to the static field $\bar{H}_2$, in the strong bias approximation $\bar{H} \gg \widetilde{H}$, the magnitude of the total field, $\mathbf{H} = \widetilde{\mathbf{H}} + \bar{\mathbf{H}}$, does not change (at least at the fundamental frequency of the dynamic field), while its direction tilts slightly. In other words, d_{61} represents the dynamic modulation

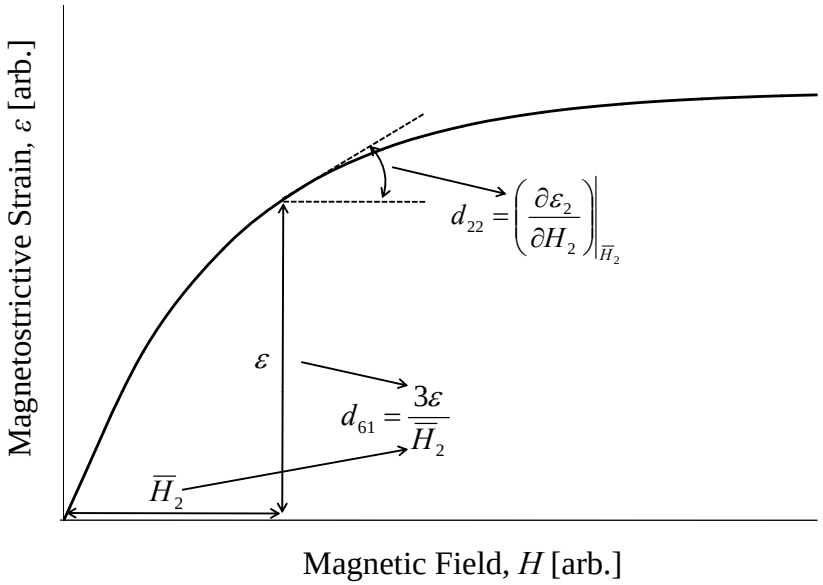

Figure 3.2: *Calculation of the magnetostriction constants d_{22} and d_{61}, at a given operation point $\bar{H}_2$, from a generic magnetostriction curve, according to Equations (3.25) and (3.26).*

of the direction of the bias field. Analyzing this rotation and applying a coordinate transformation, Ogi and Hirao [7] have shown that this parameter can be correlated to the total magnetostrictive strain ϵ, i.e. the strain parallel to the total field, and the bias magnetic field:

$$d_{61} = \frac{3\epsilon}{\bar{H}_2}. \tag{3.26}$$

All the non-zero coefficients of the matrix (3.24) can be computed from the magnetostriction curve of the material: d_{61} is directly proportional to the total magnetostrictive strain, ϵ (and inversely proportional to the static magnetic field) (Equation (3.26)), while the other coefficient, d_{22}, is proportional to the derivative of the magnetostriction curve at the operation point, Equation (3.25), as shown in Figure 3.2. In other words, once a magnetostriction curve is measured, all the piezomagnetic coefficients can be determined for any level of the bias magnetic field. From Equations (3.25) and (3.26) it is clear that d_{22} and d_{61} are functions of the static magnetic bias field and they depend on the actual shape of the magnetostriction curve of the ferromagnetic material under investigation. An example is given in Figure 3.3,

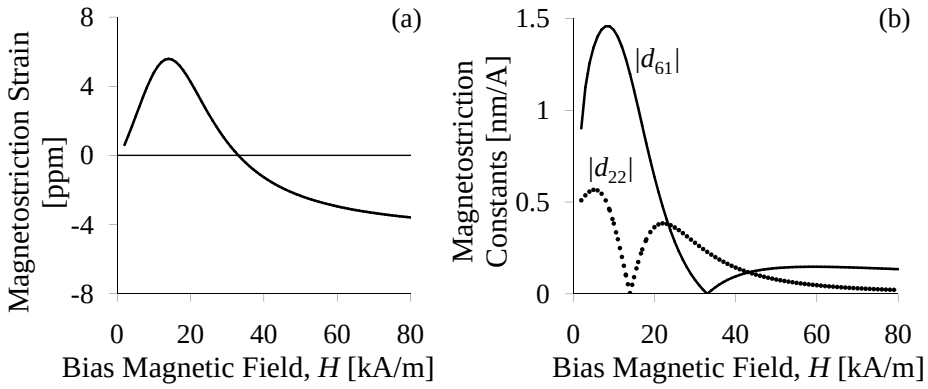

Figure 3.3: *(a) Static magnetostriction curve of EN3 steel. (b) Absolute value of the magnetostriction constants d_{22} and d_{61}, caluculated according to Equations (3.25) and (3.26).*

where the static magnetostriction curve of EN3 steel is shown (Figure 3.3 (a)) together with the absolute value of the magnetostriction constants (Figure 3.3 (b)), d_{22} and d_{61}, computed according to equations (3.25) and (3.26). Since the value of the magnetostriction parameters is a non-linear function of the bias field it can be expected that the amplitude generated by EMATs relying on magnetostriction shows maxima and minima in accordance to magnetostriction properties. This will be discussed in Chapter 5 for SH wave magnetostrictive EMATs operating on nickel and in Chapter 6 for SH wave EMATs operating on steel. It has also to be noted that the coefficient d_{61} is larger than d_{22} for most part, but not the whole range of magnetic bias field considered.

The theory outlined in this chapter relies on the strong bias field approximation, which is usually satisfied in practical EMAT applications. In those cases where the static and the dynamic magnetic field have comparable magnitudes, i.e. $\widetilde{H} \approx \bar{H}$, both the amplitude and the direction of the total magnetic field **H** change and the magnetostriction matrix d takes a more general form. For a bias field along the x_2

direction, Equation (3.24) has to be rewritten as [7]:

$$d^{lowbias} = \begin{bmatrix} d_{11} & d_{21} & d_{31} \\ d_{21} & d_{22} & d_{21} \\ d_{31} & d_{21} & d_{11} \\ 0 & 0 & d_{61} \\ 0 & 0 & 0 \\ d_{61} & 0 & 0 \end{bmatrix}. \tag{3.27}$$

The matrix components d_{ij} have more complex expressions that are essentially a combination of d_{22} and d_{61} of equations (3.25)-(3.26) multiplied by appropiate trigonometric functions of the angle between the dynamic and static magnetic field [7].

Several authors have pointed out that in some ferromagnetic metals, and for specific EMAT configurations, the signal amplitude due to magnetostriction can be dominant over the Lorentz and magnetization forces [6, 21]. This behavior has been experimentally observed when EMATs with magnetic bias field parallel to the surface are operated on materials such as Nickel or steels with oxidized surfaces [17,47]. Even though the importance of magnetostriction in EMAT transduction is widely recognized, the literature review of Section 2.5 highlighted the absence of a fully quantitatively validated numerical model including this effect. The implementation of such a model in a commercial software will be described in the next chapter.

3.4 Conclusions

This chapter analyzed the physical principles that allow an EMAT to generate and detect ultrasonic waves in a metal sample. A description of the electromagnetic and elastic equations that govern the operation of the transducer was given. The different mechanisms involved were addressed in detail from a physical-mathematical point of view. Special emphasis was given to the modelling of magnetostriction described through the addition of a magneto-mechanical coupling matrix in the

standard constitutive equations, whose coefficients are characteristic of each ferromagnetic material.

Chapter 4

Finite Element model

4.1 Introduction

This chapter presents the numerical model used to solve the equations governing EMAT operation. The implementation of the main transduction mechanisms in commercial software is discussed and an introduction to the numerical methods employed by the software is given. The different phenomena involved in the Lorentz force mechanism and magnetostriction make the latter very demanding to model. The choice of mesh size and domain size and the exploitation of symmetries are illustrated through the example of a simple magnetostrictive EMAT configuration. Further methods to reduce the computational requirements of the model, i.e. the use of analytical expression for special geometries and the use of two-dimensional axisymmetry, are covered in the last part of the chapter.

4.2 Model implementation

The equations presented in Chapter 3 give a comprehensive description of the EMAT physics. Unfortunately, they can only be solved analytically in very special conditions, when the geometry of the problem is simple and presents symmetries, and if

several simplifying assumptions are made. In engineering applications, accurate predictions are needed in situations where the geometry is complicated and the material properties have a complex behaviour. The only way to overcome these difficulties is the use of numerical methods. The Finite Element Method (FEM) is currently applied widely in all engineering fields with considerable success. In the present study FE commercial software, COMSOL Multiphysics was adopted. This package solves the partial differential equations (PDEs) that govern electromagnetism and continuum mechanics, and allows a coupled solution of different physical phenomena influencing each other. Moreover, it is possible to input custom constitutive equations. These features make COMSOL suitable to model EMATs where electromagnetic and elastic effects are coupled together.

For the Lorentz force mechanism a static magnetic model computes the magnetic flux density field $\bar{\mathbf{B}}$ produced by the permanent magnets, while a dynamic electromagnetic model evaluates the eddy current density $\mathbf{J_e}$ induced in the sample by the driving current. These quantities are used to derive the resulting Lorentz force, according to Equation (3.8), which is then used as an input load to the mechanical model that simulates ultrasonic waves. This uncoupled electro-mechanical approach has been used in previous research [10, 19, 42] and has been experimentally validated [59].

The implementation of magnetostriction requires the customization of the constitutive equations of the material (Equations (3.19)). As mentioned in the previous chapter, magnetostriction is both a static and a dynamic effect. The permanent magnet (or electromagnet) of the transducer causes strains on a ferromagnetic sample. However, such strains, being static, do not generate elastic waves. On the other hand, the small dynamic magnetic field produced by the driving current creates small perturbations of the static equilibrium that can induce time-varying mechanical waves. For these reasons, the static effects are not simulated and only the dynamic perturbation effects are analyzed (Equations (3.23)).

There is a significant difference between the Lorentz force transduction mechanism and the magnetostrictive mechanism. It has been shown [9], that in the high conduc-

tivity hypothesis, which is commonly used for metals, the electromagnetic skin depth does not affect the transduction efficiency of the Lorentz force mechanism. This happens essentially because the skin depth varies the eddy current distribution in the sample but not the total induced current. In contrast, the amplitude due to magnetostrictive generation is significantly affected by the electromagnetic skin depth. Since the generated wave amplitude is proportional to the dynamic field this effect implies that the sensitivity of the sensor depends on the phenomena taking place in the skin depth. This has profound implications in the FE simulations of magnetostrictive EMATs: in order to obtain a correct solution of the electro-mechanical equations, both the elastic wavelength λ and the electromagnetic penetration depth δ have to be resolved employing a sufficient number of elements. In most practical cases $\lambda \gg \delta$ holds, requiring the use of a very refined mesh in the regions were magnetostriction transduction occurs. The dimensional mismatch between λ and δ can be extremely serious: for nickel, if $\mu_r = 100$ and the driving frequency is 300 kHz, we have $\lambda/\delta \cong 400$. The implication is that a large number of elements is needed, even for simple models, making the simulations extremely demanding from a computational point of view.

4.3 Numerical solution of the governing equations

For the electromagnetic part of the modelling, the "AC/DC, Magnetic Quasi-Static" application mode was adopted [68]. This code uses the quasi-static approximation (Section 3.2.1) which neglects the term $\partial\mathbf{D}/\partial t$ in Maxwell's equations. This simplification is reasonable for the frequencies of interest in EMATs where the dimensions of the problems are small compared to the electromagnetic wavelength $\lambda_{EM} = c_l/f$, where c_l is the speed of light and f the excitation frequency. The electrodynamic equations (3.1) - (3.6) are solved introducing a scalar potential V and a magnetic vector potential (MVP), $\mathbf{A}$, defined as:

$$\mathbf{E} = -\nabla V - \frac{\partial \mathbf{A}}{\partial t}, \tag{4.1}$$

$$\mathbf{B} = \nabla \times \mathbf{A}. \tag{4.2}$$

After some manipulations [68], Ampére's law (Equation (3.2)) can be reduced to the differential equation:

$$\sigma \frac{\partial \mathbf{A}}{\partial t} + \nabla \times \left(\mu_0^{-1} \nabla \times \mathbf{A} - \mathbf{M}\right) - \sigma \mathbf{v} \times (\nabla \times \mathbf{A}) + \sigma \nabla V = \mathbf{J}^{ext}, \tag{4.3}$$

where $\mathbf{v}$ is the velocity of the conductor and $\mathbf{J}^{ext}$ is the external current density. The divergence of Equation (4.3) yields:

$$-\nabla \cdot \left(\sigma \frac{\partial \mathbf{A}}{\partial t} - \sigma \mathbf{v} \times (\nabla \times \mathbf{A}) + \sigma \nabla V - \mathbf{J}^{ext}\right) = 0. \tag{4.4}$$

Equations (4.3) and (4.4) completely define the electrodynamic problem in terms of the two unknown potentials, V and $\mathbf{A}$ and are numerically solved by the software.

The mechanical part of the model exploits the "Structural Mechanics" module of COMSOL [68]. The elastic problem is solved using the principle of virtual work where the displacement field $\mathbf{u}(x_1, x_2, x_3)$ in the 3D space is the unknown. The principle states that the sum of virtual work from internal stresses equals the virtual work from external loads [68]. If the total stored energy is W, the principle can be expressed as:

$$\delta W = 0. \tag{4.5}$$

This equation can be computed with numerical solvers implemented in the program, yielding the solution of the elastic problem.

When a magnetostrictive domain is modelled, the expression of the total energy W is not that usually found in linear elasticity, as electromagnetic quantities enter in it due to the coupling terms in the constitutive equations (Equations (3.23)). In COMSOL it suffices to implement a multiphysics model, with modified constitutive equations; detailed mathematical formulations of Finite Element magnetostrictive models have been developed in the field of actuators and smart structures and can be found in the literature [69–71].

4.4 3D Finite Element model for magnetostrictive SH waves EMAT

The practical implementation of the FE model described in the previous sections can be better understood through an example EMAT configuration. We consider here a transducer generating Shear Horizontal (SH) waves in ferromagnetic plate-like structures, using a static magnetic field and a single wire carrying the driving current. The static magnetic field runs parallel to the wire (x_2 direction), whereas the dynamic field acts perpendicularly to it, along the x_1 direction. No Lorentz force is produced as the static field and the induced eddy currents are parallel. Since there is only a change in the direction of the total magnetic field, not in its magnitude, shear strains are produced below the wire that generate SH waves (Figure 4.1) [26, 27]. The configuration can be described mathematically by Equations (3.23) with bias field along the x_2 direction:

$$\begin{bmatrix} \widetilde{\epsilon}_1 \\ \widetilde{\epsilon}_2 \\ \widetilde{\epsilon}_3 \\ \widetilde{\epsilon}_4 \\ \widetilde{\epsilon}_5 \\ \widetilde{\epsilon}_6 \end{bmatrix} = \begin{bmatrix} s_{11} & s_{12} & s_{12} & 0 & 0 & 0 \\ s_{12} & s_{11} & s_{12} & 0 & 0 & 0 \\ s_{12} & s_{12} & s_{11} & 0 & 0 & 0 \\ 0 & 0 & 0 & s_{44} & 0 & 0 \\ 0 & 0 & 0 & 0 & s_{44} & 0 \\ 0 & 0 & 0 & 0 & 0 & s_{44} \end{bmatrix} \begin{bmatrix} \widetilde{\sigma}_1 \\ \widetilde{\sigma}_2 \\ \widetilde{\sigma}_3 \\ \widetilde{\sigma}_4 \\ \widetilde{\sigma}_5 \\ \widetilde{\sigma}_6 \end{bmatrix} + \begin{bmatrix} 0 & -\frac{d_{22}}{2} & 0 \\ 0 & d_{22} & 0 \\ 0 & -\frac{d_{22}}{2} & 0 \\ 0 & 0 & d_{61} \\ 0 & 0 & 0 \\ d_{61} & 0 & 0 \end{bmatrix} \begin{bmatrix} \widetilde{H}_1 \\ \widetilde{H}_2 \\ \widetilde{H}_3 \end{bmatrix} \quad (4.6)$$

$$\begin{bmatrix} \widetilde{B}_1 \\ \widetilde{B}_2 \\ \widetilde{B}_3 \end{bmatrix} = \begin{bmatrix} 0 & 0 & 0 & 0 & 0 & d_{61} \\ -\frac{d_{22}}{2} & d_{22} & -\frac{d_{22}}{2} & 0 & 0 & 0 \\ 0 & 0 & 0 & d_{61} & 0 & 0 \end{bmatrix} \begin{bmatrix} \widetilde{\sigma}_1 \\ \widetilde{\sigma}_2 \\ \widetilde{\sigma}_3 \\ \widetilde{\sigma}_4 \\ \widetilde{\sigma}_5 \\ \widetilde{\sigma}_6 \end{bmatrix} + \begin{bmatrix} \mu_{11} & 0 & 0 \\ 0 & \mu_{11} & 0 \\ 0 & 0 & \mu_{33} \end{bmatrix} \begin{bmatrix} \widetilde{H}_1 \\ \widetilde{H}_2 \\ \widetilde{H}_3 \end{bmatrix} \quad (4.7)$$

where d_{22} and d_{61} are defined by equations (3.25)-(3.26) and an elastic isotropic medium has been assumed, thus $s_{44} = 2(s_{11} - s_{12})$. In principle, the theory outlined

in Chapter 3 might be applied to more general anisotropic media, however, throughout this thesis it will be assumed that the media under investigation are elastically isotropic.

Because of the spatial position of the wire (along the x_2 axis), $\widetilde{H}_1$ is the largest dynamic component and the main contribution to SH waves comes from the term $\widetilde{\epsilon}_6 \propto d_{61}\widetilde{H}_1$. It can be shown [27] that SH waves are generated and detected only by a subset of equations (4.6)-(4.7), i.e.:

$$\begin{cases} \widetilde{\epsilon}_6 &= s_{66}\,\widetilde{\sigma}_6 + d_{61}\,\widetilde{H}_1 \\ \widetilde{B}_1 &= d_{61}\,\widetilde{\sigma}_6 + \mu_{11}\,\widetilde{H}_1 \end{cases}, \tag{4.8}$$

where the second equation of the system accounts for the inverse magnetostrictive effect that allows the transducer to detect elastic waves. Equations (4.8) show that this EMAT configuration relies only on the magnetostriction coefficient d_{61}, while d_{22} does not contribute to the generation and detection of SH waves. As a consequence, the performance of this transducer strongly depends on d_{61}, but also on other physical properties, namely the magnetic permeability, as will be shown in Section 5.6.1.

The EMAT described has been modelled in COMSOL (Figure 4.2). It was simulated the operation on a 240 mm diameter, 0.5 mm thick nickel disk. A straight wire lies above the disk ($x_3 < 0$ semi-space), 0.1 mm away from it, and carries a 1 A current oscillating at 100 kHz. As mentioned, the solution of this problem is computationally extremely demanding, so special care is needed when designing the model. Only the inner part of the disk, just below the wire, employs the full magnetostrictive equations (Equation (3.23)), since the dynamic magnetic field $\widetilde{H}_1$ has a significant amplitude only in a limited region of the plate, due to the skin depth effect. The induced eddy currents are concentrated near the surface of the conductor and decay in an exponential fashion, regulated by the skin depth parameter δ [12]. Figure 4.3 shows the dynamic magnetic field induced in the nickel plate by the driving current, as computed with a FE electrodynamic simulation. The intensity of the dynamic field $\widetilde{H}_1$ exponentially decreases with depth (x_3 direction) and, with a lower rate,

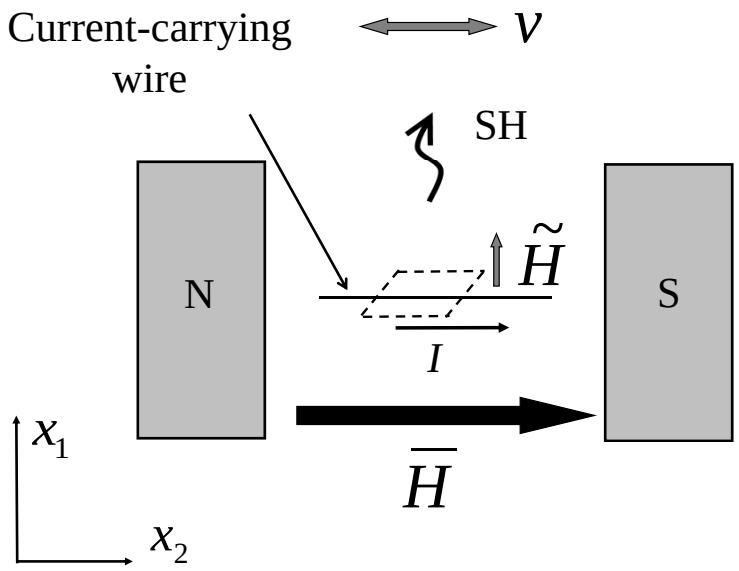

Figure 4.1: *Schematic diagram of a SH magnetostrictive EMAT on a plate lying in the $\{x_1, x_2\}$ plane. The static and the dynamic magnetic fields are indicated. The shear deformation of the material below the wire is highlighted. Shear horizontal waves propagate in the x_1 direction, causing a particle motion v in the x_2 direction.*

with the lateral distance (x_1) from the wire. For this reason, the full constitutive Equations (3.23) are employed only in the limited region where magnetostriction is significant, while in the rest of the plate the usual linear elastic constitutive equations are used. The outer part of the disk uses a purely elastic constitutive equation, as the effect of the dynamic current is negligible in this region, and only the wave propagation has to be computed. The boundary between the magnetostrictive and the elastic region was defined such that in the magnetostrictive volume the dynamic field is at least 1 % of the its maximum value: $\widetilde{H}_1(x_1, x_2, x_3) \geq 0.01\, \widetilde{H}_1^{max}$. This approximation does not affect the accuracy of the simulation but saves significant computation time. Finally, a circular absorbing region, with non-zero damping constant, surrounds the disk. This avoids back-reflections from the edge of the disk, thus enabling the simulation of an infinite plate. This region has the same elastic properties as the original medium, but has dissipative properties due to damping. The so-called proportional or Rayleigh damping [68] is used:

$$C = \alpha M + \beta K, \tag{4.9}$$

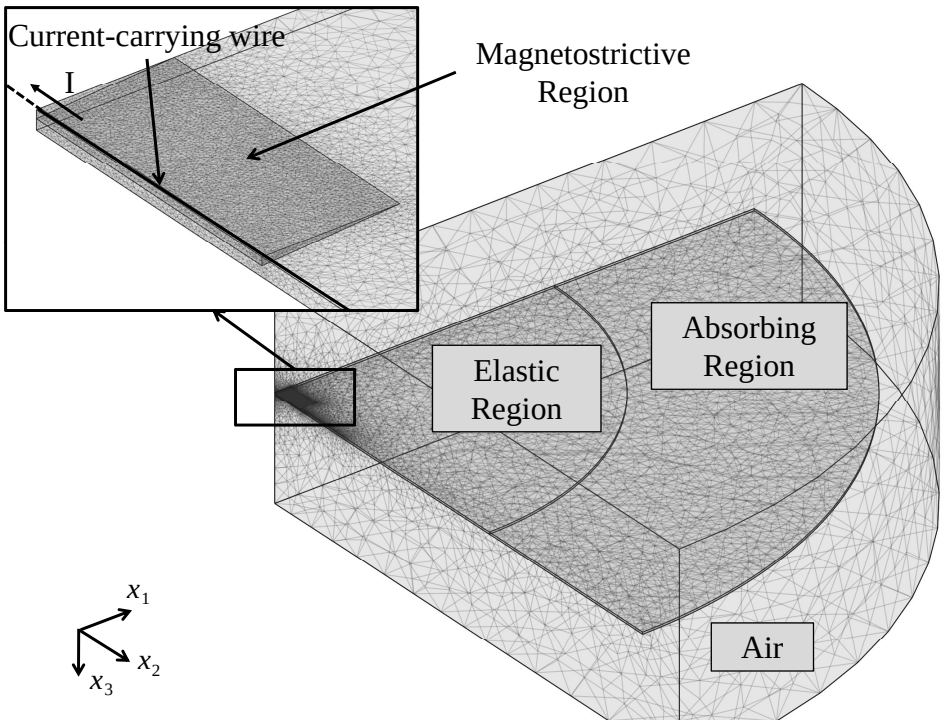

Figure 4.2: *Finite Element model of SH wave magnetostrictive EMAT configuration. The transducer is made of a current-carrying wire producing a dynamic magnetic field and permanent magnets (not shown) to provide a bias field. The disk is divided into a magnetostrictive region, where transduction occurs, an elastic region where SH waves propagate and and absorbing region to avoid back reflections from the edges of the model. The domains use different mesh refinements to correctly resolve the electromagnetic skin depth or the elastic wavelength. Only a quarter of the full geometry is modelled due to the symmetry planes* $\{x_1, x_3\}$ *and* $\{x_2, x_3\}$*. In the equivalent full model, the wire completely lies above the plate (dashed line in the inset) and carries a current with amplitude* $I = 1\,\mathrm{A}$*.*

where C is the damping matrix, M is the mass matrix, and K is the stiffness matrix; α and β are the damping factors. The damping matrix appears in the governing differential equation as a matrix coefficient multiplying the velocity, thus introducing a dissipative term In this case, β was set to zero, whereas α was a cubic function of the distance from the inner radius r_i of the absorbing region: $\alpha \propto (r - r_i)^3$, where $r = \sqrt{x_1^2 + x_2^2}$ is the radial distance from the centre of the wire.

The whole model employs a mesh of quadratic tetrahedral elements. Different mesh refinements are employed for the magnetostrictive region, where the transduction takes place and δ has to be resolved, and the elastic region, where simple elastic

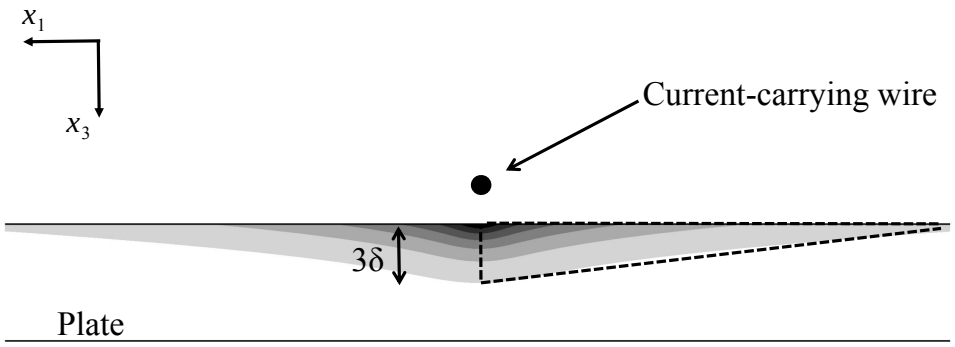

Figure 4.3: *FE simulation showing the magnitude of the tangential component of dynamic magnetic field, $\widetilde{H}_1$, induced in a nickel plate by the driving current carried by an infinite (in the x_2 direction) wire. The field exponentially decreases both with depth (x_3 direction) and lateral distance (x_1) from the wire. δ denotes the electromagnetic skin depth. By only using the full model in the dashed triangle, the computational weight of the model is drastically reduced.*

propagation occurs and the wavelength λ has to be resolved (Figure 4.2). In all the EMAT models presented in this thesis it was chosen to employ around 15 elements per wavelength, which complies with criteria established in previous research [72], dictating at least 7 elements per wavelength. As for the electromagnetic skin depth, a convergence study was carried out. The FE predicted magnetic field due to an infinite current-carrying wire above a half-space was compared to an analytical solution [73]. The discrepancy between the numerical and the exact solution is plotted as a function of the number of elements per skin depth in Figure 4.4. In order to achieve errors lower than 1%, it was chosen to use three elements per skin depth in all the EMAT models presented in this work. To avoid abrupt changes in the mesh density of the different regions, an "element growth rate" [68] is set to 1.2, i.e. the size of the elements can grow by no more than 20% from one element to another at the boundary between two regions.

Two planes of symmetry are present, i.e. the $\{x_1, x_3\}$ and the $\{x_2, x_3\}$ planes pass-

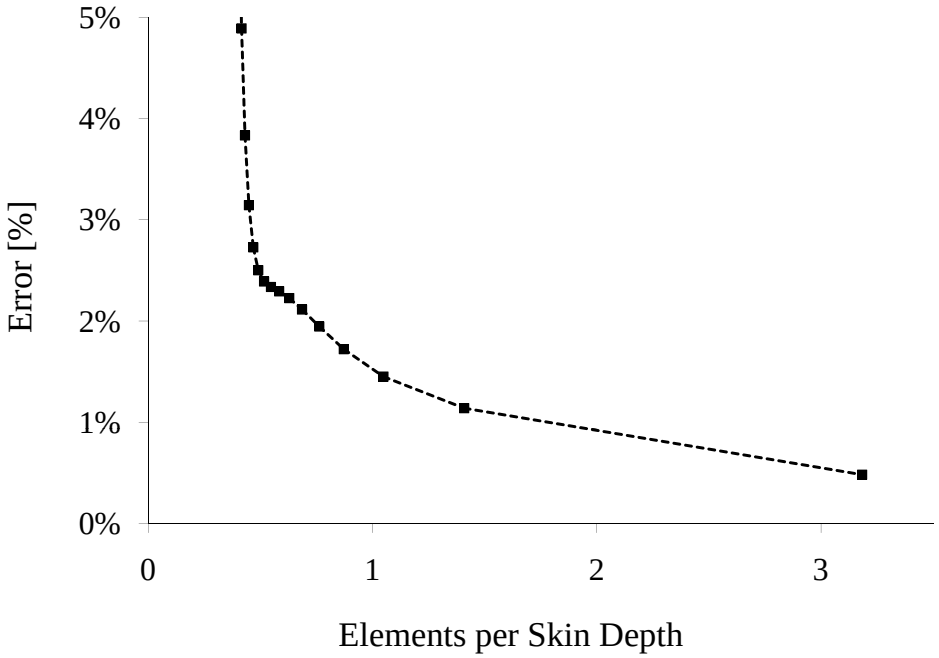

Figure 4.4: *Percentage error between FE simulation and the corresponding exact solution as a function of the number of elements per skin depth. The magnetic field caused by an infinite wire carrying a time-varying current above a conductive half-space was computed with Comsol Multiphysics and with closed-form equations [73].*

ing through the origin of axes (Figure 4.2). Thus, by defining appropriate boundary conditions the model can be reduced to a quarter of the full model. In the electrodynamic model, in the $\{x_1, x_3\}$ plane the boundary condition $\mathbf{n} \times \mathbf{A} = 0$ is prescribed, i.e. null tangential component of the magnetic vector potential, and consequently the magnetic field $\widetilde{\mathbf{H}}$ is tangential to the considered plane of symmetry. The other symmetry condition applied to the $\{x_2, x_3\}$ plane is $\mathbf{n} \times \widetilde{\mathbf{H}} = 0$, which implies a zero normal component of the electric current. For the mechanical part of the model, the $\{x_1, x_3\}$ and the $\{x_2, x_3\}$ planes are prescribed the "y-z" and "x-z symmetry plane" conditions respectively. With these boundary conditions, and by applying an equivalent driving current, that is $I^{reduced} = I^{full}/2$, the problem has to be solved only in the volume $\{x_1 \geq 0, x_2 \geq 0, x_3\}$, thus reducing the number of degrees of freedom to about a quarter of the full model. Figure 4.5 shows the results of FE simulations of a full model (solid line) against a model employing the two planes of symmetry (circles) for the same magnetostrictive SH EMAT. A polar plot of the displacement

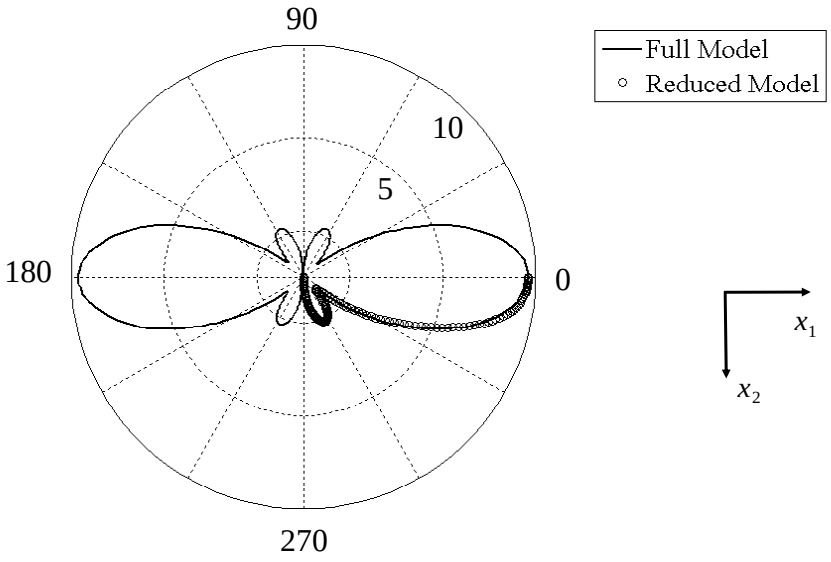

Figure 4.5: *Polar plot of the displacement component along the x_2 direction, v, at a distance $r = 50\,\mathrm{mm}$ produced by a magnetostrictive SH wave EMAT in a plate. The displacement is expressed in arbitrary units per unit current. The reference system is the same used in Figures 4.1 and 4.2 The FE simulation of a full model (solid line) is compared to a model employing the two planes of symmetry (circles) for the same magnetostrictive SH EMAT.*

component along the x_2 direction, v, produced by the same SH wave EMAT in a plate is shown.

4.5 Simplified models: analytical-numerical approach

A useful strategy to reduce drastically the computational requirements of magnetostrictive models relies on the use of a hybrid analytical-numerical approach. This kind of simplification can only be used when analytical solutions to part of the problem, either the electrodynamic or the elastic one, are available in closed form. It is seldom possible to find such analytical expressions, however, whenever they are available they can be employed to reduce the memory requirements and the compu-

tational time greatly. A typical example is the case of those EMAT configurations whose coil is made of several long straight sections, like meander or race-track coils (Section 2.4). In these cases, the dynamic magnetic field induced in a ferromagnetic material can be approximated with the analytical expression found by Chari and Reece for an infinitely long wire above a half-space [73]. It is possible to exploit these equations, for example in the modelling of the SH wave EMAT described in the previous section, such that the first constitutive equation of (4.8) becomes:

$$\widetilde{\epsilon}_6 \;=\; s_{66}\,\widetilde{\sigma}_6 + d_{61}\,\widetilde{H}_1^{\star}, \tag{4.10}$$

where $\widetilde{H}_1^{\star}$ is not an unknown quantity to be computed numerically, but is given by a known closed form expression. Since the electrodynamic problem is solved via analytical means, the electromagnetic potentials $\mathbf{A}$ and V do not have to be computed and each node of the mesh requires four degrees of freedom less than those of the original model, that is, only a simple elastic model has to be solved. This significantly reduces the computational time, as this is roughly a function of the square of the total number of degrees of freedom for harmonic simulations. The use of analytical solutions introduces the pros and the cons of such methods. Only special geometries can be addressed, effects such as the finiteness of the wires (edge effects) or their conductivity are neglected and mutual coupling between the generation and reception process is assumed to be insignificant. On the other hand, an appropriate choice of the simplifying model can lead to satisfactory approximate solutions with considerably smaller computational requirements. Figure 4.6 shows the results obtained for the same model of SH magnetostrictive EMAT described in the previous section. The magnitude of the displacement v is plotted along the x_1 axis for a multiphysics model together with a model using an analytic solution for the dynamic magnetic field. While the discrepancy between the two simulations is limited to 5-10%, the model employing the analytic expression for $\widetilde{H}_1$ is significantly faster and less demanding than the multiphysics model.

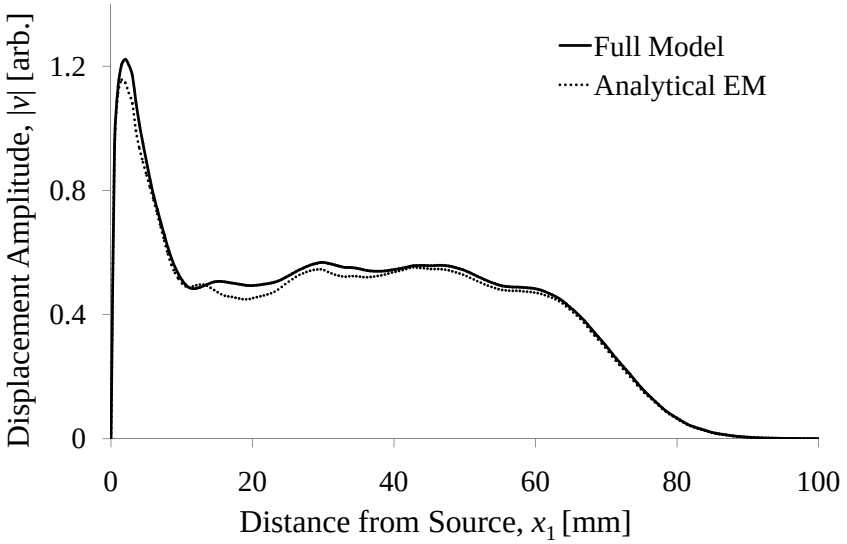

Figure 4.6: *Magnitude of the particle displacement v plotted along the x_1 axis (for $x_2 = x_3 = 0$) for a SH magnetostrictive EMAT as the one shown in Figure 4.2. The results from a full multiphysics model (continuous line) are shown together with those from a model using an analytic solution for the dynamic magnetic field (dashed line).*

4.6 2D axisymmetric model

For some EMAT configurations, for example the pancake coil shear wave EMAT, the three dimensional problem can be approximated with a simplified two-dimensional axisymmetric model, in cylindrical coordinates $\{r, z, \phi\}$. If the driving current flows in the azimuthal direction, i.e. perpendicular to the modelled plane $\{r, z\}$, the magnetic vector potential has only one nonzero component $A_\phi(r, z)$ and the electrodynamic problem reduces to finding the solution of a single scalar PDE, which is computationally simple. The mechanical part of the model can also be simplified by using COMSOL's "Stress-Strain, Axial Symmetry" application mode [68]. A cylindrical coordinate system is employed and the elastic equations are solved for the displacements in the radial and axial directions. The assumption is that the circumferential component of displacement is zero, as well as the stress and strain components $\sigma_{r\phi}$, $\sigma_{z\phi}$, $\epsilon_{r\phi}$, $\epsilon_{z\phi}$, and that the loads act on the $\{r, z\}$ plane only.

Finally, assuming that the material is magnetized along the z direction, magnetostriction constitutive equations reduce to:

$$\begin{cases} \widetilde{\epsilon}_r = s_{11}\,\widetilde{\sigma}_r + s_{13}\,\widetilde{\sigma}_z + d_{31}\,\widetilde{H}_z \\ \widetilde{\epsilon}_z = s_{13}\,\widetilde{\sigma}_r + s_{33}\,\widetilde{\sigma}_z + d_{33}\,\widetilde{H}_z \\ \widetilde{\epsilon}_{rz} = 2\,s_{44}\,\widetilde{\sigma}_{rz} + d_{15}\,\widetilde{H}_r \end{cases} \tag{4.11}$$

and,

$$\begin{cases} \widetilde{B}_r = 2\,d_{15}\,\widetilde{\epsilon}_{rz} + \mu_{11}\widetilde{H}_r \\ \widetilde{B}_z = d_{31}\,\widetilde{\epsilon}_r + d_{33}\,\widetilde{\epsilon}_z + \mu_{33}\widetilde{H}_z \end{cases} . \tag{4.12}$$

4.7 Conclusions

A description of the numerical methods used to simulate EMAT operation has been given. A SH wave magnetostrictive EMAT configuration has been taken as an example to illustrate how to effectively choose the size of the domains and of the mesh grid. The use of symmetries and analytical solutions to reduce the computational demands of the model has also been discussed. Several researchers have already proposed EMAT Finite Element models [7, 40–45, 56–59], even including magnetostriction; however, the critical question is how well the predictions of the model correlate with real-world data. The experimental validation of the present FE model will be the topic of the next chapter.

Chapter 5

Validation of the model

5.1 Introduction

This chapter investigates the validity of the FE model presented in Chapter 4 by comparing its predictions with experimental tests. This is a multi-step process that starts with the assessment of the performance of the single COMSOL modules against analytical benchmarks. Then a full multiphysics model is validated: a 3D magnetostrictive EMAT on a nickel plate is used as a case study. First a qualitative validation is given, showing how the model is able to successfully compute the wave amplitude dependence on significant parameters: the static bias field, the driving current amplitude and the excitation frequency. A quantitative validation follows, where the wave amplitude per unit current is predicted without the use of any arbitrary adjustable parameter and is compared to experimental tests.

5.2 Model benchmark

Prior to validation of the full multiphysics model, the single modules have to be benchmarked against known analytical solutions to assure the reliability of the software. Sections 5.2.1-5.2.3 are simply a verification of Comsol's performance in known

applications. First, the electromagnetic module is addressed: both the induction of eddy currents in a metal sample due to a time-varying current and the magnetic field caused by a permanent magnet are numerically modelled and compared with their analytical counter-parts. Then a simple mechanical model for ultrasonic waves is validated against an analytical model.

5.2.1 Eddy current

As a benchmark for the generation of eddy currents in a metallic sample, the classical Dodd and Deeds [35] model for a circular coil above a conductive medium was used. This model assumes an axisymmetric geometry, expressed in cylindrical coordinates $\{r, z, \phi\}$. The circular coil is modeled as a thin current sheet parallel to the surface of the sample, and placed at a distance h from it, the lift-off. The current is sinusoidally-varying and has only a circumferential component J_ϕ; thus, the problem can be solved by means of a single differential equation with the circumferential component of the magnetic vector potential $A_\phi(r, z)$ as the unknown variable. The induced eddy current in the sample is then computed simply as: $J_e = -j\omega\sigma A_\phi$, where ω is the angular frequency and σ the conductivity of the sample. A solution of the problem using Dodd's and Deed's formula can be found in [37] for a case with the following geometrical parameters and material properties: a 3 mm inner radius, 17 mm outer radius coil with lift-off 0.6 mm is driven by a sinusoidal current of amplitude 1 A and frequency 1 MHz, acting on an infinite aluminum half-space with conductivity 36.5 MS/m, and relative permeability unity. A numerical model was implemented in COMSOL to be compared to the theoretical model. The electromagnetic module of the program was used (AC/DC module), with axial symmetry. The chosen application mode was the "Azimuthal Induction Currents, Vector Potential", with time-harmonic analysis. This code solves numerically the same differential equation solved analytically by Dodd and Deeds. The same parameters of the analytical model were used, the only difference lying in the fact that the coil in the FE model has a finite thickness. This parameter was set to a very small value (0.01 mm) and the current density was adjusted so that the

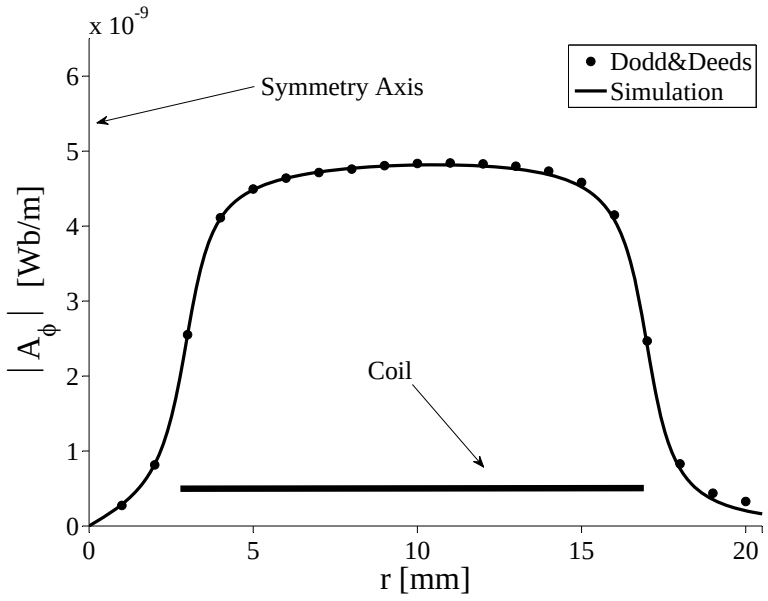

Figure 5.1: *Radial distribution of magnetic vector potential on the surface of an aluminum sample. Analytical solution (dots) compared with the numerical one (continuous line). The position of the cross-section of the coil is highlighted; for symmetry reasons only half of the distribution is shown (for positive values of r).*

total current would be the same as that of theoretical model, that is, 1 A. The conductivity inside the coil cross-section was fictitiously set to zero, in order to reproduce the homogeneous current sheet assumed in the theoretical model. The boundary conditions employed were the continuity of the tangential component of the magnetic field across different regions ($\mathbf{n} \times (\mathbf{H}_1 - \mathbf{H}_2) = 0$, where $\mathbf{n}$ is the unit vector normal to the surface separating domain 1 from domain 2) and the magnetic insulation condition ($A_\phi = 0$) for the other boundaries, representing the asymptotic behavior at infinity. The model employed 100,000 triangular elements (quadratic Lagrange elements) and was solved by means of an iterative algorithm (GMRES) in a few minutes on a desktop PC. The result of the computation is shown in Figure 5.1 together with the analytical solution. The radial distribution of the modulus of the magnetic vector potential generated on the metal surface ($z = 0$) is shown. The agreement between the two models is excellent.

5.2.2 Static magnetic field

Analytical relationships predicting the static magnetic field due to a magnet are available only for simple geometries and along particular directions. For instance, the magnetic flux density along the axis of a cylindrical, rare earth (Neodymium-Iron-Boron or Samarium-Cobalt) magnet, at distance z from its pole can be found in the catalogs of the manufacturers [74]:

$$B_z = \frac{B_r}{2}\left(\frac{L+z}{\sqrt{R^2+(L+z)^2}} - \frac{z}{\sqrt{R^2+z^2}}\right), \tag{5.1}$$

where L and R are the length and the radius of the magnet, while B_r is its remanence. For comparison, a Finite Element model was developed. This serves only as a verification of Comsol's performance as Equation (5.1) does not hold when a ferromagnetic material is nearby the magnet. The model exploits axisymmetry; the application mode is again the "Azimuthal Induction Currents", solving for the magnetic vector potential and using a static analysis, as no time-varying phenomena are involved. Within the magnet the constitutive relation used is:

$$\mathbf{B} = \mu_0\mu_r\mathbf{H} + \mathbf{B}_r. \tag{5.2}$$

This assumes a linear demagnetization curve (second quadrant of the B-H curve) defined by two parameters: the remanence, that is, the magnetic flux density when the magnetic field is null ($B_r = B_{H=0}$), and the permeability μ_r which determines the slope of the line. The magnet is surrounded by air and continuity relations are assumed at the boundaries. In both the numerical and analytical model, a NdFeB magnet was employed, magnetized along the z axis with remanence $B_r = 1.23\,\mathrm{T}$ and unit relative permeability. The magnet has a 36 mm diameter ($2R$) and is 6 mm thick (L). A comparison of the result of the analytical formula (5.1) with the analogous FE simulation is given in figure 5.2; the matching is extremely accurate.

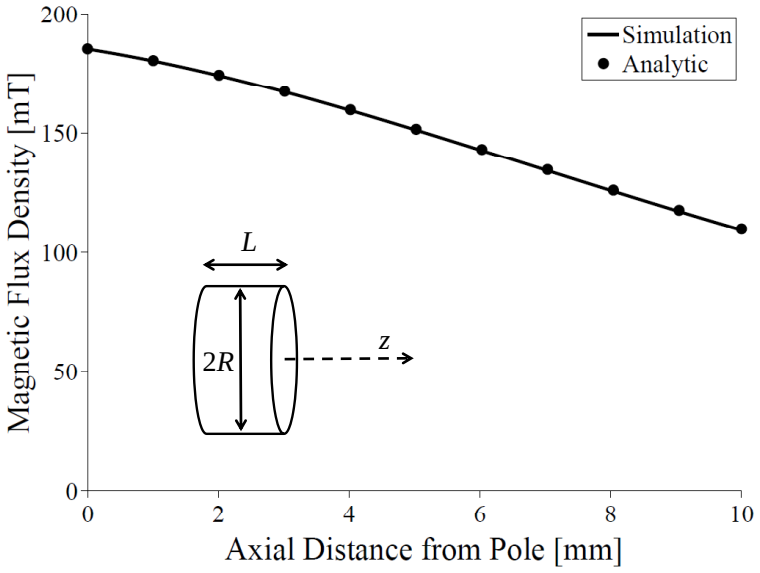

Figure 5.2: *Magnetic flux density produced by a NdFeB cylindrical magnet, $2R$ diameter and L thick. Comparison FE vs. analytic model along the magnet axis, z direction, starting from the surface of a pole. The magnet is surrounded by air.*

5.2.3 Ultrasonic field

To benchmark the mechanical module of COMSOL, a classical model relevant to NDT, the so-called piston-source model was used. The model represents an elastic half-space with a uniform harmonic stress applied over a circular area on its surface, in the direction normal to it, as shown in Figure 5.3. This model is popular in Non-Destructive testing since it can be employed to describe the ultrasonic field caused by a cylindrical piezoelectric transducer applying a normal force on a sample. Miller and Pursey [36] found the analytical solution to this axisymmetric problem. The numerical counter-part of this model was implemented in COMSOL. The "Structural Mechanics" module was adopted with the "Axial Symmetry, Stress-Strain" application mode. This application solves the Navier equation for an isotropic elastic medium (Equation (3.10)) in cylindrical coordinates $\{r, z, \phi\}$, assuming that the displacement in the circumferential direction (ϕ direction) is zero and that loads are only in r and z directions and are independent of ϕ. The surface force is applied on a circular area of radius 10 mm, its amplitude is 1 Pa and varies sinusoidally at 1 MHz.

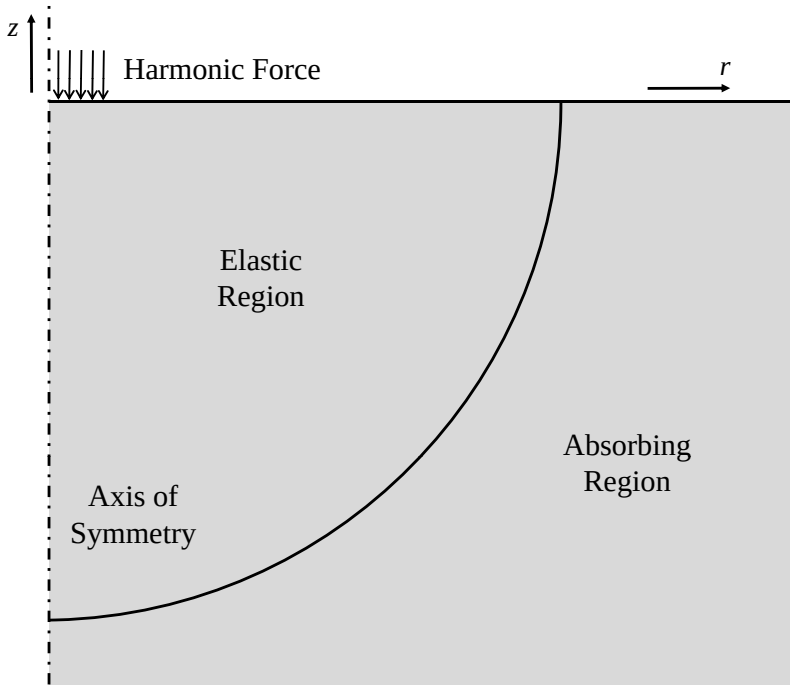

Figure 5.3: *Geometry of the piston-source model on a half-space implemented in COMSOL. The applied uniform force is also shown.*

This force acts on an aluminum sample: Young's modulus 69 GPa, Poisson's ratio 0.33, density 2700 $\mathrm{Kg/m^3}$. The analytical model assumes a semi-infinite medium, which cannot be implemented directly in the numerical model. In order to overcome this issue, an absorbing region surrounding the elastic region is added to the model. The results of the computation are shown in Figure 5.4. The amplitudes of both the radial and the axial displacement are plotted against the angle from the symmetry axis, on a hemisphere of 70 mm radius. An analytical solution of the same problem was found by Kawashima [10] and the resulting displacements are also plotted in Figure 5.4. The comparison of the two solutions, numerical and analytical, yields satisfactory match.

5.3 Multiphysics model validation

Having satisfactorily tested each COMSOL module to be employed in the full EMAT model, the overall performance of a complete model is to be assessed. As mentioned,

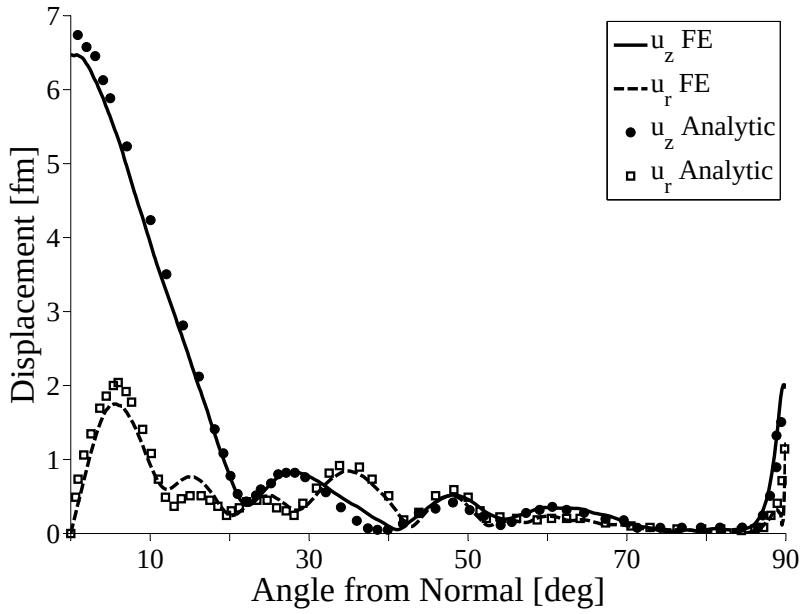

Figure 5.4: *Piston source model. Normal and radial displacements, u_z and u_r, as a function of the angle from the symmetry axis, at a distance $|r| = 70\,\mathrm{mm}$ away from the source; as simulated in COMSOL (—— and – –, respectively) and from analytical calculations (● and □) from [10].*

EMATs exploit both the Lorentz force mechanism and magnetostriction to generate and detect ultrasonic waves.

A large number of studies on the Lorentz force mechanism has been published; comprehensive monographs on EMATs by Thompson [6] and Hirao and Ogi [7] summarize the state of the art on this research topic. The phenomenon has been investigated with numerical models [40–45, 56–58] and validated against experimental data [59]. On the other hand, the status of the understanding of magnetostriction is less satisfactory due to its complex behaviour: non-linear, hysteretic coupled equations, together with a number of experimental difficulties make its study challenging. It is important to recall that the analysis of magnetostriction is paramount as this transduction mechanism is the dominant one in some EMAT configurations operating on ferromagnetic metals (Section 2.4) and it has been claimed by some authors [21] to be the dominant transduction mechanism in general.

Finite Element magnetostrictive models have been developed for actuators and smart structures to simulate the operation of giant magnetostrictive materials like Terfenol-D [69–71]. There have been many Finite Element models for Lorentz force EMATs, but few have included magnetostriction. Ludwig *et al.* [40–45] developed an EMAT finite element model inclusive of magnetostriction, however it was not validated against experiments, and the physical parameters inputted to the model were just estimated, not measured.

For these reasons, the validation of the model will focus on a magnetostrictive EMAT, that had not been studied via the Finite Element Method before. To simplify the validation process, the chosen EMAT configuration does not exploit the Lorentz force mechanism at all, so the generation of ultrasonic waves can be entirely attributed to magnetostriction. In Chapter 6 the operation of a Lorentz force EMAT will be simulated and experimental data will validate the predictions for Lorentz force-type EMATs.

5.4 Magnetostrictive Shear Horizontal wave EMAT

The EMAT configuration described in Section 4.4 was employed to validate the FE model. This transducer produces Shear Horizontal (SH) waves in ferromagnetic plates, due to magnetostrictive effects only as the current-carrying wire and the static bias field are parallel to each other (Figure 4.1). The operation of this type of EMAT is described mathematically by Equation (4.8).

The operation on a 0.5 mm thick nickel disk was simulated, as shown in Figure 5.5. The straight wire carries a 1 A current oscillating at frequencies between 100 kHz and 300 kHz. The wire is placed above the disk, 0.1 mm away from it. The plate has the material properties of nickel: Young's modulus 200 GPa, Poisson's ratio 0.29, mass density 8900 kg/m^3, electrical conductivity 14.3 MS/m. The full magnetostrictive equations (Equations (4.6)-(4.7)) are used only in the inner part of the disk, near the wire, while the outer part of the disk uses a purely elastic constitutive equation. The surrounding annular area is an absorbing region to avoid back reflections from

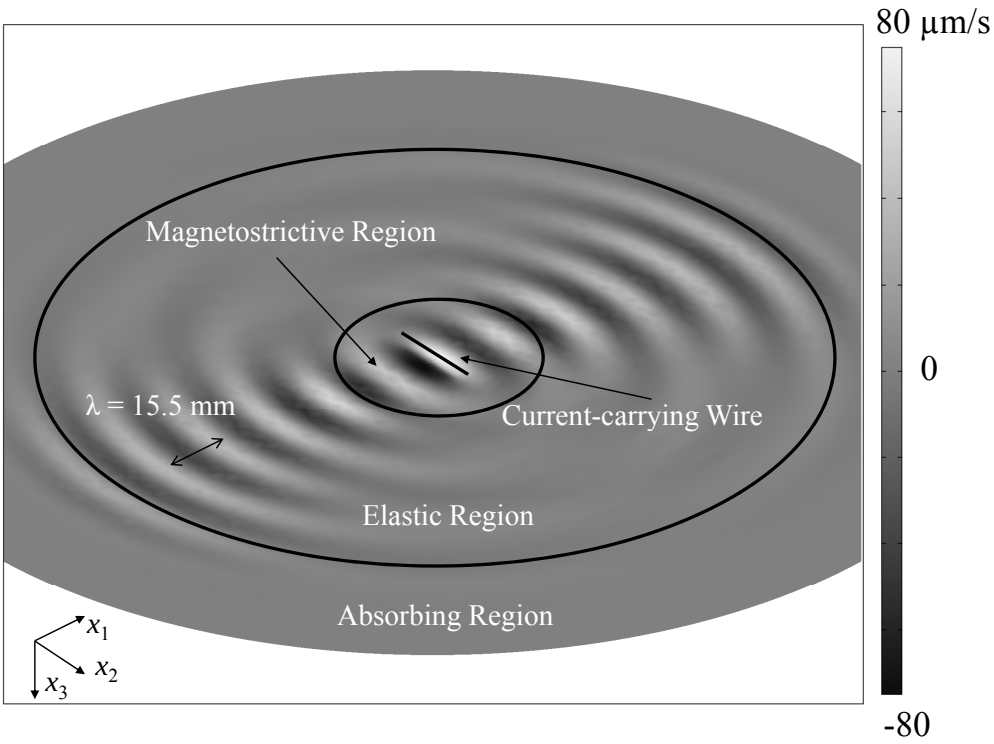

Figure 5.5: *Finite Element simulation of a magnetostrictive EMAT generating SH waves on a nickel disk. The particle velocity along the x_2 axis is displayed* [µm/s]. *Planes of symmetry were employed to reduce the size of the model; for clarity the figure shows a zoom on the central region of a complete model.*

the edge of the disk, thus enabling the simulation of an infinite plate. The model employs a mesh of quadratic tetrahedral elements and two planes of symmetry, as described in Section 4.4.

The model is solved for the coupled electrodynamic equations and linear elastic equations, at the excitation frequency. The result is shown in Figure 5.5 where the particle velocity along the x_2 direction is plotted. The model has successfully computed the generation of SH0 waves propagating along the x_1 direction. Thus the simulation can predict a mechanical effect caused by electromagnetic inputs: the static bias field and the dynamic currents.

5.5 Magnetostriction measurement

The magnetostriction curve, i.e. magnetostrictive strain against static magnetic field strength, has to be measured in order to determine the magnetostriction parameters (Equations (3.25)-(3.26)) to be fed in the numerical model. This is a non-trivial task for several reasons: the strains to be measured are small in many metals (less than 8-10 ppm in common carbon steels), and of the order of magnitude of those due to thermal expansion for a 1°C temperature change. Another issue is the determination of the magnetic field H within the metal, as we can only measure the value of the magnetic flux density B, outside the sample. These problems can be overcome by careful design of the experiment. However, what cannot be avoided is the intrinsic variability of magnetic properties. Magnetostriction is extremely sensitive to a number of external parameters such as the residual stress in the material, the texture and previous history of magneto-mechanical loads [11, 75]. This difficulty is exemplified in Figure 5.6 where five magnetostriction curves for pure nickel, measured by different researchers [11, 12, 33, 64, 76], are reported. Even if the sample is a pure metal, there are significant discrepancies, especially in the low-field region (this is partly due to hysteresis, but this phenomenon alone cannot account for the observed differences). In order to obtain unambiguous data for the numerical model, the magnetostriction curve of the nickel sample to be used for the subsequent validation of the model was measured. The sample, a 0.5 mm thick, 99.0% pure nickel plate, was annealed at 700°C for thirty minutes to minimize the above mentioned experimental variabilities. Since the Curie temperature of pure nickel is 354°C, the process completely demagnetized the sample, bringing it back to its virgin magnetic status. Furthermore, residual stresses and texture were removed within the experimental error and the intrinsic material variations, as Barkhausen noise measurements performed by the staff of Prof P. Nagy at University of Cincinnati demonstrated. To measure the magnetostriction curve, the sample was placed in the air gap of a magnetic circuit. Two electromagnets driven by an adjustable dc current generated the bias field, the resulting magnetic field being proportional to the driving current. The magnetic flux density generated at the surface of the

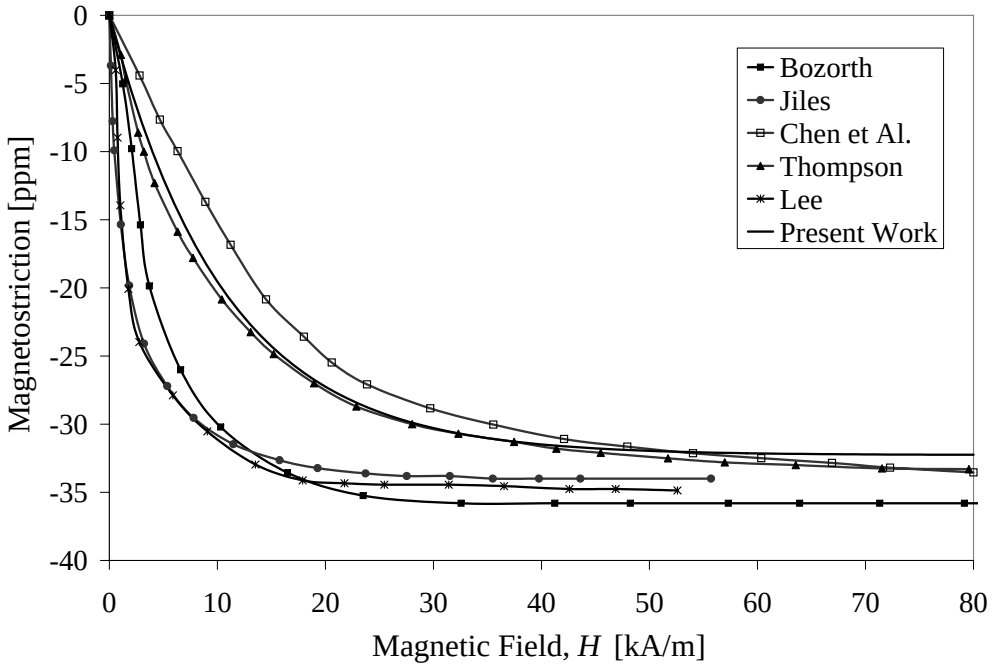

Figure 5.6: *Magnetostriction curves of pure nickel, as measured by Bozorth [11], Jiles [12], Chen et al. [76], Thompson [33], Lee [64], and the author of the present work (*0.4 ppm *standard deviation).*

sample, in a direction parallel to the surface (B^{air}) was measured by using a Hall gaussmeter (GM04, Hirst Magnetic Instruments). The magnetic field strength inside the material can then be estimated by acknowledging that $H^{air} = B^{air}/\mu_0$ and that the boundary conditions for **H** prescribe the continuity of the tangential component at the boundary between two media, so $H^{sample} \cong H^{air}$. Four strain gauges (Kyowa) in a full bridge configuration were employed. Two gauges on the opposite arms of the Wheatstone bridge were parallel to the static bias field, while the other two gauges were perpendicular to it; this configuration maximizes the sensitivity to the strain in the bias field direction while cancelling out any bending strain or thermal expansion strain. The final result is also shown in Figure 5.6, in excellent agreement with one of the curves found in the literature.

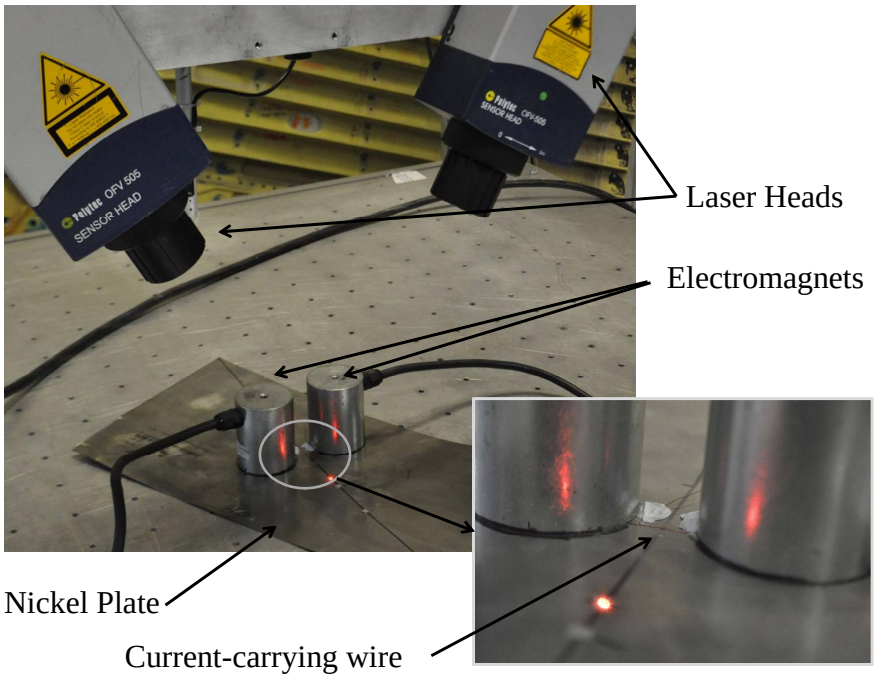

Figure 5.7: *Experimental set-up for model validation. A simple magnetostrictive EMAT is made of a straight current-carrying wire and two electromagnets. The transducer generates SH waves in a nickel plate whose particle velocity is detected by laser vibrometers.*

5.6 Validation

The model was compared against a simple experiment. The validation focused on the magnetostrictive generation mechanism as a function of different relevant quantities: the static bias field $\bar{H}$, the dynamic magnetic field $\widetilde{H}$ and the excitation frequency, f.

A magnetostrictive SH wave transducer, like the one described in the Section 4.4, was used to generate waves in a nickel plate and the in-plane particle velocity 65 mm from the transducer was detected by a laser Doppler vibrometer (two Polytec OFV 505 heads, with OFV 5000 controllers, oriented at $\pm 30°$ from the normal of the plate). The driving signal through the wire was a five-cycle toneburst, 4 A peak to peak current, centred at the target frequency. The same geometry and parameters used in the FE model were reproduced in the test. Figure 5.7 shows a picture of the experimental set-up used.

5.6.1 Qualitative validation

Bias field dependence

First the experiment was performed varying the static bias field, $\bar{H}_2$; this is a significant test, since the shear strain, and thus the signal amplitude, is commonly supposed to be proportional to d_{61}, which is a function of the static field (Equation (4.8)). The control of the bias field was achieved by changing the driving current of the electromagnets producing the field. It has been verified that the resulting static magnetic field is directly proportional to the current fed to the electromagnets. The magnetic flux density along the x_2 direction ($\bar{B}_2^{Air}$) was measured with a Hall gaussmeter. The magnetic field in air was then computed as $\bar{H}_2^{Air} = \bar{B}_2^{Air}/\mu_0$; due to boundary conditions, the field within the thin nickel plate is approximately the same as that measured in air: $\bar{H}_2^{Ni} \cong \bar{H}_2^{Air}$. This approximation was verified numerically with COMSOL, and yields an error smaller than 5%.

In each test, the static magnetic field within the material $\bar{H}_2$ and the velocity signal detected by the laser vibrometer $v_2(t)$ were measured. In this way, it was possible to compare the theoretical trend of $d_{61}\left(\bar{H}\right)$, computed according to Equation (3.26), against the experimental generation efficiency (Figure 5.8). The test was performed at three different centre frequencies: 100 kHz, 200 kHz and 300 kHz. The test was limited to the typical guided wave inspection range, as opposed to the bulk wave example of Section 5.2.3.

The comparison between the normalized experimental results and the numerical predictions yields excellent agreement, giving a first qualitative validation of the model. The shapes of the curves are not significantly affected by frequency: the trend is essentially the same, with a more pronounced reduction of the amplitude with frequency in the high bias field region. There is also a slight change in the position of the maxima of the curves at different frequencies. The trends of the experimental and FE results are consistent with each other but differ significantly from the trend of d_{61}. This behaviour may seem unexpected at first glance since $\widetilde{\epsilon}_6 \propto d_{61}\,\widetilde{H}_1$ (Equation (4.8)), and can be explained only if we account for other

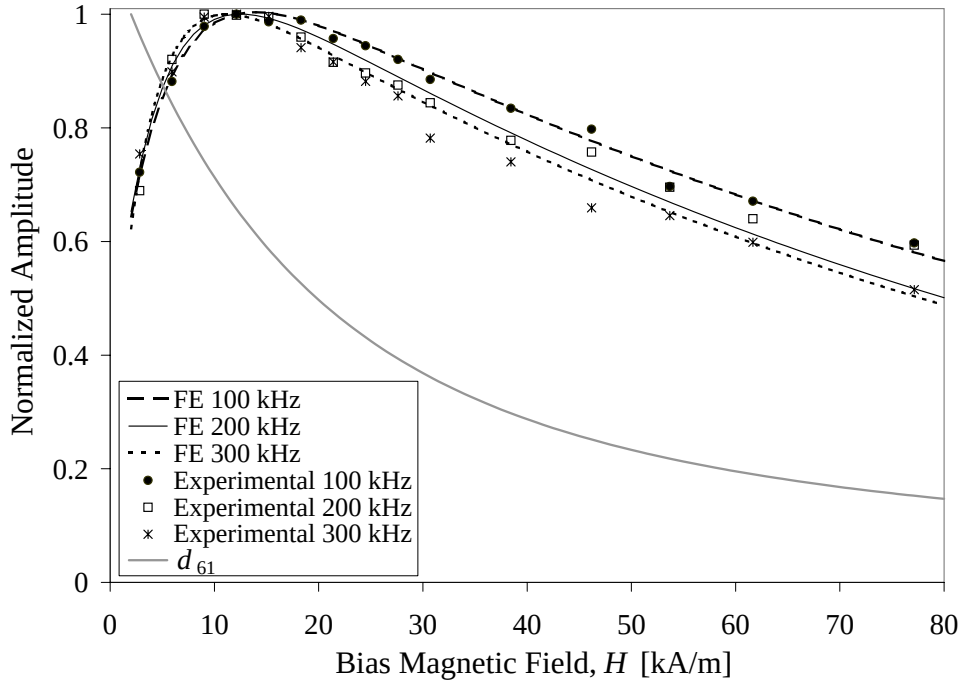

Figure 5.8: *Qualitative validation: normalized particle velocity amplitude as a function of the magnetic bias field. Experimental values are shown together with numerical predictions, for different frequencies. The trend of the magnetostriction constant d_{61} (grey line) is shown for comparison.*

phenomena taking place during the experiment. First of all, the relative magnetic permeability of the sample, μ_r, changes with the static magnetic field $\bar{H}_2$. Since nickel is ferromagnetic, its magnetization curve, B versus H, is a non-linear function (Figure 5.9 (a)). Consequently, the magnetic permeability $\mu_r = \frac{B}{\mu_0 H}$ is not a constant, and varies as a function of the static field: $\mu_r = \mu_r\left(\bar{H}_2\right)$. When the static and dynamic magnetic fields are parallel to each other, only the magnitude of the total field H changes, not the direction, thus the magnetic permeability is the differential one: $\mu_r' = \frac{1}{\mu_0}\frac{\partial B}{\partial H}$ (Figure 5.10 (a)); however in our case, the static and the dynamic magnetic fields are normal to each other and there is only a change in the direction of the total magnetic field, not in its magnitude (in the first order approximation), thus the static permeability, $\mu_r = \frac{B}{\mu_0 H}$, is the relevant parameter to be employed (Figure 5.10 (b)). If we consider the dynamic electric current carried by the wire, it causes a magnetic field within the nickel plate next to it, $\widetilde{H}_1$. It is known that the amplitude of the field inside the medium depends on its magnetic perme-

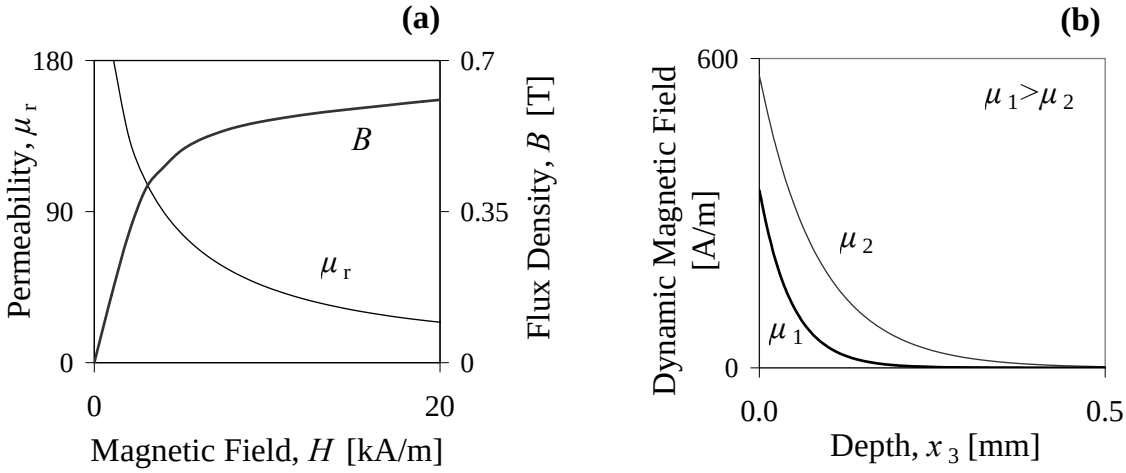

Figure 5.9: *(a) Magnetization curve and magnetic permeability of nickel, after Chen et al. [76]. (b) Distribution of the dynamic magnetic field over the thickness of a nickel plate for different relative permeabilities. Results from FE simulations with* $\mu_1 = 80$, $\mu_2 = 20$*; driving frequency* $f = 100\,\mathrm{kHz}$.

ability: the larger μ_r, the smaller the resulting magnetic field: $\widetilde{H}_1 = \widetilde{H}_1(\mu_r)$. This is a consequence of Ampere's law: the closed-loop integral of the magnetic field (in our case $\widetilde{H}$) must equal the total enclosed current. When the magnetic permeability of a ferromagnetic medium is high, the value of $\widetilde{H}$ in the material must be small to respect Ampere's equality, whereas if the permeability of the material is lower, the mismatch between the permeabilities of air and the medium is lower and $\widetilde{H}$ in the metal is higher. For the case of an infinite, straight current-carrying wire above a ferromagnetic semi-space the exact expression can be found in the literature [73]. The overall effect of these phenomena is that a variation of the bias field $\bar{H}_2$ affects the dynamic field $\widetilde{H}_1$, even if we provide the same driving current: $\widetilde{H}_1 = \widetilde{H}_1\left(\bar{H}_2\right)$. The variation of the magnetic permeability has a further consequence on the experiment: it affects the magnetostrictive force distribution over the depth of the sample. The penetration of the electromagnetic field in a metal is governed by an exponential decay, whose rate is determined by the skin depth parameter: $\delta \propto 1/\sqrt{\mu_r}$, [12]. The overall dependence of the dynamic magnetic field $\widetilde{H}_1$ on the static field $\bar{H}_2$ can

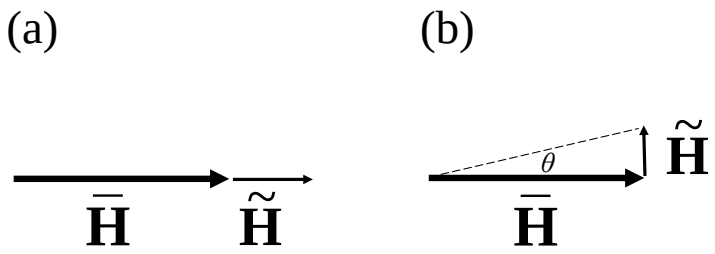

Figure 5.10: *Relative directions of the static ($\bar{\mathbf{H}}$) and dynamic ($\widetilde{\mathbf{H}}$) magnetic fields. (a) When they are parallel to each other, the total field $\mathbf{H} = \bar{\mathbf{H}} + \widetilde{\mathbf{H}}$ varies only in magnitude H, thus the relevant permeability is $\mu_r' = \frac{1}{\mu_0}\frac{\partial B}{\partial H}$. (b) When $\bar{\mathbf{H}}$ and $\widetilde{\mathbf{H}}$ are perpendicular, there is only a rotation $\theta \cong \widetilde{H}/\bar{H}$ of the total field (in the first order approximation), thus $\mu_r = \frac{B}{\mu_0 H}$. The amplitude of $\widetilde{\mathbf{H}}$ compared to $\bar{\mathbf{H}}$ is magnified in the figure for clarity.*

then be written as:

$$\widetilde{H}_1(\bar{H}_2,\, x_3) = \widetilde{H}_1(\bar{H}_2, 0)\; e^{-x_3/\delta(\bar{H}_2)}. \tag{5.3}$$

As a result, for high bias fields the permeability is low and the dynamic field penetrates deeper into the sample. This implies that the resulting magnetostrictive force is spread over the thickness and causes a larger amplitude SH0 wave. On the other hand, for low bias fields, the magnetic permeability is higher and the dynamic field is squeezed in a tiny portion of the thickness, generating lower amplitudes. The situation is illustrated in Figure 5.9 (b).

The conclusion is that considering Equation (4.8), both factors, d_{61} and $\widetilde{H}_1$, are functions of the static bias field, thus the EMAT field-dependent efficiency is not a function of the magnetostriction constant d_{61} alone: $\widetilde{\epsilon}_6 \propto d_{61}\left(\bar{H}_2\right) \cdot \widetilde{H}_1\left(\bar{H}_2\right)$. It should be noted that the magnetostriction and permeability counterbalance each other in transduction process: when d_{61} is large (i.e. for small $\bar{H}_2$), the high permeability tends to reduce the signal amplitude (because the dynamic field is squeezed over a small area), while for high bias fields a small permeability has the effect of partly compensating for the reduced value of the magnetostrictive constant.

Linearity with the driving current

Another important check for the applicability of the model is that the assumed linearity with the dynamic magnetic field (Equation (3.23)) is indeed observed in experimental tests. Keeping a constant magnetic bias field, $\bar{H}_2 = 15\,\mathrm{kA/m}$ and a fixed excitation frequency, $f = 100\,\mathrm{kHz}$, the amplitude of the driving current was varied from about 1.3 A to 3.8 A peak to peak. This range corresponds to a maximum dynamic field amplitude between 0.3 kA/m and 1.9 kA/m. The resulting measured particle velocity amplitude is shown in Figure 5.11, as a function of the driving current. The linear trend is evident, confirming that Equation (3.23) can be successfully applied over a range of different driving currents. In the case studied, the hypothesis $\bar{H} \gg \widetilde{H}$ was always satisfied, since even with the maximum driving current $\bar{H}/\widetilde{H} \cong 8$, where the dynamic field is a maximum, i.e. at the surface of the metal, just below the wire. The numerical model is linear in $\widetilde{H}$, according to Equation (3.23), thus the FE simulations show a linear dependence of the particle velocity with the dynamic field and the driving current.

5.6.2 Quantitative validation

The qualitative validation undertaken in the previous section demonstrates that the physics of the transduction mechanism is properly portrayed by the model, however it is paramount to assess the performance of the model in an absolute, quantitative manner. The experiment described in the previous section was repeated with the magnetic bias field kept constant at $\bar{H}_2 = 15\,\mathrm{kA/m}$, while the frequency was varied between 90 kHz and 300 kHz in 10 kHz steps. The velocity signal was again detected by the laser vibrometer $v_2(t)$ while the driving current $I(t)$ through the wire was recorded using a current transformer (Bergoz CT-B1.0), typical signals are shown in Figure 5.12. Both the driving and received toneburst were gated and a Fast Fourier Transform was applied. The spectrum of the measured velocity was divided by the spectrum of the driving current to give the particle velocity per unit current at each frequency. This was a necessary step since the Finite Element simulations were

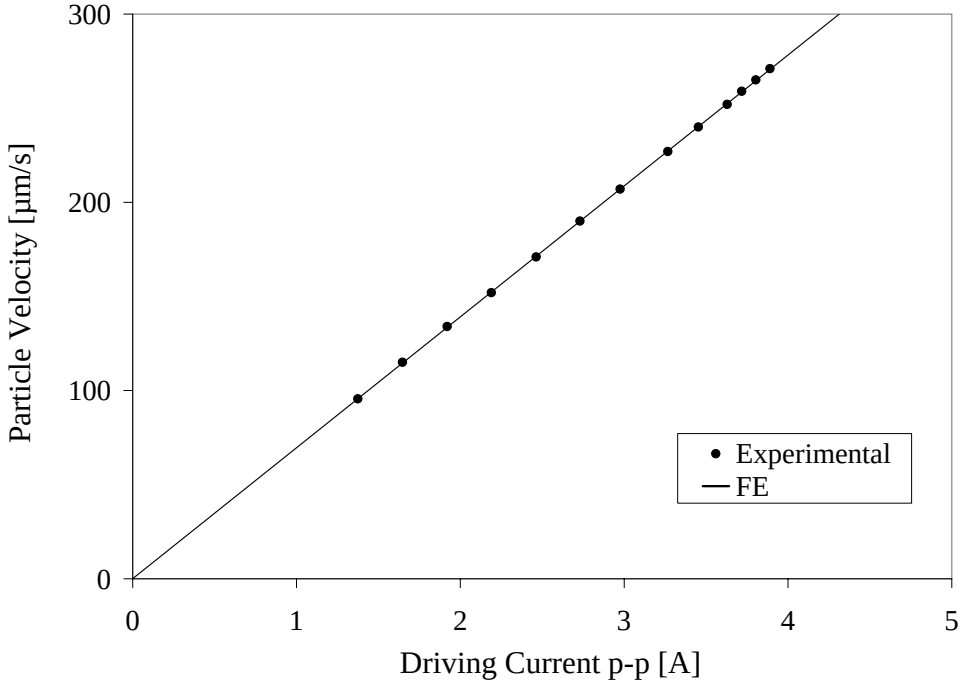

Figure 5.11: *Qualitative validation: particle velocity as a function of the amplitude of the driving current for* $\bar{H}_2 = 15\,\mathrm{kA/m}$ *and* $f = 100\,\mathrm{kHz}$*. Experimental data (dots) and the result of a FE simulation (continuous line) are shown. The uncertainty of the experimental points is* $\pm 3\,\mu\mathrm{m/s}$*.*

performed in the frequency domain, i.e. a single frequency, harmonic solution was computed. The actual physical properties of the nickel plate were used in the FE model: magnetostriction constants were computed from the measured magnetostriction curve, according to Equations (3.25)-(3.26), while magnetic permeability was obtained from an experiment performed by Chen *et al.* [76] on a pure nickel sample. The comparison between the predicted and measured velocities is satisfactory as the error is within 20 % over a significant frequency range, from 90 kHz to 300 kHz (Figure 5.13).

5.7 Mutual coupling

Another significant result that can be obtained with the model is the assessment of the mutual coupling effect, since no study had previously addressed its contribution.

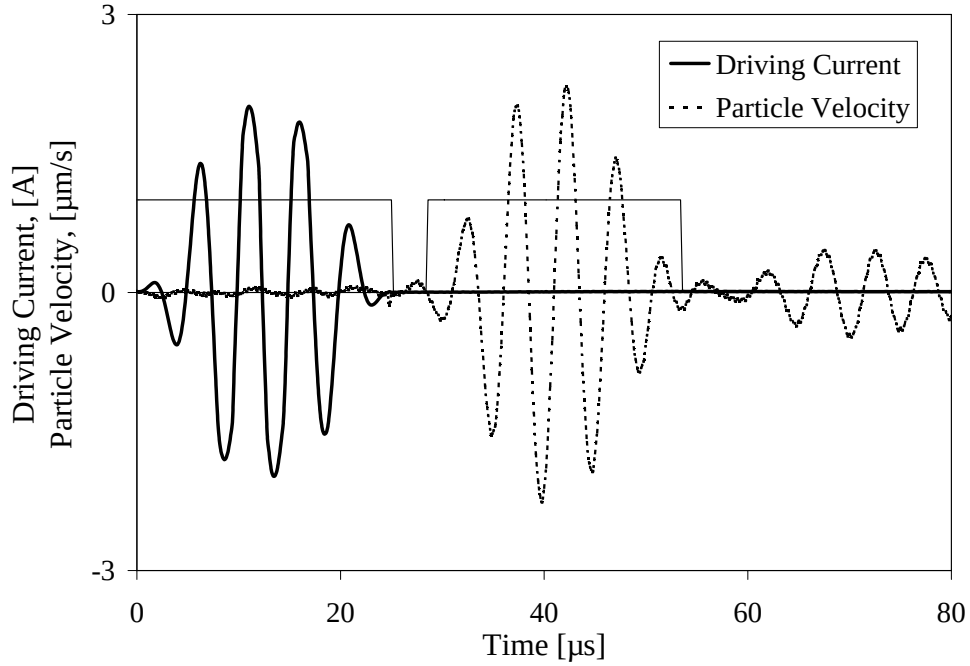

Figure 5.12: *Driving current signal (solid line) and received particle velocity (dashed line). Bias field* $\bar{H}_2 = 15\,\mathrm{kA/m}$*, frequency* $200\,\mathrm{kHz}$*. Continuous flat lines show the rectangular windows used for signal processing.*

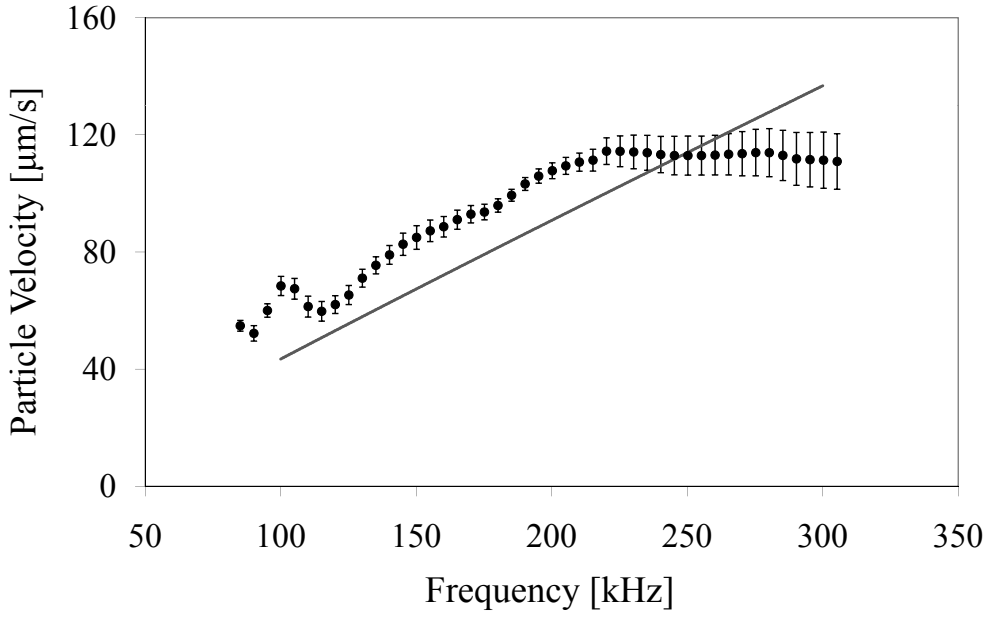

Figure 5.13: *Quantitative validation. Predicted (solid line) and measured (points) absolute velocities as function of driving frequency for* $\bar{H}_2 = 15\,\mathrm{kA/m}$*.*

The mutual coupling effect can be explained as follows: the dynamic magnetic field superimposed on a strong bias field causes dynamic strains (first equation of (4.8)); in turn, the elastic stress resulting from this strain affects the dynamic magnetic field that has generated it (second equation of (4.8)), establishing an inverse effect, in a similar fashion to the back electromotive force effect. By comparing the simulations in which the term $(d_{61}\,\widetilde{\sigma}_6)$ of the second row of Equation (4.8) was non-zero against those in which it was arbitrarily set to zero, it was possible to establish that there is indeed an effect, however it results in a variation of only around 1% of the generated displacement. In conclusion, the mutual coupling effect is negligible from a practical point of view, at least for the transducer under study in the operational conditions considered.

5.8 Discussion

5.8.1 Qualitative validation discussion

The qualitative validation process has highlighted that the optimization of a magnetostrictive transducer cannot rely on the simple study of the magnetostriction coefficients. In the case analyzed in this study, consideration of the magnetostrictive coefficient alone would indicate that optimal transduction is obtained with a small static field (Figure 5.8). On the contrary, the analysis undertaken and the experiment have shown that the optimal operation point of this EMAT, in the conditions addressed, occurs for specific values of the bias field, at the maxima of the FE trends of Figure 5.8, according to the driving frequency employed.

These features underline the significant difference between the Lorentz force and the magnetostriction mechanisms. The Lorentz force is simply a linear function of the bias field: the higher the magnetic field the larger the obtained signal; also, in the limit $\delta/\lambda << 1$ [6], the conductivity does not affect the transduction efficiency. On the other hand, magnetostriction is not a linear function of the static field (Figure 5.8) and its amplitude depends on the electromagnetic skin depth. When

different bias fields $\bar{H}_2$ are used, the magnetic permeability changes; however, not only does the distribution of the dynamic magnetic field in the material change, but also its total value given by the integral over depth is different (Figure 5.9 (b)). Since the generated wave amplitude is proportional to the dynamic field (in Equation (4.8) we have $\widetilde{\epsilon}_6 \propto \widetilde{H}_1$), this effect implies that the sensitivity of the sensor strongly depends on the phenomena taking place in the skin depth.

5.8.2 Quantitative validation discussion

The absolute validation of the model was successful (Figure 5.13), however a degree of discrepancy between the predicted values and the experimental data is present and has to be investigated. There are several sources of different nature that contribute to this discrepancy.

Uncertainty in the numerical model

Uncertainties in the numerical simulations are due to computational limitations: as mentioned, the model is extremely demanding, the maximum number of elements is limited by the total available memory of the computer. As a result, a trade-off is needed between the number of elements employed and the resolution of the skin depth and the wavelength in the magnetostrictive area in the elastic region respectively. As mentioned in Section 4.4, three elements through skin depth and around 15 elements per wavelength were used. This leads to a small but non-negligible uncertainty in the numerical results.

Uncertainty related to the ferromagnetic modelling

Other significant uncertainties are due to the physical variability of the magnetic properties of ferromagnetic materials. It is well-known from eddy-current inspection that flawless, apparently homogeneous ferromagnetic media show significant signal variability when spatial scans are performed [77]. This is attributed to spatial vari-

ations of the magnetic permeability caused by different surface conditions, residual stresses, magnetization history and aging effects [77]. Similar variabilities and dependencies affect magnetostriction, as highlighted in Figure 5.6. The conclusion is that the validity of the physical model of a perfectly homogeneous ferromagnetic medium is debatable. For instance, the existence of a ferromagnetic "dead layer" has been proposed [77,78], i.e. a thin ($10-100\,\mu$m) surface layer whose permeability is significantly lower than the bulk of the material. The use of this physical model in the FE simulations might have improved the final outcome of the validation, however the correctness of this assumption is still uncertain and is beyond the scope of our investigation, thus the homogeneous ferromagnetic medium model has been employed.

Frequency dependence of magnetic properties

A further problem related to the magnetic properties is their frequency dependence. The values of the permeability μ_r and the magnetostrictive coefficients d_{ij} were obtained in static conditions. Using these dc values at frequencies in the order of a few hundreds of kHz assumes that they do not vary with frequency. Experimental investigations with different techniques like inductance measurements [79, 80] and potential drop measurements [81], have shown that the relative permeabilities of pure ferromagnetic metals like iron and nickel exhibit a significant frequency dependence. In the case of nickel, from reference [79] it can be estimated that the value of μ_r at 300 kHz decreases by up to 20 % compared to the value at 100 kHz. There are currently no studies on the frequency dependence of magnetostrictive properties, however, since both magnetic permeability and magnetostriction are macroscopic quantities accounting for the overall effect (elastic or magnetic) of the same microscopic phenomena, i.e. domain motions, similar effects observed on the magnetic permeability can affect magnetostrictive parameters. It can be hypothesized that, at sufficiently high frequencies, the domain motion lags behind the magnetic field [81], resulting in a reduced magnetostrictive parameter value. A consequence of the frequency variations of μ_r and d_{ij} could be the non-linear trend of the experimental

plot of Figure 5.13.

All these issues show that most uncertainties are due to deficiencies in the understanding of ferromagnetic media and the frequency dependence of magnetic properties, both being physical problems rather then problems of the model under investigation. Given all these difficulties, and the fact that an absolute validation of a magnetostrictive model had never been reported before, we can conclude that the absolute validation gives an encouraging result.

5.9 Conclusions

The FE model presented in Chapter 4 and based on the theory outlined in Chapter 3 allows the simulation of complex 3D configurations; as an example the wave generation of a SH wave magnetostrictive transducer, operating on a nickel plate, has been successfully predicted.

The model has been qualitatively validated by experiments addressing the static magnetic field and the driving current dependence of the transduction. The validation has highlighted that the sensitivity is not only a function of the magnetostrictive coupling constants: the magnetic permeability has a fundamental effect too, since it affects both the penetration depth in the sample of the dynamic magnetic field and its amplitude. It has also been verified experimentally that the generation sensitivity is linearly proportional to the dynamic field and thus to the driving current, at least when the bias field is significantly larger than the dynamic field.

The predictions of the model have been quantitatively compared with experimental data. This absolute validation was successful with a discrepancy smaller than 20 % over a 200 kHz frequency range. The error is largely due to the physical uncertainties in the magnetic properties and to their frequency dependence.

The following chapters will show how the model can be exploited for the assessment of very different EMAT configurations for SH wave inspection (Chapter 6) and the

study of bulk wave EMATs operating on steel components (Chapter 7).

Chapter 6

Assessment of SH wave EMAT performance

6.1 Introduction

In this chapter the experimentally validated FE model is used to assess the performance of the main EMAT configurations for SH waves when used on steel plates. After a description of the most important types of shear horizontal wave EMATs, simulations and experimental tests are employed to compare the performance of their basic units. The FE model is also used to evaluate how key design parameters influence the sensitivity of the different kinds of probes. The quantitative results of this analysis, together with the practical issues associated with each configuration, allow the relative advantages and disadvantages of the transducers to be assessed.

6.2 EMATs and guided wave inspection

One of the most attractive features of EMATs is their capability of generating a wide range of ultrasonic wave-modes, by careful design of their geometric configuration [6, 7], including shear horizontal (SH) waves in plate-like structures or torsional waves

in pipe-like components.

The fundamental shear horizontal (SH0) and torsional (T(0,1)) waves are of practical importance in guided wave inspection due to their non-dispersive character, i.e. their group and phase velocities are not frequency-dependent, simplifying the interpretation of signals. Furthermore, these wave-modes do not show any out of plane particle displacement, thus they are not affected by the presence of (non viscous) liquids in contact with the wave-guide [82].

Shear horizontal and torsional waves are closely related: essentially a SH wave in a plate structure is the equivalent to a torsional wave in a tubular structure [83]. Therefore, although this chapter investigates the performance of different EMAT configurations for SH waves on plates, the analysis can readily be extended to EMATs producing torsional waves in pipes.

EMATs generate and detect ultrasonic waves chiefly via the Lorentz force and magnetostriction. While in some cases these two mechanisms are additive, for example in the generation of bulk shear waves (as we will see in Chapter 7), when SH waves are to be produced, very different configurations have to be devised depending on the transduction effect that one wants to exploit. This results in two main families of transducers: Periodic Permanent Magnet (PPM) EMATs, which are based on the Lorentz force [5, 25], and magnetostrictive EMATs, based on magnetostrictive effects occurring in the sample itself or in a strip of highly magnetostrictive material bonded on the testpiece [17, 26, 28, 47]. Both solutions are employed in practical applications, and have distinct advantages and disadvantages.

6.3 EMAT configurations for SH waves

Let us consider a reference system $\{x_1, x_2, x_3\}$ and a plate lying in the $x_1 - x_2$ plane. In order to generate horizontally polarized shear waves, i.e. with particle motion along the x_2 direction, with wavelength λ and propagating in the direction x_1, different EMAT configurations can be used. Figure 2.4 shows the reference system

that will be used throughout this analysis, together with the schematic diagram of two SH wave EMAT configurations. The main options available are described in the following sections.

6.3.1 Periodic Permanent Magnet (PPM) EMAT

Taking advantage of the Lorentz force, SH waves can be generated by using a periodic arrangement of permanent magnets, producing a bias magnetic flux density $\bar{B}_3$ with period (along direction x_1) equal to the acoustic wavelength λ (Figure 2.4 (a)). A straight wire, placed between the magnets and the plate, carries a current I and induces eddy current density J_{e1} in the plate. According to Equation (3.8), this produces a pattern of alternating body forces in the x_2 direction $f_2 = -J_{e1} \cdot \bar{B}_3$, launching SH waves (Figure 6.1 (a)). This basic structure can be enhanced by winding the wire several times around the magnets, thus linearly increasing the total current density: $J_e^{tot} = n_{turns} \cdot J_{e1}$. Improvements to this design can employ a linear racetrack coil and two lines of periodic magnets next to each other, to maximize the total current density in the plate; other designs use appropriate phase shifts in different PPM elements to achieve substantially unidirectional waves [6, 22, 25].

6.3.2 Magnetostrictive EMATs

An alternative way to produce SH waves exploits magnetostriction, as described in Section 4.4. A static magnetic field $\bar{H}_2$ is applied along the x_2 direction. A straight current-carrying wire, is placed along the direction of the magnetic bias field, producing a dynamic magnetic field $\widetilde{H}_1$ along the x_1 direction (Figure 6.1 (b)). The static and dynamic magnetic fields are perpendicular to each other; the tilting of the total magnetic field $\mathbf{H}$ during operation causes shear strains $\widetilde{\epsilon}_6$ in the plane of the plate, $\{x_1, x_2\}$ that result in SH waves propagating along the x_1 direction [26]. The magnetostriction constitutive equations for this configuration have been given in Chapter 5 (Equations (4.6)-(4.7)) and they practically reduce to the system of Equation (4.8).

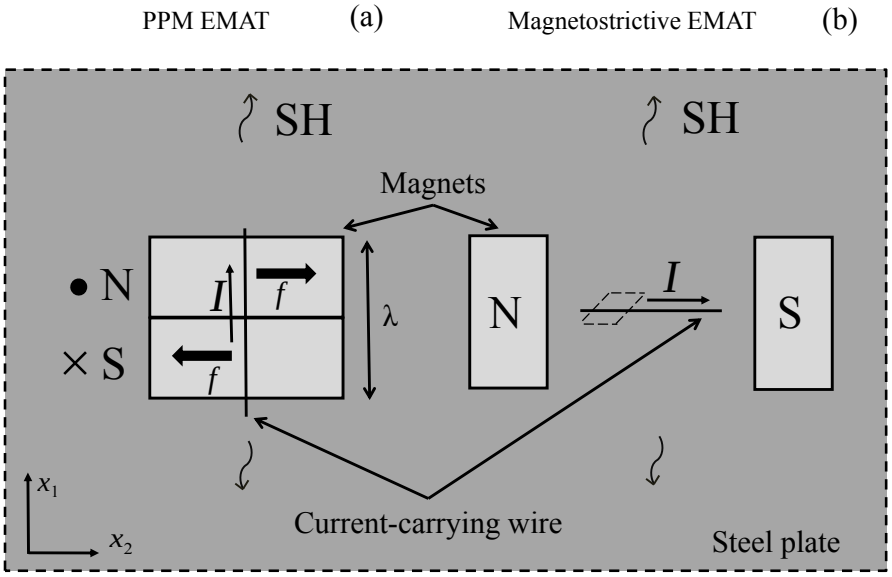

Figure 6.1: *Schematic diagram of the elemental components of (a) PPM and (b) magnetostrictive and EMATs. Top view (x_1-x_2 plane) in a reference system consistent with that defined in Figure 2.4. The same magnets (indicated in light grey), wires and lift-off are used in both the configurations. The wires are driven by the current I. In (a) the thick arrows represent the Lorentz force, f, in (b) the magnetostriction shear strain of an elemental area below the wire is shown (dashed parallelogram). The steel plate is shown in dark grey.*

In actual tests, rather than using a single straight wire, a meander coil with spacing $\lambda/2$ can be used, in order to exploit constructive interference phenomena (Figure 2.4 (b)). Also, the wire can be wound several times to increase the total dynamic field available. This EMAT set-up can operate only on ferromagnetic materials, and its performance depends strongly on the magnetostrictive properties of the sample. A possible solution to this problem is to attach a highly magnetostrictive material, like nickel or an iron-cobalt alloy, onto the sample [47,84]; this can be done by adhesive bonding or, in some cases, via shear couplant. In this way, high signal-to-noise ratios can be obtained at the cost of increasing the complexity of the transducer and losing its non-contact nature. This solution can be employed in structural health monitoring [85].

A large number of variants to the EMAT configurations described above have been reported [25,27,47,84,86]. Our study will focus only on three configurations: PPM EMAT, magnetostrictive EMAT and magnetostrictive EMAT with bonded nickel strip. In order to obtain a fair comparison between the transducers, the very basic, ideal, configurations shown in Figure 6.1 are to be examined. Transducers used in practice such as those shown in Figure 2.4 are a sum of these basic units; by analyzing the performance of the essential components we can assess the effectiveness of the transduction process. For both PPM and magnetostrictive EMATs, the real multi-turn coil is reduced to a single straight wire element, fed by the same driving current and placed at the same lift-off distance from the plate. The bias magnetic field in all the cases is provided by two permanent magnets; exactly the same hardware and driving inputs are used in all the experiments and the same physical parameters are used in all the numerical simulations. The following sections describe the simulations and the experiments used to assess the performance of the probes.

6.4 FE simulations and experimental study

6.4.1 Numerical model

The single wire configurations of Figure 6.1 yield very low signal amplitudes in experimental tests on plate thicknesses of practical interest. In order to compare the FE results with the measurements, the test object for all the simulated transducers is a 0.5 mm thick steel plate. Since for excitation within a very shallow subsurface layer the wave amplitude of shear horizontal modes is inversely proportional to plate thickness, the small thickness chosen yields relatively high signal amplitudes in experimental tests. The measured signals can then be used to validate the model simulating the conditions analogous to the experiment, i.e. the model and the actual test employ the same plate thickness as well as the same dimensions and relative position for the magnets and the wire. The plate has the material properties of mild steel, listed in Table 6.1. Since the magnetic permeability and the magnetostric-

Table 6.1: *Summary of the material properties used in the FE model.*

Material	Young's modulus [GPa]	Poisson's ratio	Mass density [kg/m^3]	Electrical conductivity [MS/m]
Steel	200	0.33	7850	4.0
Nickel	200	0.29	8900	14.3
Epoxy	1.6	0.34	1170	0

tion constants are functions of the magnetic bias field, they are given by graphs. The magnetostriction constant d_{61} was obtained by applying Equation (3.26) to the magnetostriction curve of a mild steel given in the literature [11], shown in Figure 3.1. The magnetic permeability curve of mild steel is shown in Figure 6.2. For comparison, the permeability curve of nickel is also shown.

In order to simulate an infinite plate, an elastic disk surrounded by an annular absorbing region with non-zero damping coefficient was modelled. A 1 A driving current oscillating at 150 kHz was fed to the wire, lying above the disk, 0.1 mm away from it. The chosen frequency-thickness product is well below the first cut-off frequency of higher order SH modes, so only the fundamental mode (SH0) is generated. Moreover, the driving frequency is representative of experimental conditions found in practice: frequencies in the range 10-250 kHz are often used [46, 82, 87], depending on the thickness of the testpiece and other experimental considerations. To further reduce the number of elements, mechanical and electromagnetic symmetries are exploited as discussed in Section 4.4.

6.4.2 Experimental validation

All the numerical results obtained with the FE model have been supported by experimental data. PPM and magnetostrictive EMATs were used on a 0.5 mm thick mild steel plate. For the PPM EMAT, the bias magnetic field was provided by two $20 \times 10 \times 5$ mm NdFeB permanent magnets (Eclipse Magnetics). The magnets were placed with opposite polarization (Figure 6.1 (a)), in order to mimic a unit compo-

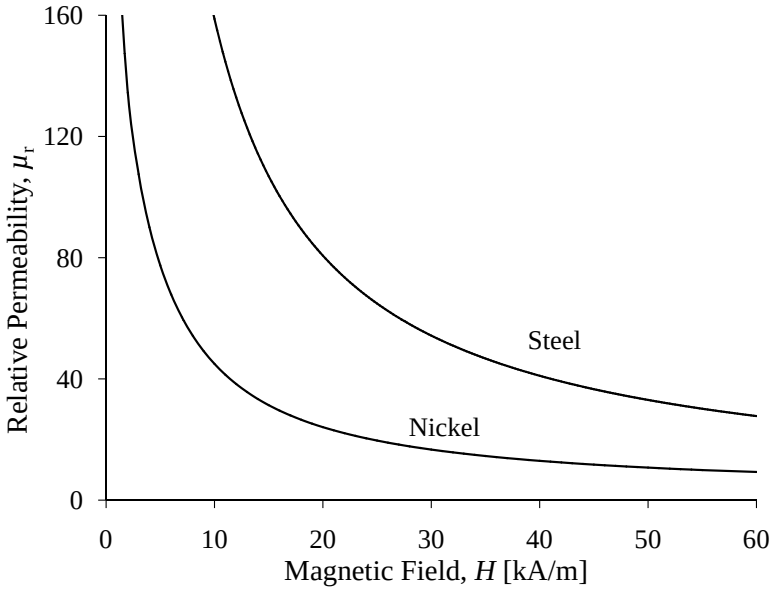

Figure 6.2: *Permeability curves of nickel and mild steel. Data from [11] (steel) and [76] (nickel).*

nent of a PPM EMAT, with spatial period 20 mm. The driving frequency chosen was 150 kHz, such that only the fundamental shear horizontal mode was generated, moreover the acoustic wavelength at this frequency is approximately 20.6 mm, close to the periodicity of the magnets, such that wave generation is maximized due to interference phenomena. The magnitude of the magnetic flux density in air, normal to the surface of the sample, $\bar{B}_3^{air}$ was measured with a Hall effect gaussmeter (GM04, Hirst Magnetics). The magnetic flux density within the plate, near its surface, was assumed to be equal to the value measured in air since the boundary conditions for $\mathbf{B}$ prescribe the continuity of its normal component: in our case $\bar{B}_3^{sample} \cong \bar{B}_3^{air}$.

For the magnetostrictive EMATs, the same permanent magnets used for the PPM EMAT were arranged in the configuration depicted in Figure 6.1 (b). Two magnetostrictive EMATs were tested: in one case the transducer was placed directly on the steel plate, while in the second type of EMAT a 100×25 mm, 0.5 mm thick nickel plate was bonded on the steel plate with epoxy. In practical applications, materials showing higher magnetostriction than nickel, such as iron-cobalt alloys [85], are commonly used to improve the signal amplitude. Here nickel was chosen as its static magnetostriction curve had already been measured for the quantitative validation

of the FE model (Section 5.5).

A structural adhesive film (3M AF163-2) was cured at 120 °C for 90 minutes while subject to a 0.15 MPa pressure. During the process the viscosity of this kind of film increases, reducing the adhesive flow-out [88]; this yielded a fairly uniform bondline, approximately 200 μm thick. The magnetic field within the sample, parallel to the surface of it, was estimated with the method outlined in Section 5.5.

The in-plane particle velocity produced by each transducer at a distance of 65 mm from it was detected by a laser Doppler vibrometer. The same experimental method used for the validation of the model (Section 5.6) was used. Two Polytec OFV 505 heads (OFV 5000 controllers) were oriented at $\pm 30°$ from the normal of the plate. Since laser vibrometers detect the velocity along the optical path of the laser beam, a simple trigonometric formula [89], accounting for the incident angle, has to be used to obtain the in-plane (or the out-of-plane) particle velocity (Figure 5.7). The current transformer measured the driving signal, a 4 A peak to peak, five-cycle toneburst, with centre frequency $f = 150$ kHz and both the driving and received signals were gated and fast Fourier transformed. The ratio between the velocity and driving current spectra at the centre frequency yielded the experimental particle velocity per unit current and was then compared with the single frequency numerical simulations.

6.5 Analysis of performance of different configurations

The overall results of the experimental and numerical investigations are summarized in Figure 6.3. The measured and simulated particle velocities per unit input current on a steel plate are plotted against the magnetic bias field $\bar{H}$. The continuous plots show the FE results for the three EMAT configurations analyzed, while the points represent the experimental measurement obtained for the corresponding transducer, all obtained using the same hardware, i.e. permanent magnets, wire and input

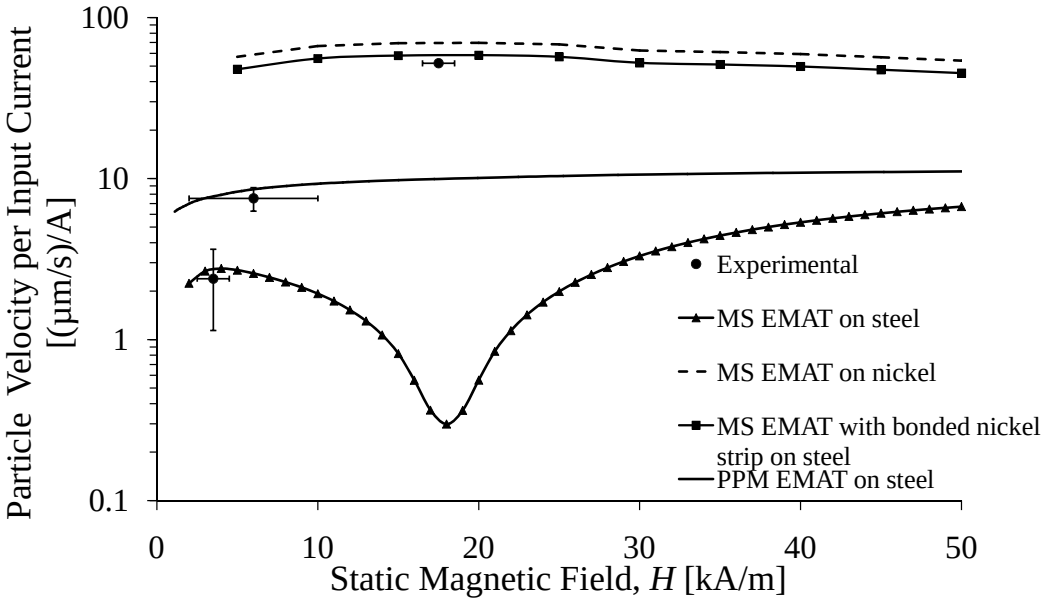

Figure 6.3: *Simulated and experimental performance of different EMAT configurations as a function of the magnetic bias field* $\bar{H}$ *on a* 0.5 mm *thick steel plate. The continuous plots represent the predicted FE amplitudes, while the points show the corresponding measured values using the same set of hardware (magnets, driving current, lift-off), with experimental error bars. The FE predictions for a magnetostrictive EMAT operating on a* 0.5 mm *thick nickel plate are also shown for comparison (dashed line).*

signal. The performance of a magnetostrictive EMAT operating on a 0.5 mm thick nickel plate is also reported for comparison (dashed line); this FE prediction was validated in Chapter 5. While we can easily sweep through a large range of values of the static bias field $\bar{H}$ with FE simulations, in experimental conditions, if a fixed arrangement of permanent magnets is employed, we have only one operation point $\bar{H}$ for each transducer. In practice, other operation points can be obtained by changing the magnetic circuit of the transducer, for example altering the distance between the magnets of Figure 6.1 (b), or by using electromagnets driven by adjustable current [33]. Here we are interested in the performance obtained using a given set of hardware in a given geometric configuration, therefore only one experimental point is obtained for each configuration. Figure 6.3 shows that the magnetostrictive EMATs operate at different bias fields even if the same permanent magnets are

used; this is a consequence of the different magnetic permeabilities of steel and of the bonded nickel plate. Since μ_r^{ni} is significantly lower than μ_r^{steel} (Figure 6.2), the resulting bias field in nickel is higher than in steel. The experimental operation points $\bar{H}$ of the magnetostrictive EMATs were determined using the method outlined in Section 5.5. With the PPM EMAT, the magnetic flux density in the sample in the direction normal to the plate can be measured, $\bar{B}_3 = 550\,\mathrm{mT}$, but the corresponding value of magnetic field strength $\bar{H}_3$ can be deduced only knowing the magnetization curve of the sample. In this study the B-H curve of steel was not measured, and $\bar{H}_3$ was estimated by inputting to a magnetic FE model a non-linear experimental constitutive equation taken from the literature [11]. Since the operation point lies after the "knee" of the magnetization curve, i.e. where the curve is relatively flat, a small uncertainty in the measurement of $\bar{B}_3$ corresponds to a wide range of values of $\bar{H}_3$, leading to the uncertainty bar on the abscissa of the PPM EMAT point in Figure 6.3.

The experimental error bars in the amplitudes are defined as the standard deviation over five repetitions of the measurement, each time trace being averaged 500 times. For the PPM EMAT and the magnetostrictive EMAT this uncertainty is only $\pm 1\,\mu$m/s while it is larger for the bonded nickel magnetostrictive EMAT, due to reverberations in the magnetostrictive layer, as will be discussed in Section 6.5.3. Overall, the maximum SH amplitude is obtained on the nickel plate with a magnetostrictive transducer. On the steel plate, the best performance in terms of amplitude is achieved by the bonded nickel magnetostrictive EMAT, followed by the PPM EMAT; the lowest wave amplitude is obtained by the magnetostrictive EMAT directly placed on the steel plate.

The magnetostrictive SH wave EMAT applied on the steel plate can be used to provide a further validation of the magnetostrictive FE model presented in Chapter 4. The experiment performed on a nickel plate in Section 5.6 can be repeated on the steel plate, i.e. the absolute wave amplitude can be measured with the laser vibrometers as a function of the magnetic bias field applied by means of electromagnets. In Figure 6.4 (a), the experimental results are compared (in a linear scale) to

the FE simulations presented in Figure 6.3. First of all, the model is again able to predict the correct order of magnitude of particle velocity without the need for any adjustable parameters. Since this EMAT configuration relies on the magnetostrictive parameter d_{61} to generate SH waves (Section 4.4), the field dependence of signal amplitude is expected to follow a trend similar to the one shown in Figure 3.3 (b), with a minimum occurring when the magnetostriction curve of the material crosses the abscissa axis, together with a π phase shift due to the change of sign of the static magnetostriction curve. The experiments performed show such features for $\bar{H} \cong 10\,\mathrm{kA/m}$, where the signal amplitude shows a minimum and the phase (Figure 6.4 (b)) is subject to an almost π shift. The disagreement in the position of the minimum between the FE simulations and the experimental data is due to the fact that, differently from the validation performed in Chapter 5, the magnetostriction curve of the steel plate under examination was not measured, and a curve for a mild steel taken from the literature was used to compute the magnetostriction constants [11].

Given this purely numerical evaluation for the basic unit of each transducer, it is important to assess how this relates to practical EMATs and how the performance is affected by relevant parameters such as the thickness of the plate, its electromagnetic properties or the properties of the bond when present. Since comparison between the FE predicted amplitudes and the experimental data shows satisfactory agreement, the assessment of the different configurations has been carried out with the validated numerical model.

6.5.1 PPM EMAT

This Lorentz force EMAT behaves linearly with the induced current density and the bias magnetic flux density according to Equation (3.8). Given a driving current I, the total induced current is independent of the thickness of the plate t_{steel}, provided it is much thicker than the electromagnetic skin depth, i.e. $t_{steel} > 3\delta$. The other term appearing in Equation (3.8), the magnetic flux density, is also slightly affected by the thickness of the plate. Figure 6.5 shows a simulation of the static flux density

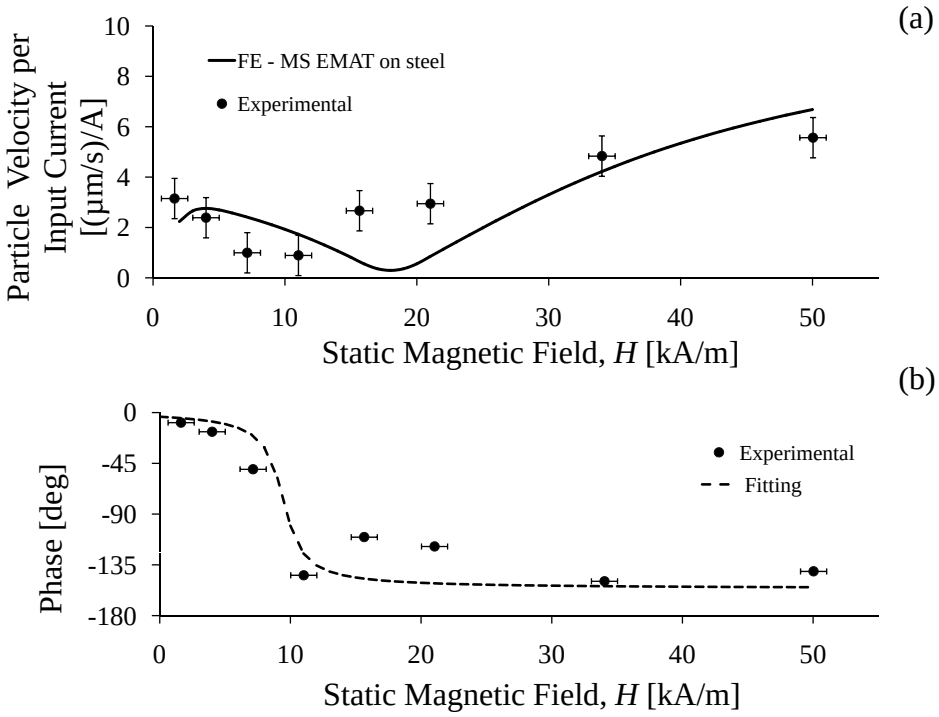

Figure 6.4: *(a) Quantitative validation of the FE model on steel for the magnetostrictive SH wave EMAT. Predicted (solid line) and measured (points) amplitude of particle velocity as a function of the magnetic bias field. (b) Measured phase (points) as a function of the magnetic bias field. The dashed curve shows a fitting function of the experimental data.*

$\bar{B}_3$ versus plate thickness. The magnitude on the surface of the sample, just below the centre of the magnet is shown. The variations are small, and for $t_{steel} > 5\,\text{mm}$, $\bar{B}_3$ is virtually constant. This implies that the electromagnetic phenomena are decoupled from the thickness of the plate. This is confirmed by simulations showing that the generated wave amplitude is inversely proportional to the thickness of the plate as would be the case with piezoelectric transducers (Figure 6.6). It will also be shown in Chapter 7 that Lorentz force EMATs are not significantly affected by the electromagnetic properties of different steels, such as the electric conductivity and the magnetic permeability, at least when $\delta/\lambda << 1$ [6]. The substantial insensitivity of this type of transducer to geometric or material properties of the testpiece makes it very versatile and robust to external conditions. On the other hand, it is also difficult to improve the signal amplitude given a limiting driving current and number of turns in the coil. For example, the bias magnetic flux density

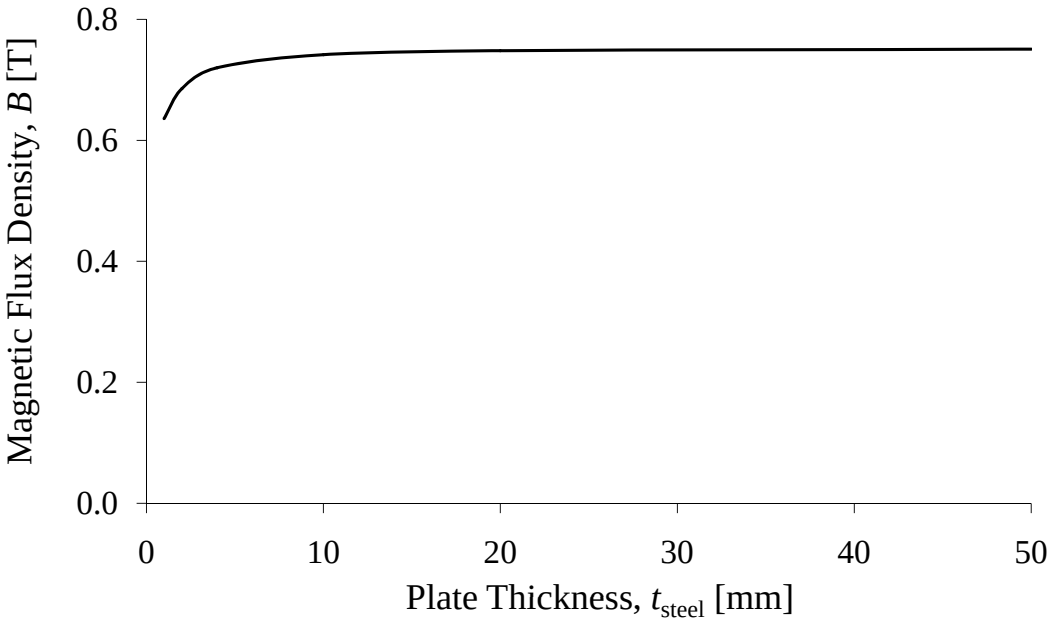

Figure 6.5: *Simulated magnetic flux density, B, due to a cylindrical permanent magnet on a steel plate as a function of the thickness of the plate. The magnitude of B on the surface of the steel plate, corresponding to the centre of the magnet, is shown. The component of B perpendicular to the plate is shown.*

produced by a single NdFeB permanent magnet is unlikely to exceed $\approx 1.3\,\mathrm{T}$ unless using special configurations [90], since this is the magnetic remanence of the material and even using electromagnets there is the upper limit of the magnetic saturation of steel around 2.2 T [12].

6.5.2 Magnetostrictive EMAT

Figure 6.3 shows that a magnetostrictive EMAT placed directly on the steel plate has a poor performance compared to the other configurations. The wave amplitude generated is four times smaller than that with a PPM EMAT and is more than an order of magnitude lower than that produced by a nickel bonded magnetostrictive EMAT. It should also be noted that these figures refer to the generation process only; in a pulse-echo test they would be squared. Ogi and co-workers [27] have proposed an enhanced configuration in which the magnetic bias field and the current-carrying

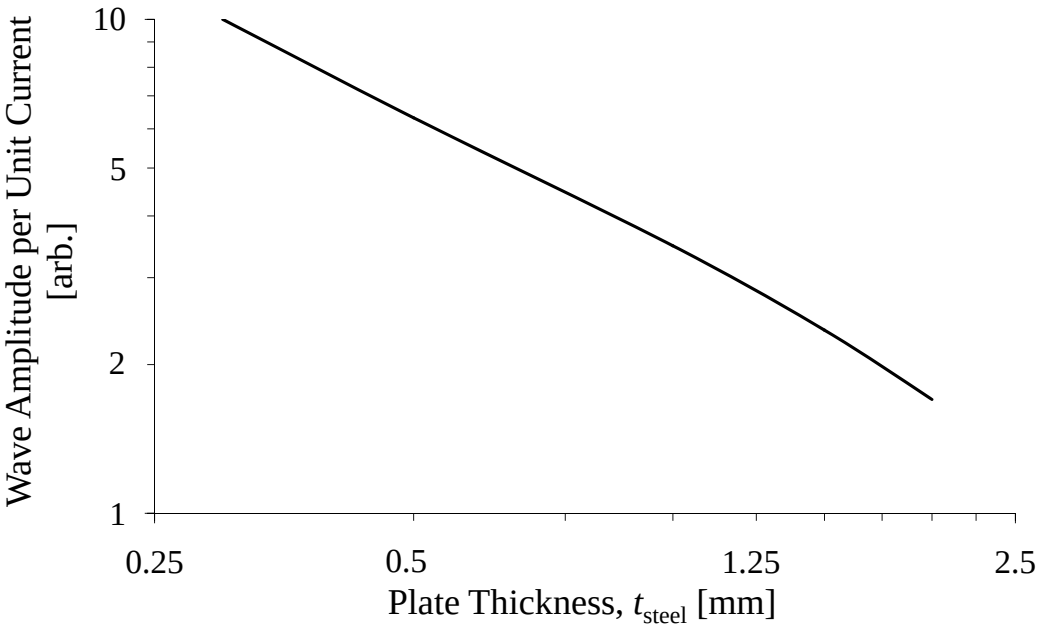

Figure 6.6: *Simulated wave amplitude produced on a plate by a PPM EMAT as a function of the thickness of the plate. As expected for a constant excitation, amplitude is inversely proportional to plate thickness.*

wire are inclined of an angle of around $\theta = 45°$. In this way, not only is the wave amplitude proportional to the magnetostrictive coefficient d_{61} (Equation (4.8)), but also to the coefficient d_{22}, leading to a signal amplitude 2.5 times larger than in the original configuration with $\theta = 0°$. However, even with this improvement, a significant disadvantage of this EMAT is its non-linear behaviour with the magnetic bias field $\bar{H}$. This is due to the highly non-linear and non-monotonic behaviour of the magnetostriction curve of steel (Figure 3.1); this causes large variations in the magnetostrictive coefficient $d_{61}\left(\bar{H}\right)$ and consequently in the resulting signal amplitude. In contrast to PPM EMATs, the magnetic bias field parallel to the surface of the sample $\bar{H}_2$ is severely affected by the thickness of the plate, as shown in the FE results of Figure 6.7, where the magnitude of $\bar{H}_2$ at the surface of the steel plate, half way between the two magnets (Figure 6.1 (b)), is plotted.

This means that the same transducer used on two different components made of the same material but with different thickness work at different operation points

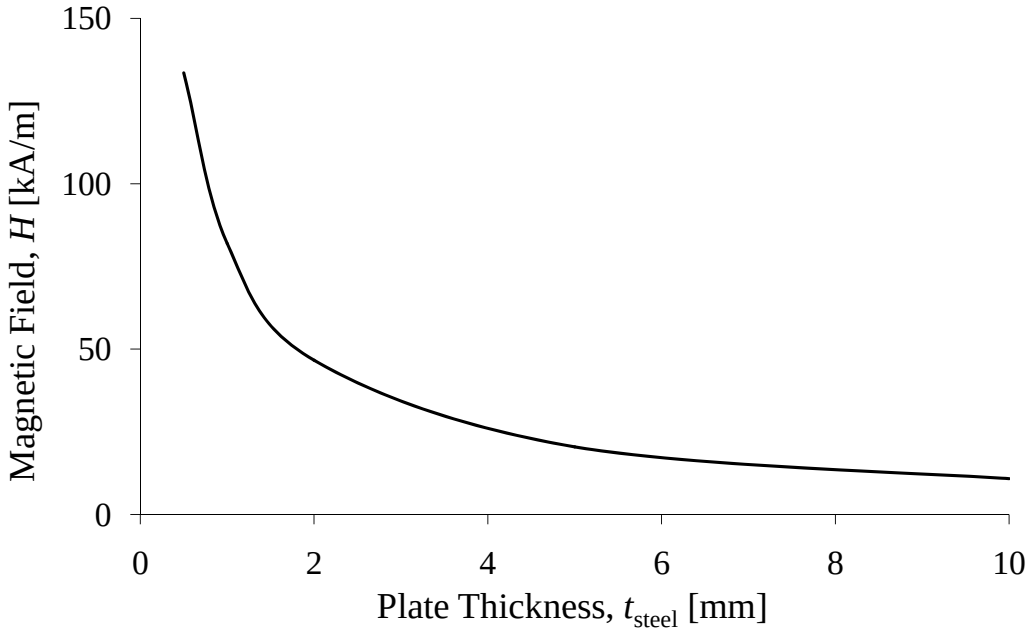

Figure 6.7: *FE simulation of the static magnetic field produced by a magnetostrictive EMAT at the surface of the steel plate, half way between the two magnets. The magnetic field component $\bar{H}_2$ parallel to the surface of a steel plate is plotted as a function of plate thickness.*

on the curve of Figure 6.3, giving dramatically different signal amplitudes. Also, different steel grades show different trends of the magnetostriction curve, for example the position of the zero in the curve (Figure 3.1) differs from material to material [11,91], and it has also been shown in Chapter 5 that the magnetic permeability profoundly alters the performance of the transducer. Magnetic permeability affects the amplitude of the dynamic magnetic field $\widetilde{H}_1$ [73] and its penetration depth (Equation (5.3)), thus significantly altering the resulting wave amplitude, since the wave amplitude is proportional to $\widetilde{H}_1$ according to Equation (4.8). This EMAT configuration performs badly on steel both in terms of signal amplitude and robustness, but when employed on a pure nickel plate (dashed line of Figure 6.3) the wave amplitude is considerably higher and relatively independent of the operation point. This is readily explained by the fact that nickel shows a higher magnetostriction (Figure 3.1) and lower permeability than steel (Figure 6.2), resulting in a signal amplitude more than an order of magnitude larger than that obtained in a mild

steel plate of the same thickness. The reduced dependency on the static bias field is a consequence of the fact that the magnetostriction curve of nickel is monotonic and does not show any zeros for $\bar{H} > 0$.

6.5.3 Magnetostrictive EMAT: bonded nickel strip

The favourable performance of magnetostrictive EMATs on nickel compared to steel suggests a modified configuration where a sheet of highly magnetostrictive material is bonded on the sample to be tested. Among the many possible solutions, here we consider a 0.5 mm thick nickel plate bonded to the steel plate, via a 200 μm thick epoxy layer. A schematic diagram is given in Figure 6.8, showing the top view (a) and the cross-section (b). In Figure 6.3 it is shown that this EMAT configuration achieves the best signal amplitude per unit driving current, and that the dependence on the bias magnetic field $\bar{H}$ is relatively small. It is important to evaluate the effects of the geometric and material properties of the bonded nickel plate on the overall performance of the transducer. The influence of the thickness and shear modulus of the adhesive layer, t_{epoxy} and G_{epoxy}, together with the thickness and width of the magnetostrictive layer, t_{ni} and W_{ni}, are to be assessed. The epoxy layer causes a discontinuity in the static magnetic circuit that decreases the magnetic field $\bar{H}$ that would be achieved with a continuous magnetic path. Simulations showed that this difference is relatively small: the percentage difference between the magnetic field with no gap and that with a 200 μm gap of epoxy is less than 20% for $\bar{H} > 20\,\mathrm{kA/m}$ (Figure 6.9). In this range, the sensitivity curve of this EMAT is relatively flat (Figure 6.3) so this effect only causes a small variation of the operation point resulting in only a small change in the generated amplitude. The dynamic magnetic field $\widetilde{H}$, is not affected by the thickness of the magnetostrictive layer as long as it is significantly larger than the magnetic skin depth, i.e. $t_{ni} > 3\delta$. Since the electromagnetic fields (static and dynamic) are not severely affected by the thickness of the adhesive and magnetostrictive layers, they can be considered to be practically decoupled from the parameters under investigation. For this reason, the magnetic fields were computed only once and then used as input to the mechanical model with different

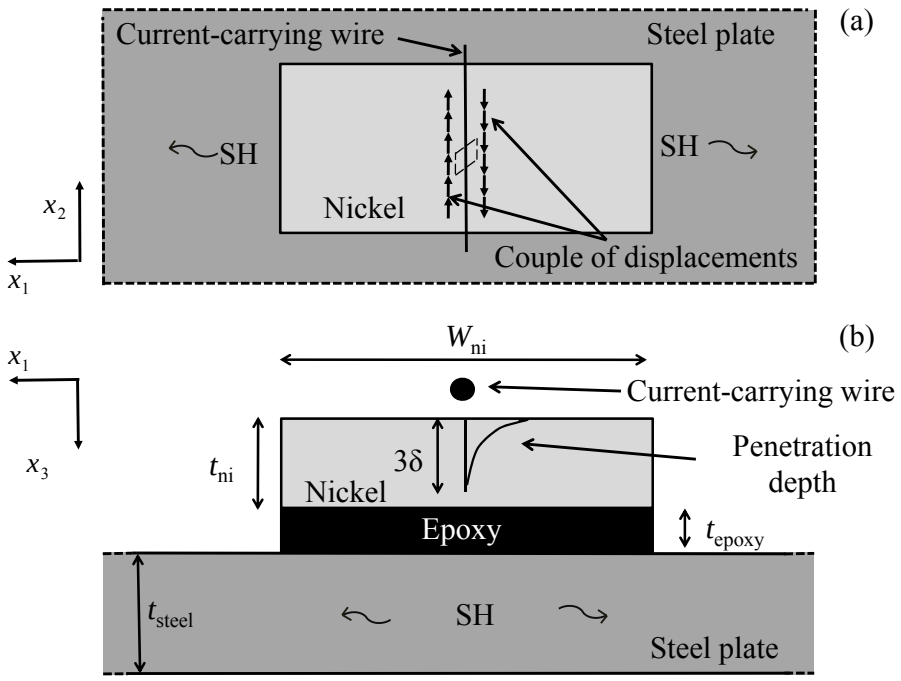

Figure 6.8: *Top view (x_1-x_2 plane) (a) and cross-section (x_1-x_3 plane) (b) of a magnetostrictive EMAT employing a bonded layer of nickel (light grey) to generate SH waves in a steel plate (dark grey). The current-carrying wire and the epoxy layer are also shown. In (a) a couple of distributed displacements, producing an ultrasonic field equivalent to that due to magnetostriction is displayed. In (b) the driving current produces a dynamic magnetic field along the x_1 direction exponentially decaying along the thickness of the magnetostrictive layer. Not to scale.*

values of the parameters under investigation. This simplification greatly reduces the computation time of the parametric study, avoiding the use of the demanding full magnetostrictive model at the cost of a slightly lower accuracy in the results. In contrast to the Lorentz force, whose mechanical effects are actually body forces on the sample, magnetostriction causes shear strains that have to be modelled as a dipole of displacements. Two equal and opposite displacements, separated by a distance of 4 millimeters, were prescribed along lines parallel to the wire on the mechanical model to reproduce the elastic field produced by a full magnetostrictive model (Figure 6.8 (a)). The wavelength at 150 kHz is $\lambda \cong 20$ mm, significantly larger than the dipole separation, so the resulting elastic field far from the trans-

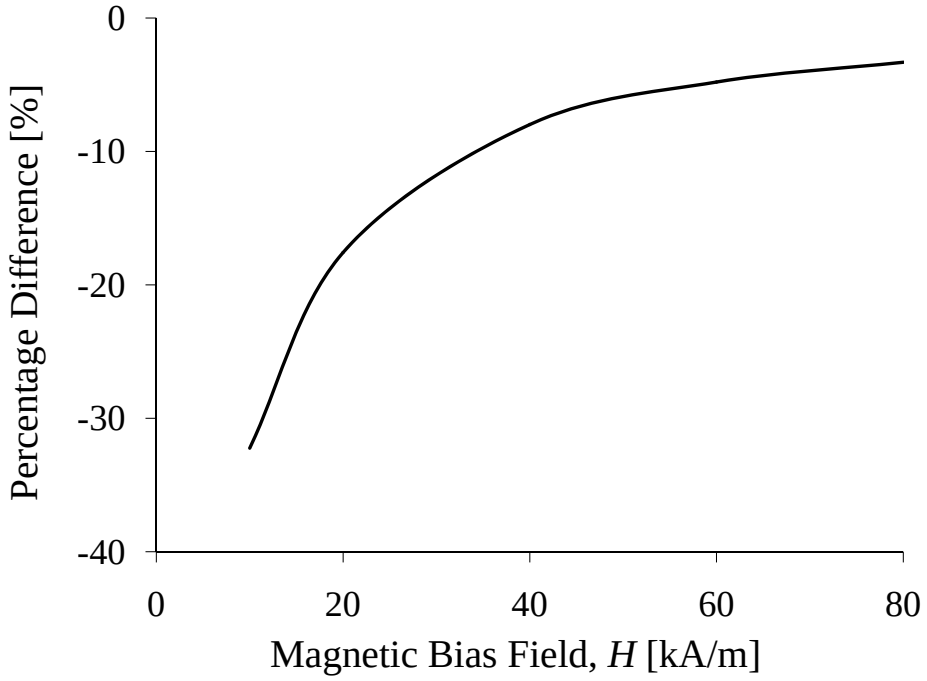

Figure 6.9: *Percentage difference between the bias magnetic field with no gap between the nickel strip and the steel plate ($t_{epoxy} = 0$) and the one with a* $200\,\mu$m *gap of epoxy. The bias field is computed on the surface of the nickel plate, half way between the two magnets.*

ducer is not affected by the dipole separation. The elastic properties for nickel and epoxy used in the model are summarized in Table 6.1. The magnetic permeability and magnetostriction curves of nickel are those used for the validation of the model presented in Chapter 5.

The adhesive layer acts as a spring placed between the nickel layer, where the transduction occurs, and the steel plate. FE simulations were performed on a 1 mm thick steel plate with a bonded 0.5 mm nickel plate, for different epoxy thicknesses and shear moduli, with the dipole-source model. Results (Figure 6.10) show that the wave amplitude is not altered for constant compliance of the bond $S_{bond} \propto (t_{epoxy}/G_{epoxy})$.

Moreover, given a certain shear modulus of the adhesive, the wave amplitude decreases with the thickness of the epoxy layer, t_{epoxy}, the reduction between the ideal case of a rigid bond with zero thickness and a $200\,\mu$m thick bond being about 30%.

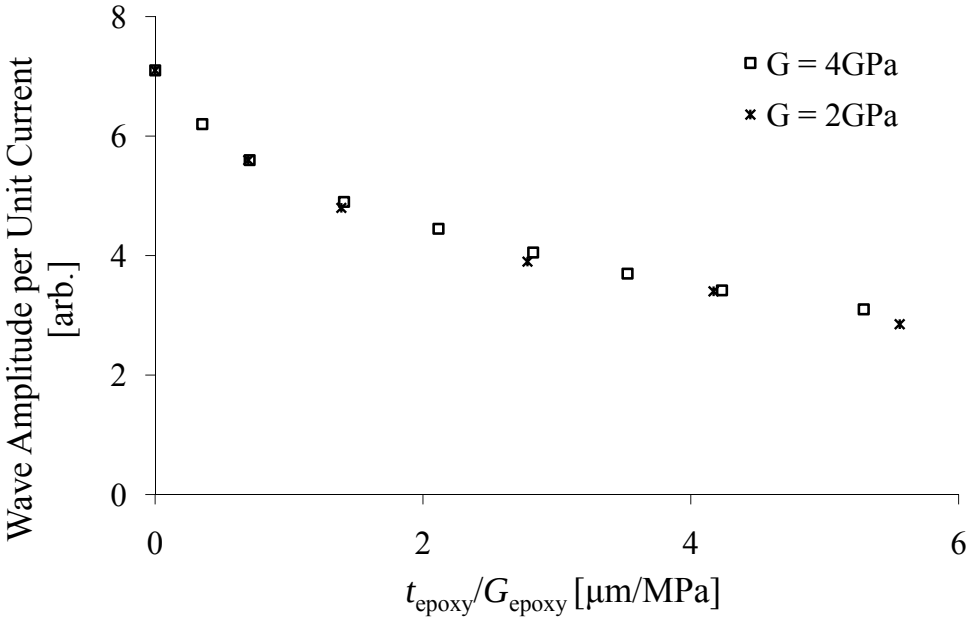

Figure 6.10: *Bonded nickel magnetostrictive EMAT: effect of the thickness and shear modulus of the epoxy layer on wave amplitude. Results from FE simulations on a* 1 mm *thick steel plate.*

The thickness of the magnetostrictive layer, t_{ni}, also influences the performance of the transducer. FE simulations (Figure 6.11) with the full magnetostrictive model on a 5 mm thick steel plate show that wave amplitude decreases with the thickness of the nickel layer, as long as the condition $t_{ni} > 3\delta$ is satisfied. This is due to the fact that the transduction occurs in a few skin depths; adding more material simply increases the overall thickness of the system, so reducing wave amplitude. On the other hand, if the magnetostrictive layer is too thin, for example less than a skin depth, the dynamic magnetic field $\widetilde{H}_1$ spreads in the steel plate which is much less magnetostrictive, and lower signal amplitudes are obtained. Therefore, the layer of magnetostrictive material should be thick enough to contain a few skin depths δ, but not significantly thicker than this.

The width (in the direction of propagation x_1) of the nickel strip, W_{ni} also affects the wave amplitude produced by this probe. The acoustic impedance of the free plate is different from the impedance in the area where the nickel strip is bonded on

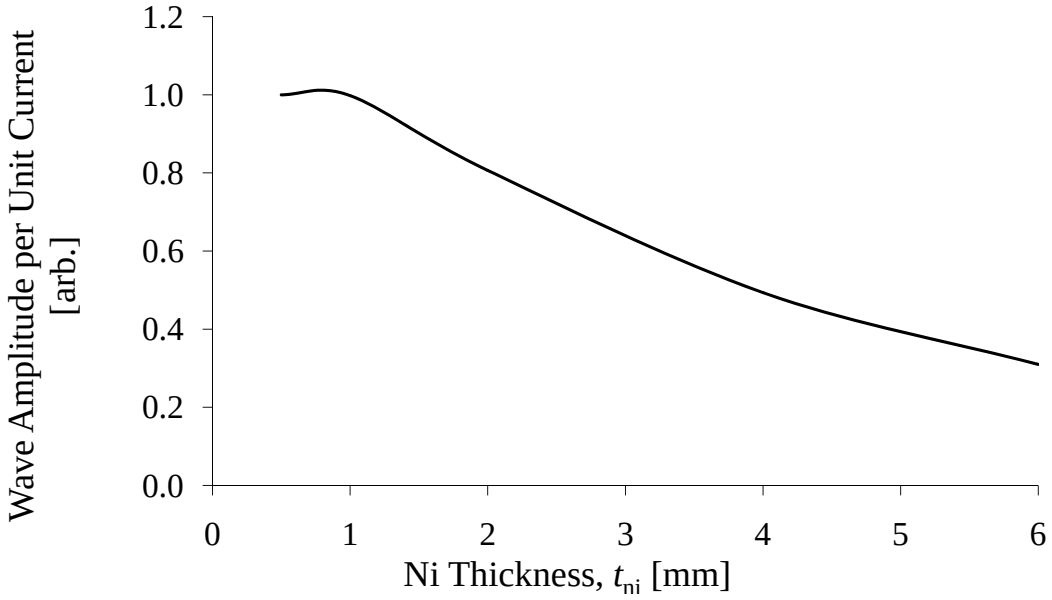

Figure 6.11: *Bonded nickel magnetostrictive EMAT: effect of the thickness of the nickel layer on the wave amplitude. FE simulation on a* 5 mm *thick steel plate,* 200 μm *epoxy bond.*

the plate. At the ends of the magnetostrictive layer, the impedance mismatch results in reverberations that produce interference phenomena. The system undergoes constructive interference when $W_{ni} = n\frac{\lambda}{2}$, where n is a positive integer number. Figure 6.12 shows FE simulations of this effect performed with the dipole-source elastic model. Resonances are observed only when n is odd, while minima are observed for even n. This is due to the fact that a dipole-like source cannot excite modes having a nodal line in the middle of the nickel layer, which correspond to even n. This resonant behaviour is really significant only when the thicknesses of nickel and steel are comparable, as in the experiment of Figure 6.3, where $t_{steel} = t_{ni} = 0.5\,\text{mm}$. In this case, the wave amplitude can vary by $\pm 50\%$ about the mean, depending on the ratio W_{ni}/λ. In practical applications, where the magnetostrictive layer is much thinner then the test object, the impedance mismatch is small and these interference phenomena are not significant. Figure 6.12 shows that while for $t_{steel} = t_{ni}$ there are large oscillations, for $t_{steel} = 6\,t_{ni}$ only small oscillations can be observed, thus confirming that the interference effect is seldom significant in actual tests.

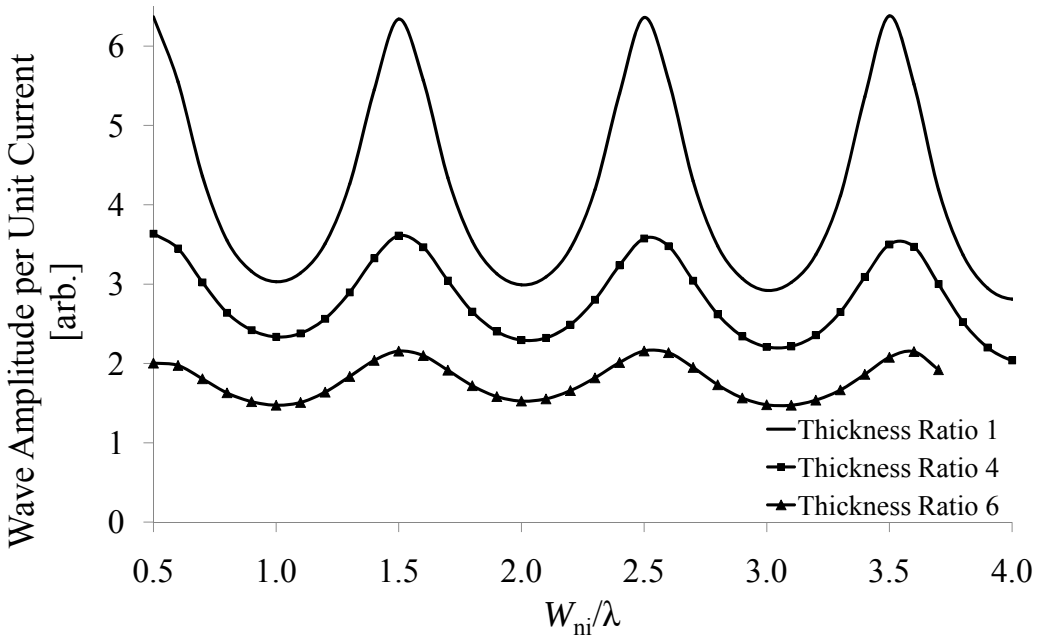

Figure 6.12: *FE simulations of the wave amplitude per unit current as a function of the width of nickel strip W_{ni}(measured as a multiple of the wavelength λ). Plots are reported for three different ratios of the thickness of steel over the thickness of nickel, t_{steel}/t_{ni}.*

6.6 Discussion

The results show that a magnetostrictive EMAT applied directly on a steel plate is not a good method for SH wave generation, not only because of the low wave amplitude obtained but even more because of the dependence of this transducer on the material and geometric properties of the testpiece. In contrast, the PPM EMAT is relatively insensitive to the precise composition and stress history of the plate to be inspected and gives better signal amplitudes than the magnetostrictive EMAT. Even better performance can be achieved by attaching a layer of highly magnetostrictive material to the sample. It has been shown that bonding a nickel layer can increase the particle velocity produced by more than a factor of five compared to that obtained with a PPM EMAT. In practice, materials significantly more magnetostrictive than nickel are available, for example iron-cobalt alloys show magnetostrictive strains twice as large as those of pure nickel, roughly doubling the resulting signal amplitude. Materials with significantly higher magnetostriction, such as Terfenol-D

or Metglas, are available and might be used to further increase the signal amplitude. The use of these materials makes bonded magnetostrictive EMATs the best probe in terms of wave amplitude. The main drawback of this configuration is that the transducer is no longer non-contact and the need for bonding significantly increases the time required to set the test up. Also, if for example a large pipe is to be tested, it can be difficult to produce a consistent bond over the required area.

It can be concluded that the choice between a PPM EMAT and a bonded magnetostrictive EMAT depends on the relative importance of signal amplitude and ease and reliability of test setup.

6.7 Conclusions

A number of different EMAT configurations able to generate horizontally polarized shear waves on a steel plate have been examined. Three basic types of EMATs have been addressed: Lorentz force PPM EMAT and magnetostrictive EMATs, used directly on the sample or with a bonded strip of highly magnetostrictive material on the plate. The performance of the probes has been assessed with the validated Finite Element model; the effect of relevant parameters on generated wave amplitude has been examined. The influence of geometric factors like the thicknesses of the plate, the magnetostrictive layer and the bond have been analyzed, as well as the effect of material properties like the magnetostrictive constants or the stiffness of the bond.

The analysis has shown that the magnetostrictive EMAT (without any extra magnetostrictive layer) generates low signal amplitude that is severely affected by the precise magneto-mechanical properties of the plate. On the other hand, this configuration can be dramatically improved by bonding a layer of highly magnetostrictive material between the transducer and the plate. In this case signal amplitudes an order of magnitude higher can be achieved, at the cost of the transducer becoming contact, rather than non-contact, and the extra preparation needed to provide an effective mechanical bond. Finally, a PPM EMAT produces intermediate amplitudes but is non-contact, easy to set up and is not sensitive to the different physical

properties seen across typical steels. The results of the study can be applied to analogous transducers producing torsional waves in pipe-like structures.

The next chapter will deal with another application of the FE model: the analysis of the performance of bulk shear wave EMATs on a range of different steel grades.

Chapter 7

Bulk shear wave EMAT performance on steels

7.1 Introduction

This chapter presents an experimental study of EMAT performance on a wide range of steel materials commonly used in engineering. Two EMAT configurations for bulk shear waves are examined. The experimental results are compared with simulations from the previously validated Finite Element model in order to obtain a physical interpretation of the data. An analysis of the relative importance of the transduction mechanisms is performed and practical conclusions are drawn.

7.2 Bulk wave EMATs on steel materials

A wide range of different kinds of steel materials, with different physical properties is employed in modern engineering. It has been reported that EMAT performance depends significantly on the material properties of the inspected sample. The variation of EMAT performance with material properties represents a major concern for practical applications, since it raises the question whether the same EMAT probe

can be successfully used to inspect different kinds of steel, or if transducers optimized for each steel grade have to be developed.

When employed on ferromagnetic materials such as steel, EMATs exploit mainly two different types of transduction mechanisms: the Lorentz force and magnetostriction. While the Lorentz force mechanism is linear and relatively insensitive to material properties such as electric conductivity σ and relative magnetic permeability μ_r, magnetostriction is highly non-linear, depends significantly on the physical properties of the sample and is a function of the applied magnetic field, stress state and magneto-mechanical loading history [11]. For this reason, it is fundamental to determine which transduction mechanism dominates for a given EMAT configuration as it affects the behaviour of the transducer when used on materials with different properties. Previous research has established that magnetostriction is the leading phenomenon in those EMAT configurations where the bias field is parallel to the surface of the sample [6]. However, when the static field is normal to the sample, some authors state that the Lorentz force dominates [6, 38, 39], while others [7, 21] claim that magnetostriction is the major effect for most practical cases.

The following sections will address the issues of the performance variation on different steel grades and the relative importance of the transduction mechanisms.

7.3 The experimental study

The steel grades under investigation are among the most commonly used in modern engineering, ranging from mild steel to tool and alloy steel, and including pipe steel and an austenitic steel, AISI 304 (with permeability and magnetostriction much less than 10% of those of a typical steel, as this is the maximum volume fraction of martensitic phase that can be present). The materials tested are listed in Table 7.1. All the samples have the same dimensions: $70 \times 30 \times 4\,\text{mm}$. The physical parameters influencing EMAT operation have been measured using the techniques described in the following sections.

Table 7.1: *List of the steel samples under investigation.*

Designation	C%	Other Elements %	Notes
EN8	0.32–0.40	0.80 Mn	Mild Steel
EN16	0.30–0.40	1.50 Mn, 0.25 Mo	Hardenable
EN24	0.30–0.40	0.60 Mn, 0.25 Mo, 1.50 Ni, 1.20 Cr	Hardenable
EN36	0.10	0.50 Mn, 3.50 Ni, 0.90 Cr	Hardenable
EN3	0.16–0.24	0.70 Mn	Mild Steel
EN32B	0.13–0.18	0.80 Mn	Mild Steel
BO1	0.90–1.00	1.20 Mn, 0.50 Cr, 0.50 W, 0.22 V	Tool Steel
AISI 304	0.08	9.00 Ni, 19.00 Cr	Austenitic
L80[a]	0.25–0.30	1.40 Mn, 0.12 Cu, Mo, Cr, Ti	Pipe Steel
L80[b]	0.25–0.30	1.40 Mn, 0.12 Cu, Mo, Cr, Ti	Pipe Steel
L80SS	0.25–0.30	Mo, Cr, Ti	Pipe Steel
TN80cr3	0.25–0.30	Mo, Cr, Ti	Pipe Steel
J55	0.40–0.50	1.00Mn, 0.17 Cr, 0.09 Cu Mo, Ni	Pipe Steel
CS70	0.65–0.75	0.70 Mn	Pipe Steel

7.3.1 Conductivity and permeability measurement

The electrical conductivity σ and the relative magnetic permeability μ_r of each sample were measured with the alternating current potential drop (ACPD) technique [92,93]. A pair of electrodes injects an alternating current in the testpiece and a second pair of electrodes measures the resulting potential drop; the real component of the impedance can then be computed as the real part of the ratio between the potential difference and the current [93]. The real component of the impedance varies with frequency due to the electromagnetic skin depth effect; once the geometric configuration of the probe and the thickness of the sample are known, analytical solutions [94] can be employed to compute the couple $\{\sigma, \mu_r\}$ that minimizes the root mean square error between theoretical and experimental data. The real component of the impedance of each sample was measured in the frequency range between 2 and 400 Hz and a two-variable fit with the analytical formula was performed to

deduce the electromagnetic properties (Table 7.2). The measured conductivity of the ferritic steels falls within the range $\sigma \in [2.5, 4.5]$ MS/m while the conductivity of austenitic AISI 304 is 1.39 MS/m. The measured permeabilities for the ferritic steel samples were between 50 and 140, while AISI 304, being non-ferromagnetic, has approximately unit relative permeability.

The magnetic permeability was also measured with a Fischer Technology Feritscope MP30E-S. This instrument measures an engineering parameter, the equivalent ferrite content, from which permeability can be estimated using an approximated relationship found in the literature [95]. While ACPD employs low-intensity currents, in the order of a few milliamperes, the Feritscope induces much larger currents in the sample. The EMATs used in the experimental study were driven by an approximately 10 A peak to peak pulse, and the currents used by the Feritscope are closer to the actual experimental conditions than the ACPD ones, however, this instrument gives much less accurate values, reported in Table 7.2.

7.3.2 Magnetostriction measurement

The magnetostriction curves of four steel grades (EN3, EN24, EN32B, BO1) were measured in order to determine the components of the magnetostriction coupling matrix d. In each measurement, a small sample ($30 \times 20 \times 1$ mm) was placed in the air gap of a magnetic circuit. The bias magnetic field was changed by adjusting the driving dc current fed to the electromagnets and the resulting strain was measured with strain gauges in full bridge configuration, using the same method described in Section 5.5. The resulting magnetostriction curves, shown in Figure 7.1, are consistent with data available in the literature [11, 12, 21, 33]. For comparison, the magnetostriction curve of industrially pure (99.0%) nickel is also shown, as measured in Section 5.5. In the steel samples the application of a magnetic field initially causes a positive strain (i.e. an expansion) along the direction of the field. The deformation reaches a maximum for $H < 20$ kA/m and turns into a compressional strain for higher bias fields. Even though the shapes of the four curves are similar, the position and magnitude of the maxima differ significantly for each grade because

Table 7.2: *Measured electromagnetic properties. Relative magnetic permeability was estimated via ACPD technique and a Feritscope instrument. The electric conductivity was measured with ACPD. The average standard deviation for the conductivity is* 0.1 MS/m*, while for the permeability the standard deviation of the ferromagnetic steels is* 1 *when measured with ACPD and* 5 *with the Feritscope instrument. The individual standard deviations for each sample are given in Figures 7.3 and 7.4.*

Designation	σ [MS/m]	μ_r, ACPD	μ_r, Feritscope
EN8	4.12	92	170
EN16	3.71	52	110
EN24	3.80	65	132
EN36	3.03	99	142
EN3	4.47	128	166
EN32B	4.46	108	150
BO1	4.01	90	157
AISI 304	1.39	1	1
L80[a]	4.54	70	143
L80[b]	4.54	61	139
L80SS	4.19	67	126
TN80cr3	2.61	86	167
J55	4.06	137	164
CS70	3.77	59	100

of the presence of alloy elements and due to thermal treatments. Conversely, nickel shows a monotonic contraction whose amplitude is significantly larger than the strain observed in any steel.

7.3.3 EMAT wave amplitude measurement

Two commercial transducers (Sonemat Ltd.) have been used: a spiral coil EMAT and a linear racetrack coil EMAT. Both transducers generate shear waves, with ra-

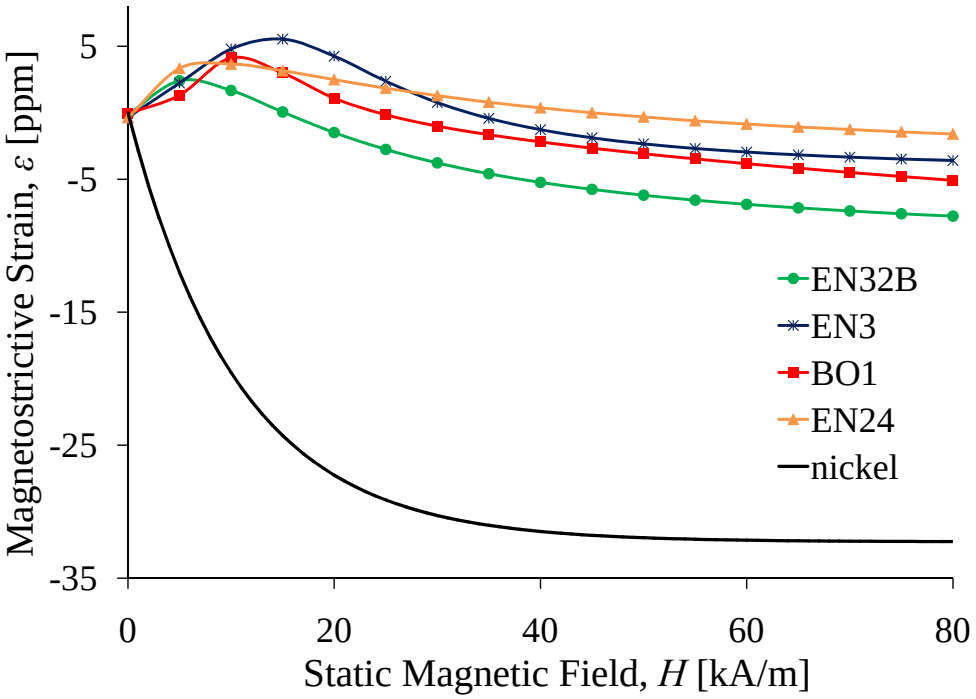

Figure 7.1: *Static magnetostriction curves of four steel grades and industrially pure nickel. Average standard deviation* 0.4 ppm.

dial and linear polarization respectively, propagating in the bulk of the material. The static magnetic field is normal to the surface of the sample and is due to a permanent magnet (NdFeB), while the coil generates eddy current and dynamic magnetic fields parallel to the surface of the sample. The transducers are driven by a broadband pulse, whose centre frequency is around 2.5 MHz. The result of a typical pulse-echo test using the linearly polarized EMAT is shown in Figure 7.2 (a): the ultrasonic pulse travels across the thickness of the sample and the reflections from its back-wall are received by the transducer. For each type of transducer, five acquisitions per steel sample were taken, each resulting from the average of 1000 time traces. The peak to peak amplitudes of the first seven reflections were measured and were fitted with an exponential function, in order to extrapolate the theoretical amplitude for zero time of flight (Figure 7.2 (b)). This is necessary in order to compensate both for diffraction effects and for the ultrasonic attenuation which is different for each kind of steel. Since the tests used the EMAT in pulse echo mode, the square root of the values obtained was taken in order to account for the generation mechanism only,

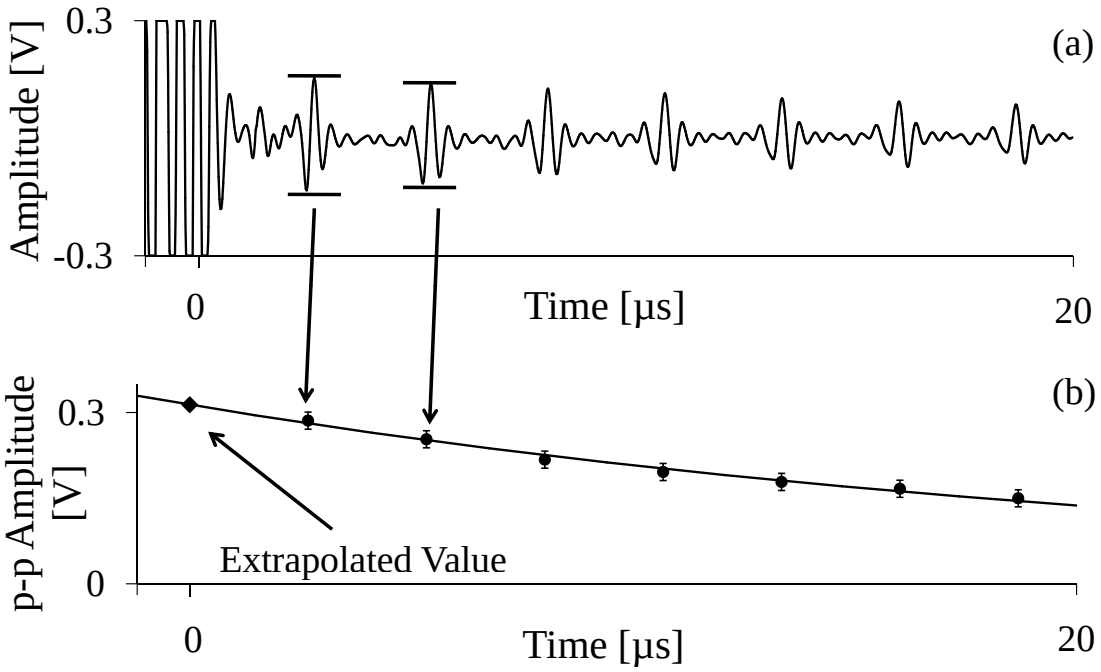

Figure 7.2: *(a) Signal received by an EMAT transducer in a pulse-echo test. The peak to peak amplitudes of the back-wall reflections have been interpolated via an exponential fit (b). It is then possible to estimate a theoretical attenuation-free amplitude for zero time of flight.*

on the assumption that reciprocity holds [13]. The experimental results are shown in Figures 7.3 and 7.4 for the linear coil transducer. The adjusted signal amplitudes are plotted against electric conductivity σ (Figure 7.3) and against magnetic permeability (measured with the ACPD technique [81]), μ_r (Figure 7.4). Error bars show the experimental standard deviations of the quantities under investigation for each steel grade. Analogous graphs were obtained from the spiral coil EMAT.

The data show that the signal amplitudes do not have a large scatter and are not obviously correlated with the electric conductivity and magnetic permeability. Even using the permeabilities values measured with the Feritscope there is no better correlation between EMAT amplitudes and permeabilities. The only exception is the case of austenitic steel whose lower amplitude is due to the fact that since this material is not ferromagnetic the magnetic flux density is significantly smaller than in the case of ferromagnetic steels. Indeed, measurements indicated that $\bar{B} = 410\,\mathrm{mT}$

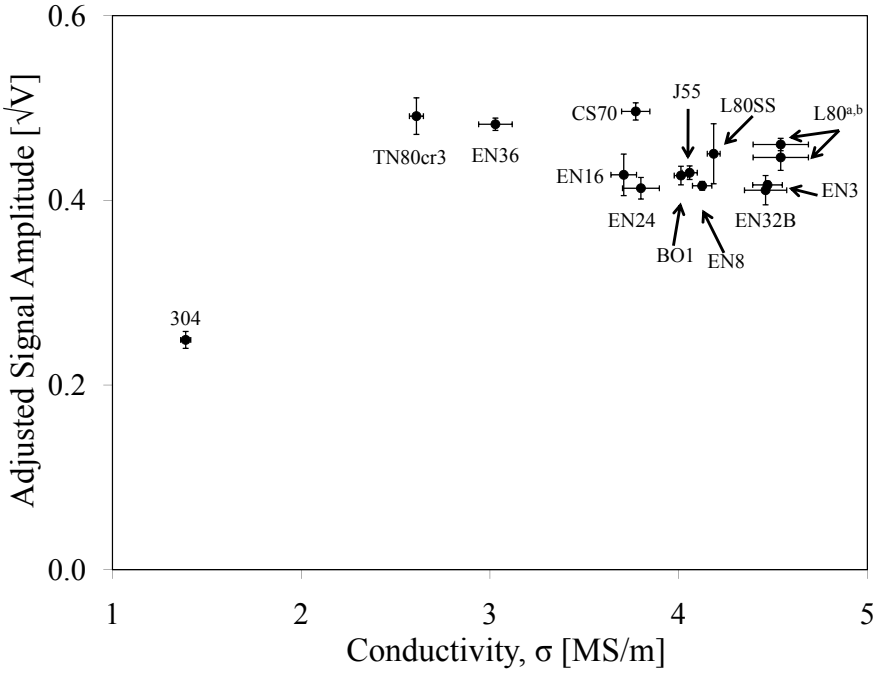

Figure 7.3: *Experimental EMAT amplitudes on different steels plotted against their electric conductivity. The amplitudes are attenuation compensated and square-rooted to account for the wave generation process only.*

for AISI 304, against $\bar{B} \cong 770\,\mathrm{mT}$ for all the other samples; this reduces the resulting amplitude by a factor of about 2, as the Lorentz force is linear in $\bar{B}$ (Equation (3.8)). If we compensate the amplitude of AISI 304 for this effect, all the experimental points have similar amplitudes. This strongly suggests that the transduction is mainly due to the Lorentz force, whose magnitude does not depend significantly on conductivity or permeability (in the limit $\delta/\lambda << 1$ [6]); if magnetostriction were dominant, a much larger scatter would be expected because of the observed differences in the magnetostriction curves of the various grades. In order to test this hypothesis and shed light on the experimental results, numerical simulations were carried out.

7.4 Finite Element simulations

The EMAT numerical model has been used to help understand the results of the experiments on the steel samples discussed above. The components of the magne-

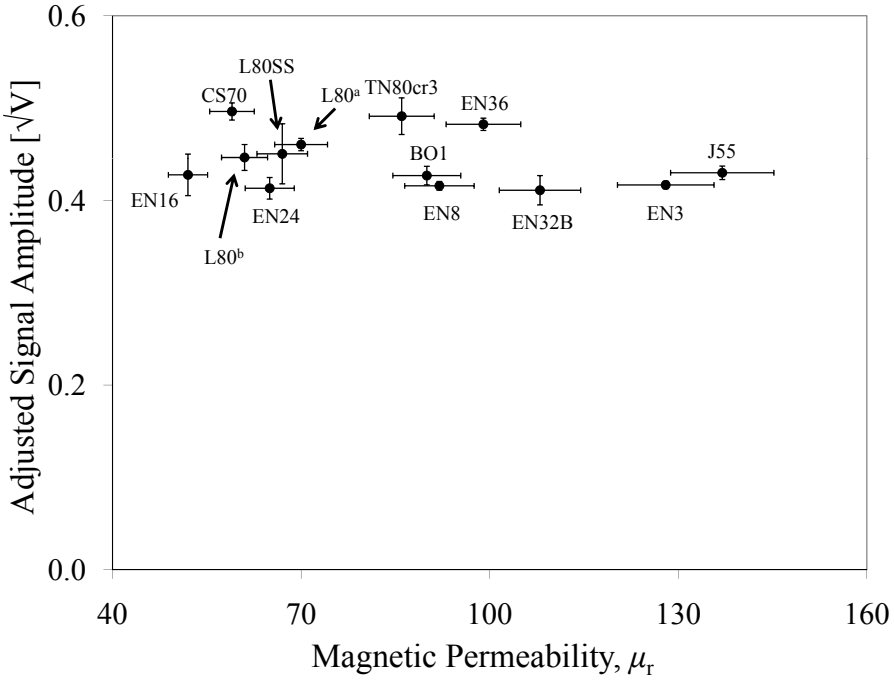

Figure 7.4: *Experimental EMAT amplitudes on different steels plotted against their magnetic permeability as measured with ACPD technique (AISI 304 not shown in this graph as $\mu_r = 1$). The amplitudes are attenuation compensated and square-rooted to account for the wave generation process only.*

tostriction coupling matrix d were determined from the experimental magnetostriction curves and Equations (3.25)-(3.26).

An axisymmetric two-dimensional model in a cylindrical reference system $\{r, z, \phi\}$ of an EMAT has been developed, as described in Section 4.6. The driving current in the coil is modelled as a zero cross-section current sheet, flowing in the circumferential direction above the metal, that induces eddy currents J_ϕ. These interact with the vertical component of the static flux density $\bar{B}_z$ producing a Lorentz body force $f_r = J_\phi \cdot \bar{B}_z$ in the radial direction that generates shear waves. Magnetostriction also contributes to the wave generation, according to Equation (4.11) , mainly due to shear strains $\widetilde{\epsilon}_{rz}$ produced by the radial component of the dynamic magnetic field, $\widetilde{H}_r$:

$$\widetilde{\epsilon}_{rz} \propto d_{15}\, \widetilde{H}_r, \tag{7.1}$$

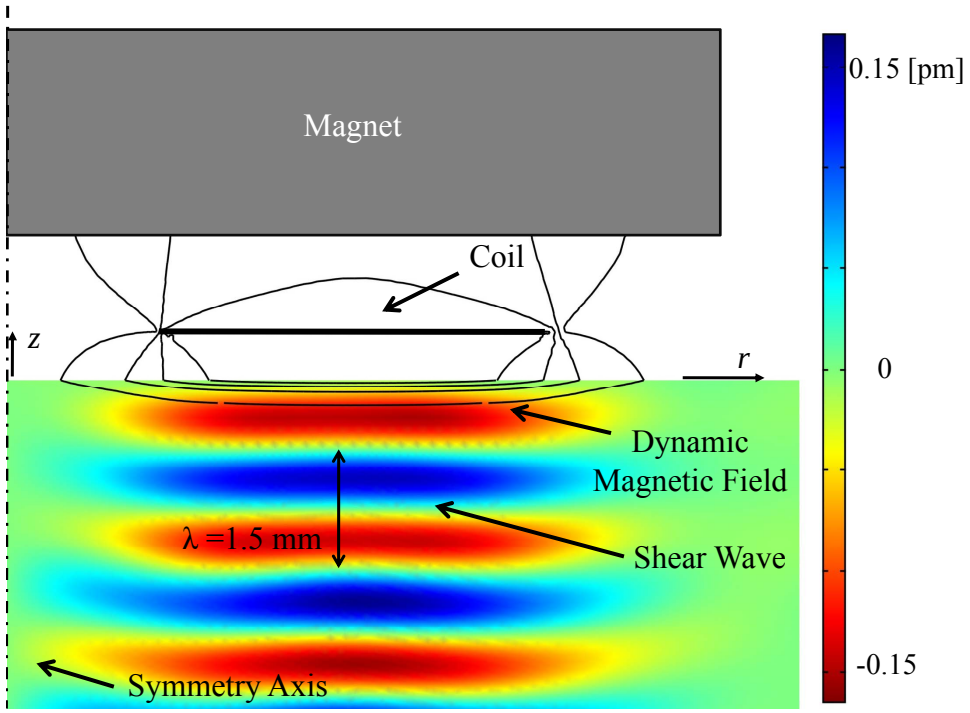

Figure 7.5: *Axisymmetric FE model of spiral coil EMAT. The displacement in the r direction generated by the transducer is represented by the colour plot. The amplitude of the radial component of the dynamic magnetic field produced by the coil is represented by the contour lines (Each line represents* 10 A/m *variations).*

where d_{15} is the magnetostrictive matrix component involved in shear wave generation, equivalent to d_{61} of Equation (3.26). The outer and inner diameters of the coil are 34 mm and 6 mm respectively; the distance between the coil and the sample (lift-off) is 0.6 mm. The coil is driven by a 1 A current oscillating at a frequency $f = 2$ MHz. The mesh consists of approximatively 150,000 triangular elements. The elastic properties used were the same for all the grades of steel and are those used in Chapter 6 (Table 6.1). Just below the coil, full magnetostrictive constitutive equations are employed to simulate the transduction process. For a depth larger than a few skin depths δ, i.e. $|z| > 4\delta$, the dynamic magnetic field becomes negligible and no transduction occurs. For this reason, purely elastic constitutive equations can be used to describe wave propagation, saving significant computational time. In order to simulate the operation on a half-space, an absorbing region with finite damping constant surrounds the elastic domain, to avoid back-reflections from the boundaries of the model. The result of a typical FE simulation is shown in Figure 7.5. The

displacement amplitudes produced separately by the Lorentz force and by magnetostriction were computed for four of the steel samples (EN3, EN24, EN32B, BO1). In turn solely the Lorentz force was applied, without any magnetostriction, and then the simulation was repeated with purely magnetostrictive effects and no Lorentz force, in order to evaluate the contribution of each mechanism. The magnetostriction and magnetic properties were obtained from the experiments discussed above. In order to test the hypothesis that the Lorentz force is the largest effect, the most favourable conditions for magnetostriction were assumed to assess its maximum contribution. The magnetic permeabilities used in the simulations were those measured via ACPD, which are lower than those estimated with the Feritscope. Lower permeabilities imply a larger skin depth as $\delta = (\pi f \sigma \mu)^{-1/2}$, that is, there is a larger region where a significant dynamic field $\widetilde{H}$ is present. In other words, this means that the surface over which Equation (7.1) has to be integrated is wider so the effect of magnetostriction is stronger. This effect has been presented in Chapter 5, where it was shown that with low permeability (due to high bias fields) magnetostriction generation is higher than it would be expected by assuming a direct proportionality to the relevant magnetostriction constant, $d_{61}(\bar{H})$ (Figure 5.8).

Moreover, the magnetic bias field in the material, $\bar{H}$, which determines the operation point cannot be estimated without a degree of uncertainty. This is a consequence of the fact that at the boundary between two media the perpendicular component of $\mathbf{B}$ (in our case $\bar{B}_z$) is continuous, while the perpendicular component of $\mathbf{H}$ is discontinuous. In other words, we know accurately the value of $\bar{B}_z$ from experimental data, but we can only estimate $\bar{H}_z$ using FE models. For the case under study it was found that $\bar{H}_z \in [6, 15]$ kA/m. The maximum values of the magnetostriction constant d_{15} falling in this range were considered to assess the largest possible impact of magnetostriction on wave generation. For the Lorentz force computations the static bias field $\bar{B}_z$ was assumed to be the same for all the samples and was set to the experimental value: $\bar{B}_z = 770\,\mathrm{mT}$. Remembering that the values for magnetostriction are to be considered an upper limit, the simulations indicate that for the investigated steels, the Lorentz force is the main transduction mechanism and that the contribution of magnetostriction is never larger than $\approx 30\%$ of the

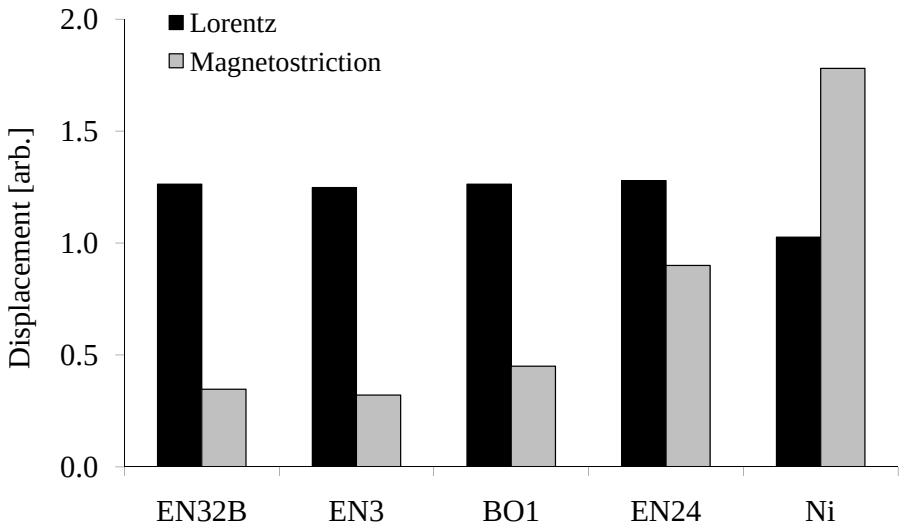

Figure 7.6: *Simulated displacements caused by the Lorentz force and magnetostriction in four steel grades and nickel. The amplitudes are not necessarily in phase and the values for magnetostriction represent an upper limit. The same unit driving current oscillating at* 2 MHz *was used for all the simulations.*

Lorentz force for three samples, and reaches $\approx 70\%$ for EN24 (Figure 7.6). For comparison, the simulations were also performed on nickel. The material properties used are listed in Table 6.1, and assuming the most favourable operation point for magnetostriction on nickel, i.e. 20 kA/m, the relative permeability is $\mu_r = 24$, and the magnetostriction constant $d_{15} = 4.09\,\mathrm{nm/A}$. This is the operation point where the balance between the magnitude of d_{15} and the amplitude and penetration depth of the dynamic magnetic field gives the maximum sensitivity for nickel, as shown in Figure 5.8. It has also to be noted that the bias magnetic flux density in nickel is $\bar{B} = 600\,\mathrm{mT}$ due to magnetic saturation. Nickel is significantly more magnetostrictive than steel, thus in this case magnetostriction is the larger effect, the resulting displacement being 1.7 times the one due to the Lorentz force mechanisms. These results are summarized in Table 7.3.

The predictions made for magnetostriction are essentially an upper limit; not only

Table 7.3: *Maximum magnetostriction constant d_{15} of four steel samples in the range $\bar{H}_z \in [6, 15]$ kA/m. The corresponding EMAT signal amplitudes (experimental), for the wave generation process only, are also shown. The last column displays the percentage ratio of the displacement caused by magnetostriction against the one due to the Lorentz force as predicted by the FE model for $f = 2$ MHz. Data on nickel are also shown for reference.*

Material	d_{15} [nm/A]	Exp.Amp [$\sqrt{\text{V}}$]	MS/LOR
EN32B	1.30	0.411	27.5%
EN3	1.44	0.417	25.7%
BO1	1.23	0.427	35.6%
EN24	1.71	0.413	70.4%
Nickel	4.09	–	173.5%

have we considered the maximum magnetostriction constant for a given steel and the lowest measured permeability, it has also been implicitly assumed that magnetostriction constants are frequency independent. The magnetostriction curve of each material was measured in dc conditions, applying a static bias field and the resulting magnetostriction constants were used for ac simulations. This assumption was made simply because assessing the frequency dependency of magnetostriction is a very complex experimental task, and in the literature there is a lack of dynamic magnetostriction properties. However, it is likely that when a dynamic magnetic field oscillating at frequencies in the order of hundreds of kilohertz is applied to a ferromagnetic material, not all the magnetic domains are able to follow the driving input, resulting in a reduction of the magnetostriction coefficients. This hypothesis is strongly supported by the fact that magnetic permeability significantly decreases with frequency [79, 81]; since permeability and magnetostriction are macroscopic effects caused by the same microscopic structures, i.e. magnetic domains, it is likely that the value of d_{15} used in our computation is overestimated. This is experimentally hinted at by the fact that there is no correlation between the magnetostriction constants measured and the EMAT wave amplitudes (Table 7.3).

7.5 Discussion

The numerical and experimental results lead to the conclusion that the Lorentz force mechanism is the largest in steel, while magnetostriction plays a less significant role. This conclusion can be interpreted via the physics of the two transduction mechanisms. As long as the eddy current penetration depth is much smaller than the acoustic wavelength, it is found by integrating Equation (3.8) that the total Lorentz force is proportional to the total induced current: $F_L \propto \bar{B} \int JdA$, whereas the total magnetostrictive force is proportional to the integral of the dynamic magnetic field: $F_{MS} \propto d_{15} \int \widetilde{H} dA$. By using an electromagnetic FE model, or analytical solutions [73], we can compute the dependencies of these quantities on electrical conductivity and magnetic permeability. The results are shown in Figure 7.7, normalized on the $y-$axis in order to show the relative variations of the integrals with the electromagnetic properties. Within the condition $\delta/\lambda << 1$, the Lorentz force is not very sensitive to changes in σ and μ_r because highly conductive materials show a shielding effect: the eddy currents tend to equal and mirror the driving current, regardless of their spatial distribution which is governed by conductivity and permeability [6, 12]. For this reason, the total eddy current, and thus the Lorentz force, is relatively insensitive to conductivity and permeability changes in highly conductive materials. On the other hand, magnetostriction is highly affected by σ and μ_r because not only does the distribution of the dynamic magnetic field $\widetilde{H}$ along the depth of the material change, but also its amplitude. This means that the integral of the magnetic field, and thus magnetostriction, is strongly affected by the electromagnetic properties of the material. The overall conclusion is that if the Lorentz force mechanism is dominant, a small variation of signal amplitudes with conductivity and permeability is to be expected, while if magnetostriction is the main transduction mechanism, large variations in the amplitudes should be observed. The relatively small variation of signal amplitudes in the experimental data supports the argument that Lorentz force is the largest transduction mechanism for this EMAT configuration [6, 38, 39], in agreement with FE predictions. A purely Lorentz force mechanism would give virtually no variation with σ and μ_r; how-

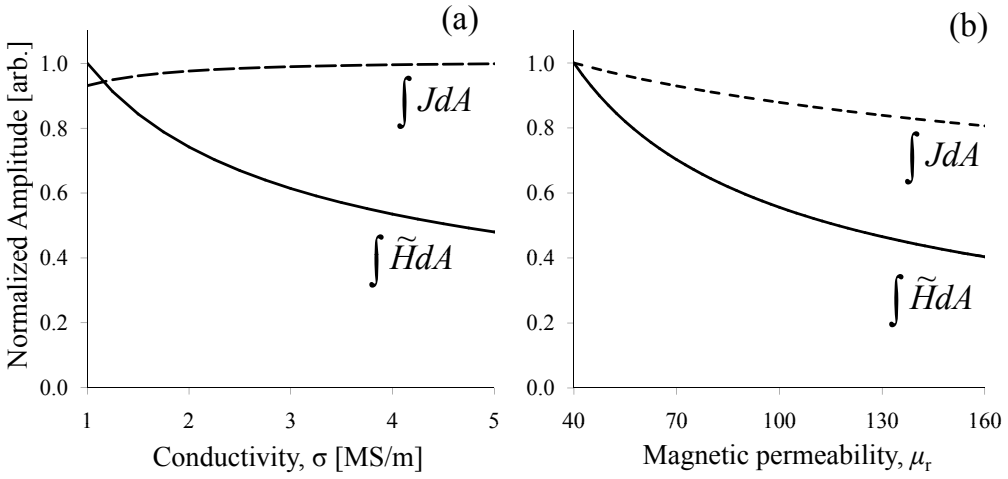

Figure 7.7: *Total induced current ($\int JdA$, dashed line) and total dynamic magnetic field ($\int \widetilde{H}dA$, continuous line) plotted against (a) electric conductivity and (b) magnetic permeability. Since the Lorentz force is proportional to the total induced current and magnetostriction is proportional to the total dynamic magnetic field, these plots show the dependence of the two transduction mechanisms on material properties. The values on the $y-$axis are normalized to show the relative variations with σ and μ_r.*

ever, there is some scatter in the experimental data. This is mainly due to the contribution of magnetostriction, together with experimental uncertainties in the measurement of magnetic flux density $\bar{B}$ and of the driving current I which were quantified to ±3-6% uncertainty of the signal amplitudes. From a practical point of view, since the measured amplitudes on different kinds of steel are similar, it is possible to use the same EMAT probe on a wide range of grades. Large amplitude variations have been observed in the field while inspecting steel components. Such variations are probably due to the presence of highly magnetostrictive oxide layers. In those cases, magnetostriction plays an important role in the transduction, as in the case of nickel, and the signal level is significantly increased. It can be concluded that normal bias field EMATs do not show large variations in the performance when operating on steel with a range of different material properties, except when a highly magnetostrictive oxide layer is present.

7.6 Conclusions

Previous research on EMATs had suggested that when the magnetic bias field is parallel to the surface of the sample, magnetostriction is the dominant transduction mechanism, while when it is normal to the surface, diverging conclusions had been drawn. The experimental tests on normal bias field EMATs, supported by numerical simulations, discussed in this chapter have shown that the Lorentz force mechanism is the largest transduction phenomenon on steel materials, regardless of the level of magnetic bias field employed, while the Lorentz force and magnetostriction are of the same order in nickel. It has been disproved that the magnetostrictive contribution is order of magnitudes larger than the Lorentz force contribution for EMAT generated ultrasound on steels, as previously claimed [7, 21]. This is also supported by the identification of a possible flaw in the previous analysis, as shown in Appendix A. It has also been shown that, unlike magnetostriction, the Lorentz force is relatively insensitive to the range of material properties of steels. This implies that using the same EMAT probe on various grades is possible and yields similar performance. However, signals will increase when a highly magnetostrictive oxide is present so magnetostriction becomes significant, while the performance on austenitic steels is poorer than ferritic steels because of the reduced bias magnetic field.

Chapter 8

Conclusions

8.1 Thesis review

In this thesis the operation of Electromagnetic Acoustic Transducers has been investigated through the development of a numerical model. A review of the work in literature, described in Chapter 2, showed that a large number of studies had been carried out on EMAT modelling, but most of them focused only on one transduction mechanism, the Lorentz force mechanism, while the other major phenomenon, magnetostriction, was included only in ideal analytical models or in non-validated numerical models. On the other hand, many studies had pointed out that magnetostriction plays a fundamental role in signal generation and detection in some EMATs configurations when employed on ferromagnetic media, which include materials extensively used in modern engineering such as ferrous and nickel alloys.

This led to development of a numerical multiphysics model, implemented in a commercial Finite Element software, that can be used as a prediction tool for arbitrary EMAT configurations when employed on ferromagnetic materials. The theoretical basis of the model was described in Chapter 3, where the relevant equations for all the transduction mechanisms involved in the generation and reception processes were presented.

The actual implementation of the governing equations in a commercial FE package was depicted in Chapter 4. The numerical methods employed by the software were introduced and a description of the absorbing regions, symmetries and meshes used was given, taking as an example a particular EMAT configuration. The use of a 2D simplified model and analytical solutions to reduce the computational burden of the model were also discussed.

The effectiveness of the numerical model was assessed by comparing its predictions with the results of experimental tests. A simple magnetostrictive EMAT generating shear horizontal waves in a nickel plate was taken as a benchmark. The wave amplitude variation as a function of the driving current amplitude, frequency and the static magnetic field was used to qualitatively validate the FE model. The absolute accuracy of the model was evaluated by comparing first principle predictions, i.e. obtained without the use of any arbitrary parameter, against experimental data. The validation of the model and the physical insight provided during the process was the subject of Chapter 5.

The usefulness of the validated model was demonstrated in its application to two practical issues: the comparison of different EMAT solutions to generate horizontally polarized shear waves in plates (Chapter 6) and the assessment of the performance of bulk wave EMATs on different steel grades (Chapter 7). The main SH wave EMAT configurations were analyzed, and the performance of their basic units were addressed in order to obtain a fair comparison between very different set-ups. Both the numerical model and experimental tests were employed to evaluate the sensitivity of the configurations in analogous conditions and the effect of key design parameters on the transduction. The model also proved to be useful in the physical interpretation of the experimental results obtained from the bulk wave EMATs on a large range of steel grades. In this way, the relative weight of the transduction mechanisms (the Lorentz force and magnetostriction) was determined with consequences on the applicability of EMATs on the range of steel grades commonly encountered in inspections.

8.2 Main findings of the thesis

8.2.1 EMAT magnetostriction model: development and validation

A comprehensive Finite Element model for EMATs was developed on commercial software. Simulations of the generation mechanism can be performed, accounting for the main transduction processes (i.e. the Lorentz force and magnetostriction). Magnetostriction was included using coupled constitutive equations that link the elastic field with the magnetic field. The model allowed the simulation of complex 3D configurations; as an example the generation of shear horizontal waves in a nickel plate due to an EMAT composed of a current-carrying wire parallel to a bias magnetic field has been successfully predicted.

Within the range of the strong bias field approximation, i.e. when the bias magnetic field is much larger than the dynamic one, it was experimentally observed that the generation sensitivity is linearly proportional to the dynamic magnetic field, which is determined by the driving current amplitude. This confirmed the validity of the strong bias approximation and the theory relying on it. The qualitative validation of the model showed that magnetostrictive EMAT sensitivity is not only a function of the magnetostriction constants, as the magnetic permeability plays a significant role in the transduction mechanism too: the penetration depth and the amplitude of the dynamic magnetic field are in fact determined by the magnetic permeability. This implies that magnetostrictive properties together with magnetic permeability have to be taken into account in the design of magnetostrictive EMATs. The wave amplitude per unit current predicted by the model, using measured material properties and without any arbitrary parameter was compared with experimental data. The discrepancy was smaller than 20 % over a 200 kHz frequency range, yielding a successful validation. Indeed, it was found that the difference between measured and numerically computed amplitudes was largely caused by the uncertainties in the magnetic properties and by their frequency dependence.

8.2.2 EMAT configurations for Shear Horizontal waves in steel plates

The performance of different EMAT configurations for shear horizontal waves on steel plates was compared. The EMAT types under investigation were the Periodic Permanent Magnet (PPM) EMAT (based on the Lorentz force mechanism) and purely magnetostrictive EMATs, with or without a bonded layer of highly magnetostrictive material on the testpiece.

The analysis showed that magnetostrictive EMATs directly applied on steel plates had comparatively poor performance in terms of wave amplitude generated, which was also strongly dependent on the precise magneto-mechanical properties of the plate. The PPM EMAT generated intermediate wave amplitude but with the advantage of being non-contact, simple to set up and insensitive to the variations in properties such as the magnetic permeability and electrical conductivity normally observed in ferromagnetic steels. Large signal amplitudes with relatively small dependence on the magnetic bias field were achieved with a magnetostrictive EMAT with a layer of highly magnetostrictive material bonded between the transducer and the plate. Numerical simulations highlighted that the wave amplitude of this EMAT configuration depends on the stiffness of the bond and that the thickness of the magnetostrictive layer has an optimal value related to the electromagnetic penetration depth. Also, the width of the magnetostrictive strip can affect the signal amplitude due to interference phenomena that build up when the thicknesses of the testpiece and the strip are similar. The main drawback of this configuration is that it compromised the non-contact nature of the transducer, increasing the complexity and preparation time required to perform inspections.

In practical applications the preference between a PPM EMAT and a bonded magnetostrictive EMAT reduces to a trade-off choice between the signal performance of the latter versus the ease of use and non-contact qualities of PPM EMATs.

8.2.3 Bulk shear Wave EMAT performance on different steel grades

While magnetostriction was already acknowledged to be the main transduction effect in EMAT configurations whose magnetic bias field is parallel to the surface of the sample, no clear conclusion had been reached on normal bias field configurations.

Experimental evidence indicated no obvious correlation between signal amplitude and physical properties of various steel samples, such as the electric conductivity and magnetic permeability. The numerical model helped the interpretation of these results by showing that a "shielding effect" makes the total induced eddy current roughly equal to the driving current that generates it, regardless of the material properties of the sample. This explained the fact that the Lorentz force is not very sensitive to conductivity and permeability. On the contrary, the amplitude and penetration depth of the dynamic magnetic field, upon which magnetostriction depends, is highly influenced by the electromagnetic properties of the sample. This diverging behaviour of the main transduction mechanisms hinted at an explanation of the experimental data in terms of a large Lorentz force effect, which was confirmed by FE simulation with the validated model. For a normal bias field EMAT, the Lorentz force is the major transduction effect on steels while on more magnetostrictive materials like nickel the two transduction mechanisms are of the same order of magnitude. Also, it has been proved that the previous theory according to which magnetostriction is 10 or 100 times larger than the Lorentz force on magnetic steel materials is not correct. This is further supported by the fact that a flaw in the published research was found, as explained in Appendix A. This implies that the use of a given EMAT probe on various grades of ferritic steel is possible and yields similar performance. Poor performance on austenitic steels are mostly due to the reduced bias magnetic field compared to ferritic steel while signal amplitude can significantly increase when highly magnetostrictive oxide cover the surface of the metal.

8.3 Suggestions for future work

The successful validation of the FE model carried out in Chapter 5 implies the substantial validity of the theoretical relations on which it is based. This is encouraging for further analytical work that might find exact solutions for some simplified EMAT cases of practical importance. For example an extension of the analytical model developed by Kawashima [10] for a pancake coil EMAT including magnetostriction would be very useful to rapidly design optimized transducers.

The quantitative validation also highlighted that the discrepancy between the predictions and the measurements is largely due to a lack in the knowledge of the material properties to input to the model. The magnetostriction coefficients were determined in static conditions, and then used to simulate dynamic conditions, with the unrealistic assumption that no frequency dependence arises. A characterization of magnetostriction behaviour in the frequency range used in EMATs applications, from a few kilohertz to tens of megahertz would be extremely useful to assess the accuracy of the FE model. Moreover, it was hypothesized that, at sufficiently high frequencies, the domain motion lags behind the magnetic field resulting in a reduced sensitivity for EMATs relying on magnetostriction. The measurements of dynamic magnetostriction parameters would test this theory, with practical implications for magnetostrictive EMAT design.

The models developed in Chapter 6 for SH wave EMATs are valid for plate inspection. The extension of these results to EMATs for pipe inspection is possible due to the similarities between the shear horizontal waves and torsional waves. It would be worth developing such models to increase the understanding of EMATs currently employed in the field and to optimize their operation.

Appendix A

A new analysis of the article "*Field dependence of coupling efficiency between electromagnetic field and ultrasonic bulk waves*" by H. Ogi

A.1 Introduction

In his paper, H. Ogi [21] studies the magnetic field dependence of bulk wave amplitudes generated by EMATs. His conclusion is that "*Both the measurement and the model analysis conclude that the magnetostrictive effect dominates the EMAT phenomena for the bulk waves in ferromagnetic metal, regardless of the bias field direction.(Page 3940)*[1]". However, this conclusion seems controversial compared to previous researches [6, 38] and to the results presented in Chapter 7. An analysis of Ogi's article will be presented here, showing the possible flaw that invalid his conclusions.

[1]We use italics font to refer to Ogi's original article.

A.2 EMAT configuration and reference system

Ogi employs a 2D model for a spiral elongated coil EMAT. The reference system is such that the x_1 axis is parallel to the surface of the metal while the x_3 axis is normal to it. The current flows in the x_2 direction and here we consider only the case of normal bias field, i.e. B_0 lies along the direction x_3. A bulk wave propagating in the thickness of the material, along x_3 has a longitudinal displacement u_3 and a transverse displacement u_1 (shear wave). These displacement components are due to the Lorentz force (L) and magnetostriction (MS) and the two contribution can be separated (*Equation (29) page 3946 in Ogi's paper, when the magnetization force is neglected*):

$$u_1 \doteq u_1^L + u_1^{MS} \tag{A.1}$$

$$u_3 \doteq u_3^L + u_3^{MS} \tag{A.2}$$

A.3 The experimental part

Ogi measured experimentally the field dependence of the amplitude of EMAT signals, which is reported in *Figure 5(a)* for the longitudinal and shear waves with normal bias field. He measured the signal amplitudes, A_1 (shear wave) and A_3 (longitudinal wave) which are the product of the generation amplitudes by the respective reception amplitudes. Assuming that reciprocity holds, we can write the total amplitude as proportional to the square of the displacement caused by the generation process, i.e. $A_i \propto u_i^2$, for $i = 1, 3$. On *page 3942* Ogi writes: "*Figure 5 presents the field dependences of their amplitudes. The amplitudes have been normalized by the maximum shear-wave amplitude in the normal bias field case.*". If we follow his notation, everything was normalized by the maximum of A_1. From *Figure 5(a)* we can then deduce the ratio between the longitudinal signal amplitude A_3 and the shear signal amplitude A_1:

$$A_3 = k^2 A_1 \qquad \text{From } \textit{Figure 5(a)}\text{, experimental.} \tag{A.3}$$

Assuming reciprocity and taking the square root, we can write Equation (A.3) in terms of the displacements:

$$u_3 = k u_1 \tag{A.4}$$

A.4 The theoretical part

Ogi's theoretical result for EMAT generation are presented in *Figure 8*, *page 3946*. On this page he states: "*Figure 8 shows the field dependence of the bulk-wave amplitudes due to the magnetostrictive effect normalized by the Lorentz force contribution for the longitudinal wave* (u_i^{MS}/u_3^L) *for each bias field.*". This time he is normalizing by u_3^L, which is the Lorentz contribution to the longitudinal wave and is much smaller than the shear component u_1, as can be deduced from *Figure 5(a)*. From *Figure 8* we can deduce the ratios between the magnetostrictive contributions, i.e. u_1^{MS} and u_3^{MS}, and u_3^L:

$$\frac{u_1^{MS}}{u_3^L} = \alpha \qquad \text{From } \textit{Figure 8}\text{, theoretical.} \tag{A.5}$$

$$\frac{u_3^{MS}}{u_3^L} = \frac{1}{\beta} \qquad \text{From } \textit{Figure 8}\text{, theoretical.} \tag{A.6}$$

A.5 The new normalization

In *Figure 5(a)* Ogi normalizes by the shear component u_1 while in *Figure 8* he normalizes by u_3^L, the longitudinal component due to Lorentz force, which is much smaller than u_1, as *Figure 5(a)* suggests. In order to obtain a fair comparison

between magnetostriction and the Lorentz force we want the ratios between u_1^{MS} and u_3^{MS} and the Lorentz shear component u_1^L, rather than the longitudinal one, u_3^L. This can be achieved as it follows. Using Equations (A.1),(A.2) and (A.4) we find:

$$u_3^L + u_3^{MS} = k\, u_1^L + k\, u_1^{MS} \tag{A.7}$$

Combining Equations (A.5) and (A.6) we have:

$$u_3^{MS} = \frac{1}{\alpha\beta}\, u_1^{MS} \tag{A.8}$$

Using Equations (A.5) and (A.8) in (A.7), with some algebra, we have:

$$\frac{u_1^{MS}}{u_1^L} = \frac{\alpha\beta k}{1+\beta-\alpha\beta k} \tag{A.9}$$

This expression compares the magnetostrictive contribution with the most significant Lorentz contribution u_1^L, using three factors, α, β and k, obtained by Ogi's graphs. It has to be noted that k is a function of the magnetic flux density B_0 while α and β are functions of the magnetic field H_0. These quantities are linked by the magnetic permeability $\mu_r = B/(\mu_0 H)$ which can be computed from *Figure 6(a), page 3943*, where a magnetization curve $M-H$ is shown. The new plot (Figure A.3, continuous line) shows that the magnetostrictive shear component u_1^{MS} is only 10^{-1} times the Lorentz shear component, u_1^L.

A.6 Conclusions

In his article Ogi states that "[...] *the magnetostriction mechanism governs the bulk-wave generation as a whole, regardless of the field direction.*" (*page 3946*). This seems to be the case when the bias field is parallel to the sample, as confirmed

by the researches of Wilbrand [38] and Thompson [6]. However, when the bias field is normal to the sample Wilbrand and Thompson found that magnetostriction has a negligible effect, in contrast with Ogi's article. Ogi seems to prove his conclusion in *Figure 8* where he compares the field dependence of magnetostrictive contributions against Lorentz contributions. The flaw probably lies in the fact that the chosen reference for Lorentz force is the longitudinal displacement, u_3^L which is significantly smaller than the shear contribution u_1^L. Since normal field EMATs are mainly used to generate shear waves, it makes sense to compare the shear contribution of magnetostriction and Lorentz effect, i.e. the ratio u_1^{MS}/u_1^L rather than u_1^{MS}/u_3^L as Ogi did. The ratio between the shear contributions has been deduced using Ogi's data and same simple algebraic manipulations. It has to be stressed that Ogi's results were assumed to be correct (both experimental and theoretical) and were simply re-plotted with a different normalization. The result shows a very different picture: Lorentz force contribution is larger than the magnetostrictive one, for any bias field (Figure A.3).

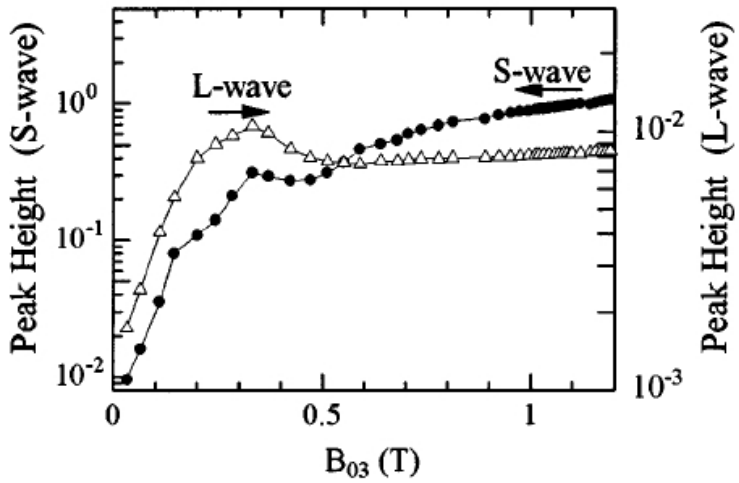

FIG. 5. Field dependences of the spectrum-peak height for the steel plate. Plotted are the response at the 4th resonant frequency for the longitudinal wave and the 8th one for the shear wave.

Figure A.1: *Figure 5(a) of Ogi's article [21].*

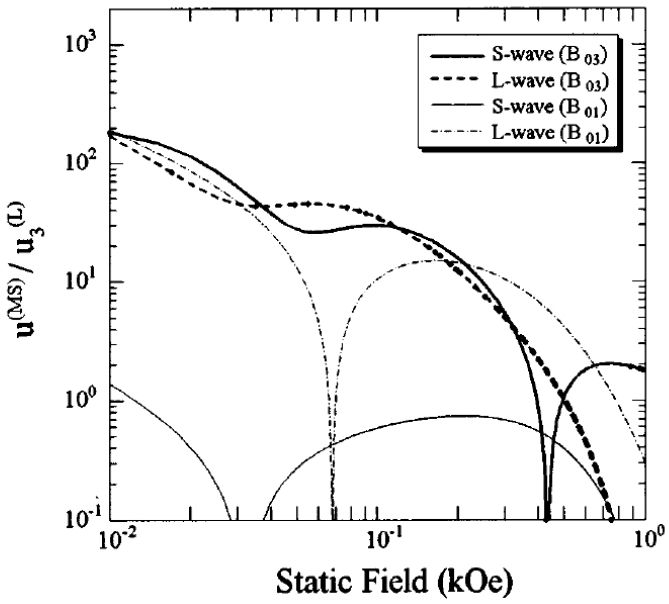

FIG. 8. Calculation of the field dependence of the generated bulk-wave amplitudes.

Figure A.2: *Figure 8 of Ogi's article [21].*

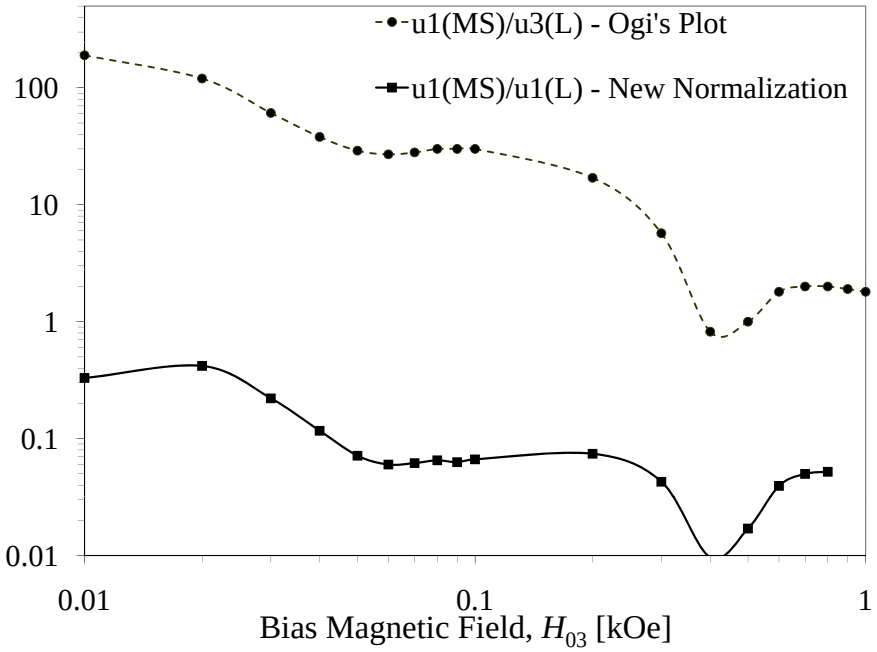

Figure A.3: *Figure 8 of Ogi's article re-plotted. The dashed curve is Ogi's original curve* u_1^{MS}/u_3^L *(indicated with S-wave* (B_{03}) *in the original graph). The solid curve show the ratio* u_1^{MS}/u_1^L *re-computed using Ogi's data.*

References

[1] G. L. Workman, D. (technical editors) Kishoni, and P. O. (editor) Moore. *Nondestructive Testing Handbook: Ultrasonic Testing*. American Society For Nondestructive Testing, Columbus, 2007.

[2] J. Szilard. *Ultrasonic testing: Non-conventional testing techniques*. John Wiley & Sons, Inc., New York, 1982.

[3] D. C. Jiles. *Introduction to the Principles of Materials Evaluation*. CRC Press, Boca Raton, 2008.

[4] L. W. Schmerr. *Fundamentals of Ultrasonic Nondestructive Evaluation: A Modeling Approach*. Plenum Press, Norwell, 1998.

[5] B. W. Maxfield and C. M. Fortunko. The design and use of electromagnetic acoustic wave transducers (emats). *Materials Evaluation*, 41:1399–1408, 1983.

[6] R. B. Thompson. Physical principles of measurements with emat transducers. In W. P. Mason and R. N. Thurston, editors, *Physical Acoustics*, volume XIX, pages 157–200. Academic Press, New York, 1990.

[7] M. Hirao and H. Ogi. *EMATs for science and industry: noncontacting ultrasonic measurements*. Kluwer Academic Publishers, Boston, 2003.

[8] E. R. Dobbs. Electromagnetic generation of ultrasonic waves. In W. P. Mason and R. N. Thurston, editors, *Physical Acoustics*, volume X, pages 127–189. Academic Press, New York, 1973.

[9] R. B. Thompson. A model for the electromagnetic generation and detection of rayleigh and lamb waves. *IEEE Transactions on Sonics and Ultrasonics*, SU-20(4):340–346, 1973.

[10] K. Kawashima. Theory and numerical calculation of the acoustic field produced in metal by an electromagnetic ultrasonic transducer. *The Journal of the Acoustical Society of America*, 60:1089–1099, 1976.

[11] R. M. Bozorth. *Ferromagnetism*. Van Nostrand, Princeton, 1951.

[12] D. C. Jiles. *Introduction to magnetism and magnetic materials*. Chapman and Hall, London, 1998.

[13] P. H. Rogers. *The electrical engineering handbook*. CRC Press, Boca Raton, 1997.

[14] P. Nagy. http://www.ase.uc.edu/ pnagy/classnotes/.

[15] R. B. Thompson, S. S. Lee, and J. F. Smith. Angular dependence of ultrasonic wave propagation in a stressed, orthorhombic continuum: theory and application to the measurement of stress and texture. *The Journal of the Acoustical Society of America*, 80(3):921–931, 1986.

[16] S. Dixon and M. D. G. Potter. Ultrasonic texture measurement of sheet metals: An integrated system combining lamb and shear wave techniques. *Nondestructive Testing and Evaluation*, 20(4):201–210, 2005.

[17] H. Kwun and C. M. Teller. Magnetostrictive generation and detection of longitudinal, torsional, and flexural waves in a steel rod. *The Journal of the Acoustical Society of America*, 96:1202–1204, 1994.

[18] M. G. Silk. *Ultrasonic transducers for nondestructive testing*. Adam Hilger, Accord, 1984.

[19] R. B. Thompson. A model for the electromagnetic generation of ultrasonic guided waves in ferromagnetic metal polycrystals. *IEEE Transactions on Sonics and Ultrasonics*, SU–25(1):7–15, 1978.

[20] I. V. Il'in and A. V Kharitonov. *Soviet Journal of Nondestructive Testing*, 16:549, 1980.

[21] H. Ogi. Field dependence of coupling efficiency between electromagnetic field and ultrasonic bulk waves. *Journal of Applied Physics*, 82:3940–3949, 1997.

[22] B. W. Maxfield, A. Kuramoto, and J. K. Hulbert. Evaluating emat designs for selected applications. *Materials Evaluation*, 45:1166–1183, 1987.

[23] S. Dixon, C. Edwards, and S.B. Palmer. High accuracy non-contact ultrasonic thickness gauging of aluminium sheet using electromagnetic acoustic transducers. *Ultrasonics*, 39(6):445 – 453, 2001.

[24] A. Hobbis and A. Aruleswarana. Non-contact thickness gauging of aluminium strip using emat technology. *Nondestructive Testing and Evaluation*, 20(4):211–220, 2005.

[25] C. F. Vasile and R. B. Thompson. Excitation of horizontally polarized shear elastic waves by electromagnetic transducers with periodic permanent magnets. *Journal of Applied Physics*, 50(4):2583–2588, 1979.

[26] R. B. Thompson. Generation of horizontally polarized shear waves in ferromagnetic materials using magnetostrictively coupled meander-coil electromagnetic transducers. *Applied Physics Letters*, 34:175–177, 1979.

[27] H. Ogi, E. Goda, and M. Hirao. Increase of efficiency of magnetostriction sh-wave electromagnetic acoustic transducer by angled bias field: Piezomagnetic theory and measurement. *Japanese Journal of Applied Physics*, 42:3020–3024, 2003.

[28] R. Murayama, S. Makiyama, M. Kodama, and Y. Taniguchi. Development of an ultrasonic inspection robot using an electromagnetic acoustic transducer for a lamb wave and an sh-plate wave. *Ultrasonics*, 42(1-9):825–829, 2004.

[29] J. C. Maxwell. *On Physical Lines of Force*, volume 21. 1861.

[30] J. P. Joule. On the effects of magnetism upon the dimensions of iron and steel bars. *Philosophical Magazine, Physics of Condensed Matter, Defects and Mechanical Properties*, 30(199):76, 1847.

[31] C. C. Grimes and S. J. Buchsbaum. Interaction between helicon waves and sound waves in potassium. *Physical Review Letters*, 12(13):357–360, 1964.

[32] M. R. Gaerttner, W. D. Wallace, and B. W. Maxfield. Experiments relating to the theory of magnetic direct generation of ultrasound in metals. *Physical Review B, Condensed Matter*, 184(3):702–704, 1969.

[33] R. B. Thompson. Mechanisms of electromagnetic generation and detection of ultrasonic lamb waves in iron-nickel alloy polycrystals. *Journal of Applied Physics*, 48(12):4942–4950, 1977.

[34] W. Mohr and P. Höeller. On inspection of thin-walled tubes for transverse and longitudinal flaws by guided ultrasonic waves. *IEEE Transactions on Sonics and Ultrasonics*, SU-23(5):369–374, 1976.

[35] C. V. Dodd and W. E Deeds. Analytical solutions to eddy-current probe-coil problems. *Journal of Applied Physics*, 39(5):2829–2838, 1968.

[36] G. F. Miller and H. Pursey. The field and radiation impedance of mechanical radiators on the free surface of a semi-infinite isotropic solid. *Proceedings of the Royal Society of London*, 223(1155):521–541, 1954.

[37] K. Kawashima. Quantitative calculation and measurement of longitudinal and transverse ultrasonic wave pulses in solid. *IEEE Transactions on Sonics and Ultrasonics*, 31(2):83–94, 1984.

[38] A. Wilbrand. Emus–probes for bulk waves and rayleigh waves. model for sound field and efficiency calculations. In P. Holler, editor, *New Procedures in Non-destructive Testing*, pages 71–82, Berlin, 1983. Springer.

[39] A. Wilbrand. Quantitative modeling and experimental analysis of the physical properties of electomagnetic–ultrasonic transducers. In D. Chimenti and

D. Thompson, editors, *Review of Progress in Quantitative Nondestructive Evaluation*, volume 7, pages 671–678, New York, 1987. Plenum.

[40] R. Ludwig, D. Moore, and W. Lord. A comparative study of analytical and numerical transient force excitations on an elastic half-space. *IEEE Transactions on Ultrasonics, Ferroelectrics and Frequency Control*, 36(3):342–350, 1989.

[41] R. Ludwig and X. W. Dai. Numerical and analytical modeling of pulsed eddy currents in a conducting half-space. *IEEE Transactions on Magnetics*, 26(1):299–307, 1990.

[42] R. Ludwig and X. W. Dai. Numerical simulation of electromagnetic acoustic transducer in the time domain. *Journal of Applied Physics*, 69:89–98, 1991.

[43] R. Ludwig. Numerical implementation and model predictions of a unified conservation law description of the electromagnetic acoustic transduction process. *IEEE Transactions on Ultrasonics, Ferroelectrics and Frequency Control*, 39(4):481–488, 1992.

[44] R. Ludwig. Theoretical basis for a unified conservation law description of the electromagnetic acoustic transduction process. *IEEE Transactions on Ultrasonics, Ferroelectrics and Frequency Control*, 39(4):476–480, 1992.

[45] R. Ludwig, Z. You, and R. Palanisamy. Numerical simulations of an electromagnetic acoustic transducer-receiver system for ndt applications. *IEEE Transactions on Magnetics*, 29(3):2081–2089, 1993.

[46] H. Kwun and K. A. Bartels. Experimental observation of elastic-wave dispersion in bounded solids of various configurations. *The Journal of the Acoustical Society of America*, 99:962–968, 1996.

[47] H. Kwun and K. A. Bartels. Magnetostrictive sensor technology and its applications. *Ultrasonics*, 36(1-5):171–178, 1998.

[48] R. Murayama. Driving mechanism on magnetostrictive type electromagnetic acoustic transducer for symmetrical vertical-mode lamb wave and for shear horizontal-mode plate wave. *Ultrasonics*, 34(7):729–736, 1996.

[49] R. Murayama. Study of driving mechanism on electromagnetic acoustic transducer for lamb wave using magnetostrictive effect and application in drawability evaluation of thin steel sheets. *Ultrasonics*, 37(1):31–38, 1999.

[50] X. Jian, S. Dixon, K. T. V. Grattan, and R. S. Edwards. A model for pulsed rayleigh wave and optimal emat design. *Sensors and Actuators: A Physical*, 128(2):296–304, 2006.

[51] S. Dixon and S. B. Palmer. Wideband low frequency generation and detection of lamb and rayleigh waves using electromagnetic acoustic transducers (emats). *Ultrasonics*, 42(10):1129–1136, 2004.

[52] X. Jian, S. Dixon, R. S. Edwards, and J. Reed. Coupling mechanism of electromagnetic acoustical transducers for ultrasonic generation. *The Journal of the Acoustical Society of America*, 119(5):2693–2701, 2006.

[53] S. Dixon and X. Jian. Eddy current generation enhancement using ferrite for electromagnetic acoustic transduction. *Applied Physics Letters*, 89(19):193503, 2006.

[54] X. Jian and S. Dixon. Enhancement of emat and eddy current using a ferrite back-plate. *Sensors and Actuators A: Physical*, 136(1):132–136, 2007.

[55] X. Jian, S. Dixon, and S. B. Palmer. In-plane and out-of-plane particle velocity measurement using electromagnetic acoustical transducers. *IEEE Ultrasonic Symposium*, pages 1276–1279, 2005.

[56] R. Jafari-Shapoorabadi, A. Konrad, and A. N. Sinclair. Improved finite element method for emat analysis and design. *IEEE Transactions on Magnetics*, 37(4):2821–2823, 2001.

[57] R. Jafari-Shapoorabadi, A. Konrad, and A. N. Sinclair. Comparison of three formulations for eddy-current and skin effect problems. *IEEE Transactions on Magnetics*, 38(2):617–620, 2002.

[58] R. Jafari-Shapoorabadi, A. Konrad, and A. N. Sinclair. The governing electrodynamic equations of electromagnetic acoustic transducers. *Journal of Applied Physics*, 97(10):10E102, 2005.

[59] K. Mirkhani, C. Chaggares, C. Masterson, M. Jastrzebski, T. Dusatko, A. Sinclair, R. Jafari-Shapoorabadi, A. Konrad, and M. Papini. Optimal design of emat transmitters. *NDT & E International*, 37(3):181–193, 2004.

[60] S S. (technical editor) Udpa and P. O. (editor) Moore. Non-destructive testing handbook: Electromagnetic testing. 2007.

[61] F. C. Moon. *Magneto Solid Mechanics*. John Wiley & Sons, Inc., New York, 1984.

[62] K. R. Whittington. Ultrasonic testing at high temperatures. *Physics in Technology*, 9(2):62–67, 1978.

[63] S. S. Lee and B. Y. Ahn. Emat application at high temperature. *Nondestructive Testing and Evaluation*, 7(1):253–261, 1992.

[64] E. W. Lee. Magnetostriction and magnetomechanical effects. *Reports on Progress in Physics*, 18(1):184–229, 1955.

[65] E. W. Lee. Magnetostriction curves of polycrystalline ferromagnetics. *Proceedings of the Physical Society*, 72(2):249–258, 1958.

[66] G. Engdahl. *Handbook of giant magnetostrictive materials*. Academic Press, San Diego, 2000.

[67] R. A. Toupin and B. Bernstein. Sound waves in deformed perfectly elastic materials. acoustoelastic effect. *The Journal of the Acoustical Society of America*, 33:216–225, 1961.

[68] Comsol multiphysics user's guide, 2008.

[69] K. S. Kannan and A. Dasgupta. A nonlinear galerkin finite-element theory for modeling magnetostrictive smart structures. *Smart Materials & Structures*, 6:341–350, 1997.

[70] J. L. Perez-Aparicio and H. Sosa. A continuum three-dimensional, fully coupled, dynamic, non-linear finite element formulation for magnetostrictive materials. *Smart Materials & Structures*, 13(3):493–502, 2004.

[71] J. G. Benatar and A.B. Flatau. Fem implementation of a magnetostrictive transducer. In *Proceedings of the Smart Structures and Materials Conference*, volume 5764, San Diego, USA. Proc. of SPIE.

[72] A. Demma. *The interaction of guided waves with discontinuities in structures*. PhD thesis, Imperial College London, 2003.

[73] M.V.K. Chari and P. Reece. Magnetic field distribution in solid metallic structures in the vicinity of current carrying conductors, and associated eddy-current losses. *Power Apparatus and Systems, IEEE Transactions on*, PAS-93(1):45–56, 1974.

[74] Magnet Sales & Manufacturing Inc. High performance permanent magnets 7.

[75] T. Yamasaki, Y. Shirayama, and M. Hirao. Magnetostriction of nickel under applied stress. *Transactions of the Japan Society of Mechanical Engineers Part A*, 19(3):434–439, 2007.

[76] Y. Chen, B. K. Kriegermeier-Sutton, J. E. Snyder, K. W. Dennis, R. W. McCallum, and D. C. Jiles. Magnetomechanical effects under torsional strain in iron, cobalt and nickel. *Journal of Magnetism and Magnetic Materials*, 236(1–2):131–138, 2001.

[77] J. C. Moulder, C. C. Tai, B. F. Larson, and J. H. Rose. Inductance of a coil on a thick ferromagnetic metal plate. *IEEE Transactions on Magnetics*, 34(2):505–514, 1998.

[78] E. Peterson and L. R. Wrathall. Eddy currents in composite laminations. *Proceedings of the Institute of Radio Engineers*, 24:275–286, 1936.

[79] J. H. Rose, E. Uzal, and J. C. Moulder. Magnetic permeability and eddy-current measurements. In D. Chimenti and D. Thompson, editors, *Review of*

Progress in Quantitative Nondestructive Evaluation, volume 14, pages 315–322, New York, 1995. Plenum.

[80] S. Momeni, A. Konrad, and A. N. Sinclair. Determination of reversible permeability in the presence of a strong bias field. *Journal of applied physics*, 105:103908, 2009.

[81] N. Bowler. Frequency-dependence of relative permeability in steel. In D. Chimenti and D. Thompson, editors, *Review of Progress in Quantitative Nondestructive Evaluation*, volume 25, pages 1269–1276, Brunswick, Maine, USA, 2006. AIP.

[82] A. Demma, P. Cawley, and M. Lowe. The reflection of the fundamental torsional mode from cracks and notches in pipes. *The Journal of the Acoustical Society of America*, 114:611–625, 2003.

[83] A. Velichko and P. D. Wilcox. Excitation and scattering of guided waves: Relationships between solutions for plates and pipes. *The Journal of the Acoustical Society of America*, 125(6):3623–3631, 2009.

[84] L. Satyarnarayan, J. Chandrasekaran, B. W. Maxfield, and K. Balasubramaniam. Circumferential higher order guided wave modes for the detection and sizing of cracks and pinholes in pipe support regions. *NDT & E international*, 41(1):32, 2008.

[85] S. Vinogradov and G. Kidd. Advanced guided wave piping and tubing inspection using magnetostrictive sensor technology. In *International EPRI Conference on NDE*, San Diego, 2006.

[86] Y. Y. Kim, C. I. Park, S. H. Cho, and S. W. Han. Torsional wave experiments with a new magnetostrictive transducer configuration. *The Journal of the Acoustical Society of America*, 117:3459–3468, 2005.

[87] M. Lowe, D. N. Alleyne, and P. Cawley. Defect detection in pipes using guided waves. *Ultrasonics*, 36(1-5):147–154, 1998.

[88] C. A. Harper. *Handbook of Plastics, Elastomers & Composites (4th Edition)*. McGraw-Hill Companies, New York, 2002.

[89] Z. Fan. *applications of guided wave propagation on waveguides with irregular cross-section*. PhD thesis, Imperial College London, 2010.

[90] F. Bloch, O. Cugat, G. Meunier, and J.C. Toussaint. Innovating approaches to the generation of intense magnetic fields: design and optimization of a 4 tesla permanent magnet flux source. *IEEE transactions on magnetics*, 34(5):2465–2468, 1998.

[91] H. G. Dorsey. Magnetostriction in iron-carbon alloys. *Physical Review*, 30(6):698–719, 1910.

[92] T. V. Venkatasubramanian and B. A. Unvala. An ac potential drop system for monitoring crack length. *Journal of Physics E: Scientific Instruments*, 17(9):765–771, 1984.

[93] G. Sposito, P. Cawley, and P. B. Nagy. An approximate model for three-dimensional alternating current potential drop analyses using a commercial finite element code. *NDT & E International*, 43(2):134–140, 2010.

[94] J. R. Bowler and N. Bowler. Theory of four-point alternating current potential drop measurements on conductive plates. *Proceedings of the Royal Society A: Mathematical, Physical and Engineering Sciences*, 463(2079):817–836, 2007.

[95] W. Yin, A. J. Peyton, M. Strangwood, and C. L. Davis. Exploring the relationship between ferrite fraction and morphology and the electromagnetic properties of steel. *Journal of Materials Science*, 42(16):6854–6861, 2007.

List of Publications

[P1] R. Ribichini, F. Cegla, P. B. Nagy, P. Cawley, "Modelling of Electromagnetic Acoustic Transducers Operating on Ferromagnetic Materials", in *Review of Progress in Quantitative Nondestructive Evaluation*, Kingston, Rhode Island. Edited by D. Chimenti, B. Thompson. 2010.

[P2] R. Ribichini, F. Cegla, P.B. Nagy, P. Cawley, "Quantitative Modelling of the Transduction of Electromagnetic Acoustic Transducers Operating on Ferromagnetic Media", *IEEE Trans. Ultrasonics, Ferroelectrics, and Frequency Control*, Volume 57, Issue 12, pp.2808–2817, 2010.

[P3] R. Ribichini, F. Cegla, P. B. Nagy, P. Cawley, "Evaluation of Electromagnetic Acoustic Transducer Performance on Steel Materials", in *Review of Progress in Quantitative Nondestructive Evaluation*, San Diego, California, 2011. In press.

[P4] R. Ribichini, F. Cegla, P. B. Nagy, P. Cawley, "Experimental and Numerical Evaluation of Electromagnetic Acoustic Transducer Performance on Steel Materials", *NDT&E International*, accepted, 2011.

[P5] R. Ribichini, F. Cegla, P. B. Nagy, P. Cawley, "Study and Comparison of Different EMAT Configurations for SH Wave Inspection" *IEEE Trans. Ultrasonics, Ferroelectrics, and Frequency Control*, accepted, 2011.